UNIVERSIDAD NACIONAL AUTÓNOMA DE MÉXICO
POSGRADO EN CIENCIAS DE LA TIERRA
INSTITUTO DE GEOFÍSICA
CIENCIAS ATMOSFÉRICAS, ESPACIALES Y PLANETARIAS

CHOQUES HELIOSFÉRICOS: SIMULACIONES Y OBSERVACIONES

TESIS
QUE PARA OPTAR POR EL GRADO DE
DOCTOR EN CIENCIAS

PRESENTA:
LUIS FEDERICO PREISSER RENTERÍA

TUTOR PRINCIPAL
DRA. XÓCHITL G. BLANCO CANO
INSTITUTO DE GEOFÍSICA

COMITÉ TUTOR
DR. ERNESTO AGUILAR RODRÍGUEZ
INSTITUTO DE GEOFÍSICA (MICHOACÁN)

DR. ALFREDO J. SANTILLÁN GONZÁLEZ
DGTIC / UNAM

CD.MX., NOVIEMBRE 2020

A Luca y Cayetana

Agradecimientos

A mi madre, por su amor y apoyo incondicional siempre y en cada una de las decisiones que he tomado a lo largo de toda mi vida. Pero más allá de todo, por el ejemplo de amor, lucha y trabajo para alcanzar lo que se ha propuesto y sacarnos a todos adelante, sin importar las numerosas adversidades a las que se ha enfrentado y que habrían hecho flaquear a cualquier otro. Eres la persona a la que más admiro en el mundo mamá.

A mi padre, por la preocupación que siempre puso en nuestra educación tanto académica como moral. Por las miles de discusiones que tuvimos sobre las otras miles de cosas sobre las que no estabamos de acuerdo y las pocas sobre las que sí. Al final me sirvieron para aprender a defender con argumentos mis puntos de vista.

A mis hermanos, Ernesto, Omar, Dante y Darío, por que sé que siempre van a estar ahí cuando los necesite. Hay pocas cosas más poderosas que el estar seguro de poder contar con alguién sin importar las circunstancias y saber que uno también es capaz de estar ahí para el otro ante cualquier problema. Mi amor, admiración y orgullo total hacia todos ustedes, siempre.

A Luca y Cayetana, el motor que hace que no desista de hacer lo que hago y me mantiene en pie siempre. Simplemente no hay palabras que puedan describir lo agradecido que estoy por tenerlos en mi vida, son lo que más amo y punto pelota !

A Xóchitl, por TODO EL APOYO (con mayúsculas) y los regaños (con minúsculas), estos últimos sobre todo al principio del doctorado pues ubicaron al físico "rebelde" y me hicieron amar las Ciencias Espaciales. Por las risas, las pláticas, las discusiones científicas, los congresos, las presentaciones con gente, los buenos consejos y un larguísimo etcétera. Por ser la mejor asesor(a) con la que me pude haber topado, sin lugar a dudas. Has sido una gran influencia en mi vida académica y personal.

A Primoz, por la camaradería y las interminables discusiones y encontronazos sobre los papers en los que colaboramos. Los antagonismos que tuvimos (y que seguramente seguiremos teniendo) al final son de lo que más se aprende, y eso es invaluable.

A Ernesto, por estar siempre ahí para lo que se pudiera ofrecer, por el asilo en San Francisco (y las chelas también, obviamente), por todos los buenos consejos y los comentarios de ánimo al acabar cada semestre.

A Alfredo Santillán, por sus comentarios siempre oportunos con respecto a mi trabajo y lo constructivo de sus críticas a la hora de las evaluaciones semestrales.

A Alejandro Lara, por ese humor ácido al que uno debe acostumbrarse pero que vale la pena ya que después uno sabe que puede recurrir a él con cualquier duda o propuesta académica por incoherente que sea, por siempre tener tiempo para escuchar y las invitaciones a los proyectos. Y obvio, por las reuniones de fin de año!

A Rogelio Caballero, por la camaradería, las discusiones mañaneras sobre física y política, por esa excelente clase de rayos cósmicos y por siempre tener la puerta abierta para (plumón en mano) buscar en el pizarrón la respuesta.

A Julio Herrera, por ser el excelente maestro y ser humano que es. Por las excelentes clases "gratis" de plasmas, por las discusiones, los prestamos de libros, las invitaciones a congresos, seminarios y confererencias, por ser una persona comprometida con la educación y los estudiantes y SIEMPRE tener la puerta abierta para platicar y discutir sobre ciencia. Pocas personas que dominen y estén dispuestos a explicar como usted el tema Dr. Herrera.

A Alex Raga, por siempre mostrar una sincera preocupación (desde que fué parte de mi comité en la maestría) y expresar su apoyo a mi trabajo. Por esos comentarios tan buenos sobre el presente trabajo y por siempre tratar a los alumnos como iguales.

A Dolores Maravilla, por siempre mostrar esa preocupación sincera sobre lo que estaba haciendo o iba a hacer, por los igualmente sinceros consejos y frases de ánimo cada vez que nos encontrabamos en los pasillos y por siempre fomentar mi continua preparación.

A Diana Rojas, por que aún del otro lado del mundo, nunca dejó de ayudarme y apoyarme en lo que se podía. Por las discusiones sobre el "debiera" de tantas cosas que hay que cambiar y por siempre estar ahí para (muy a nuestro estilo) apoyarnos. Aún siendo yo un "fresa" indigno de su amistad proletaria y de lucha jajajajajaja.

A Hector Pérez de Tejada y Hector Durán, por contagiarme ese amor a la ciencia y esa curiosidad que tienen por lo que hacen. Por no quedarse callados cuando rechazan alguna de sus ideas y siempre estar dispuestos a discutir sobre física.

A Alberto Flandes, por sus consejos e interés en mi vida académica, incluso sin tener mucho que ver con mi trabajo académico.

A Adriana Morales, por todo el apoyo secretarial recibido y su amabilidad, pero sobre todo por siempre recibirnos a todos con una sonrisa al entrar al departamento y las incontables charlas y risas mañaneras.

To David Burgess, for his patience and his good reception in London, his camaraderie and openness to answer any question about HYPSI, the good lunches and beers at the QMUL pub and the good times in his visit to Mexico.

To Domenico Trotta, for the good times both in London and CDMX, for the endless discussions about the HYPSI code, data visualization and plasma physics. For every night in the pubs where so many ideas came from and still stand for the future. But above all else, for your sincere friendship. Grazie mille per tutto!

A todos los compañeros y amigos "del pasillo" por las horas frente al pizarrón, los clubes de lectura, las "chelas & pizza" de los viernes, las pláticas a la hora de la comida, los cafés y/o tés, las discusiones sobre política, software, hardware, programación, música, literatura, videojuegos, etc. Sin ustedes mi tiempo en Geofísica no hubiera sido lo genial que fué. Alberto, Arturo, Pablo, Tatiana, Ángel, Arum, Alma, Karla, Amanda, Gaby, Paulina, Pedro, Oscar, Dulce, Alicia y Mariana mil gracias por su amistad y cariño.

A todo el equipazo de supercómputo de la DGTIC gracias infinitas por toda la ayuda recibida y el acceso a la supercomputadora MIZTLI de la UNAM. Gracias por haber hecho que me reencontrara con Linux y todas las clases "gratis" que gustosos me dieron.

Al Instituto de Geofísica de la UNAM por brindarme todas las facilidades a nivel humano y de infraestructura para poder realizar mis estudios en un ambiente propicio para ello. Sin duda, una institución de admirar.

Finalmente, a los proyectos institucionales CONACyT 174700, CONACyT 255203, DGAPA/PAPIIT IN105218, DGAPA/PAPIIT IN205014, Royal Society Newton International Exchange Scheme (Mexico) grant NI150051 y LANCAD-UNAM-DGTIC-337.

Índice general

Introducción

El estudio de las ondas de choque (o simplemente choques) en un plasma sin colisiones ha sido fuertemente motivado por las observaciones realizadas en la heliosfera. Si bien la más simple descripción teórica de un choque es la de una discontinuidad que separa dos estados en un flujo, el reciente avance en la instrumentación espacial ha propiciado el estudio *in situ* de la estructura a pequeña escala "dentro" de esta discontinuidad. Aunque esto pudiera limitar nuestro conocimiento solamente al rango de parámetros de los choques heliosféricos, las observaciones y modelos desarrollados a partir de éstas pueden ser aplicados a entornos astrofísicos más distantes para los cuales es imposible contar con la calidad de datos obtenidos en la heliosfera.

La heliosfera es la región dominada por el flujo del viento solar y su campo magnético. La naturaleza supersónica de este flujo de plasma sin colisiones (el camino libre medio de sus partículas es del orden de 1 unidad astronómica o AU por sus siglas en inglés) es lo que da lugar, de forma natural, a los choques interplanetarios. Hay varias formas de clasificar estos choques dependiendo de cómo han sido formados o si son un fenómeno transitorio o permanente dentro de este flujo de viento solar. Un obstáculo a dicho flujo, como por ejemplo una magnetosfera planetaria, puede generar un choque de proa (Figura 1) alrededor del planeta. Por otra parte, cambios en la velocidad del flujo en la fuente del viento solar pueden dar lugar a compresiones capaces de producir choques. Estos, a su vez, pueden evolucionar como un patrón de flujo (Figuras 2 y 3) a través del medio interplanetario.

En el caso del choque de proa terrestre, a medida que el viento solar pasa a través de éste, se calienta y se frena al mismo tiempo que es desviado alrededor de la magnetopausa, que es la frontera entre los campos magnéticos planetario y solar. La región de flujo subsónico localizada entre el choque de proa y la magnetopausa es conocida como

la magnetofunda terrestre. El proceso de reconexión magnética que puede tener lugar en la magnetopausa, es capaz de permitir el intercambio de material entre la magnetofunda (viento solar que ha pasado de supersónico a subsónico a través del choque de proa) y la magnetosfera terrestre.

Una de las consecuencias más interesantes de la forma curva del choque de proa terrestre (ver Figura 1) es el hecho de que la geometría magnética de éste, caracterizada por el parámetro θ_{Bn} definido como el ángulo entre el campo magnético en la región río arriba $\mathbf{B_{sw}}$ y el vector normal a la superficie del choque $\mathbf{n}$, puede variar a lo largo de su superficie. Dependiendo del valor de este parámetro, los choques pueden ser clasificados como cuasiparalelos (θ_{Bn} <45°) o cuasiperpendiculares (θ_{Bn} >45°). Otro parámetro que es usado, esta vez para caracterizar la geometría local del flujo del viento solar, es el ángulo θ_{Vn} entre el vector de velocidad del viento solar $\mathbf{V_{sw}}$ y el vector $\mathbf{n}$.

La forma curva del choque de proa además da lugar a una región turbulenta, río arriba de la región cuasiparalela, conocida como el antechoque terrestre. Esta región turbulenta es generada por la interacción entre las partículas que son reflejadas eficientemente bajo esta geometría y el flujo de viento solar que continuamente permea en sentido contrario la región río arriba. Para una configuración promedio del viento solar, en la región río arriba (i.e. un ángulo entre el campo magnético del viento solar y la línea Sol-Tierra de ∼45°), existe una clara distinción entre la región cuasiperpendicular, donde no existe antechoque terrestre, y la región cuasiparalela, donde la interacción choque-antechoque es importante en la estructura de este último. Esta distinción y sus subsecuentes características también pueden ser extrapoladas a la región río abajo del choque de proa como se ilustra en la Figura 1.

Otro aspecto a considerar es que mientras el perfil del choque cuasi-perpendicular está bien definido debido a que el campo magnético tangencial a su superficie no permite que las partículas sean reflejadas lejos de éste, la transición del choque cuasiparalelo, por el contrario, no se encuentra bien definida y la región río abajo de éste, que es el antechoque anteriormente mencionado, se encuentra permeada por partículas reflejadas que se mueven a lo largo de las líneas de campo magnético en dicha región.

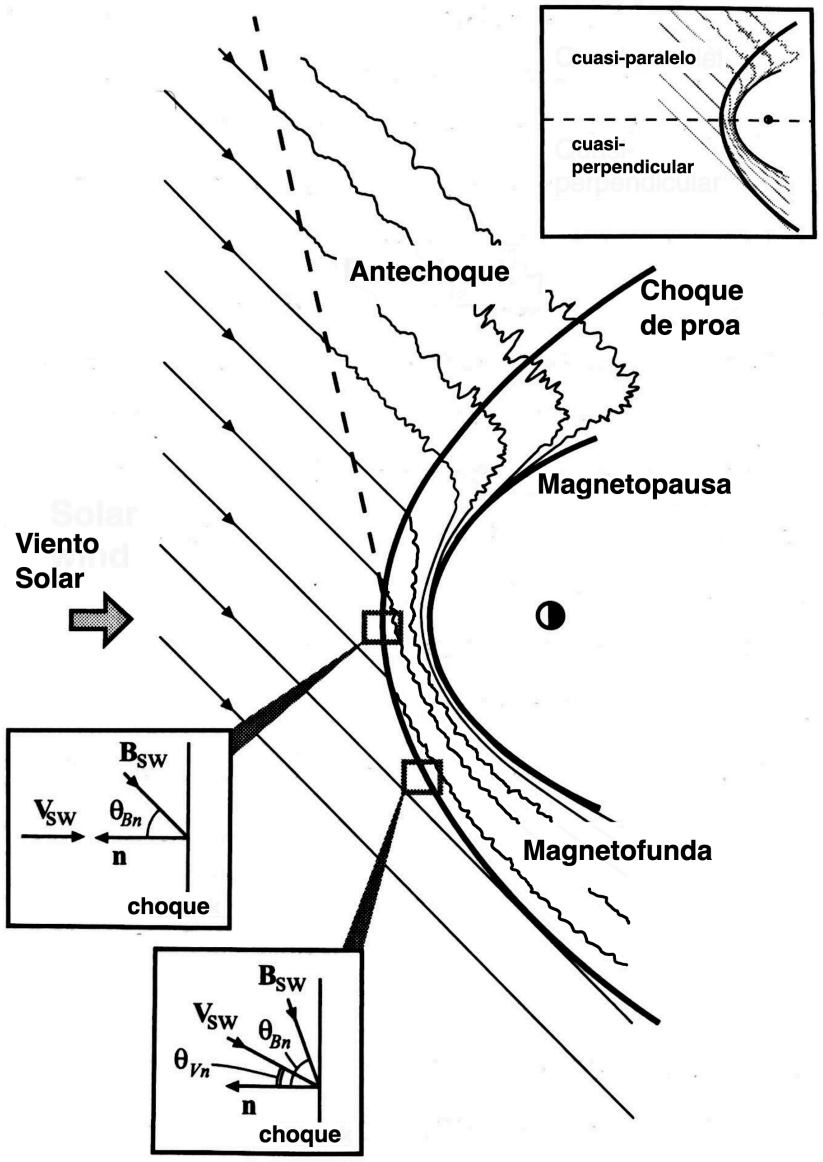

Figura 1: Esquema del choque de proa terrestre sobre el plano de la eclíptica donde se ilustran varias regiones y parámetros relacionados con éste. El esquema corresponde a un campo magnético interplanetario que forma un ángulo de 45° con respecto a la línea Sol-Tierra. Adaptado de Burgess and Scholer (2015)

A medida que estas partículas interaccionan con el flujo de viento solar, diferentes tipos de ondas y estructuras de gran amplitud son generadas. Estas ondas interaccionan con el choque conforme son transportadas hacia éste por el flujo del viento solar. Dicho proceso es el responsable de que la región de la magnetofunda tenga también un comportamiento turbulento. Es en esta región turbulenta, río abajo del choque cuasiparalelo, donde las es-

tructuras transitorias conocidas como jets y plasmoides han sido mayormente observadas y caracterizadas (Plaschke et al., 2018).

Como se mencionó anteriormente, los choques también pueden ser formados a partir de cambios locales del flujo de viento solar al ser generado en el Sol. Los choques generados de este modo se propagarán dentro del mismo viento solar por lo que se les conoce como choques interplanetarios. El Sol produce viento solar con velocidades que dependen de la localización de la fuente de éste en la corona. Dependiendo de su velocidad, el viento solar puede ser clasificado como rápido ($\mathbf{V_{sw}} \sim$ [600-800] km/s) o lento ($\mathbf{V_{sw}} \sim$ [300-500] km/s). Si para alguna heliolongitud dada uno de estos flujos rápidos alcanza a uno lento, la rotación solar y la expansión casi radial del viento solar permitirá, debido a la diferencia de velocidades de estos dos flujos, la formación de una región de compresión por delante y detrás de esta interface. Dependiendo de la evolución de esta región de compresión, se podrán o no generar choques por delante y detrás de ésta. Este patrón de interacción entre los dos flujos rota con el Sol por lo que es llamado región de interacción corrotante (CIR por sus siglas en inglés) y es ilustrado en la Figura 2. Observacionalmente, desde el punto de vista de una sonda, la CIR viaja radialmente por lo que primero se observará el choque frontal seguido de la interfaz y finalmente el choque reverso. Típicamente, estas estructuras se forman en regiones a 1-2 AU del Sol y su extensión espacial dependerá de la forma y tamaño de las regiones que generan los flujos rápidos en la corona solar, cuyas características a su vez dependerán de diferentes factores; por ejemplo, el ciclo solar (Jian et al., 2006a).

Los choques interplanetarios también pueden ser formados cuando un cambio abrupto en la velocidad y densidad del viento solar se presenta en la corona. Las eyecciones de masa coronal (CMEs por sus siglas en inglés) son la principal fuente de este tipo de choques "impulsivos" en la heliosfera (Jian et al., 2006b; Zurbuchen and Richardson, 2006). Si la velocidad de la CME es supersónica con respecto al viento solar ambiente, entonces a medida que la CME se expande, al propagarse a través de la heliosfera será precedida por un choque interplanetario generado por ésta. La forma de la CME es más curva y su tamaño generalmente llega a ser mayor que el de una CIR. Un aspecto que es importante señalar aquí es que los parámetros usados para caracterizar la geometría local del choque

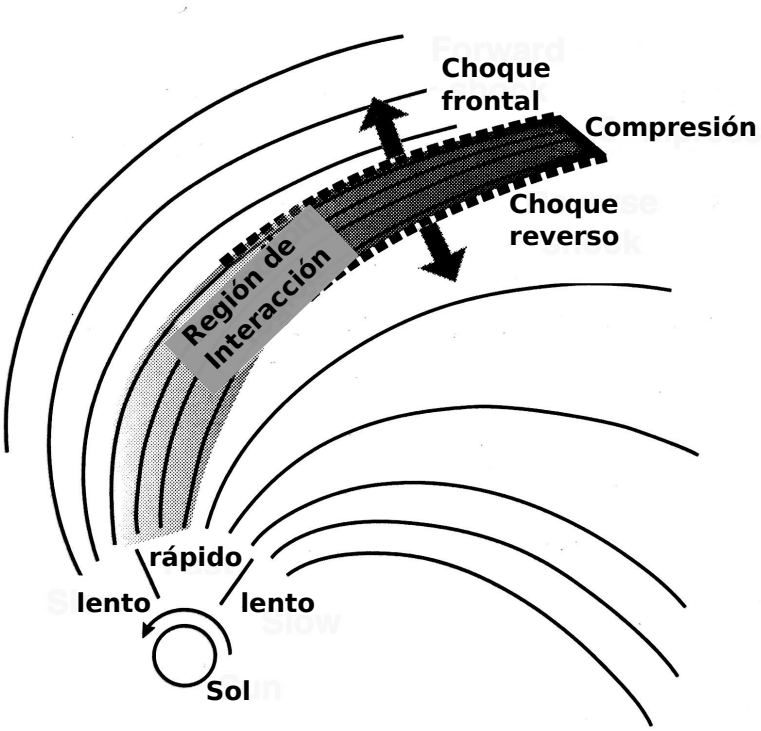

Figura 2: Esquema de la formación de una región de interacción corrotante y sus choques asociados, a partir de la interacción de los flujos lentos y rápidos generados en el Sol. Las flechas representan el movimiento de los choques con respecto al flujo de viento solar ambiente. Adaptado de Burgess and Scholer (2015)

de proa (e.g. θ_{Bn}, θ_{Vn}) son igualmente aplicables a los choques interplanetarios generados por las CMEs y CIRs.

Conforme la CME se propaga a través de la heliosfera, la forma y fuerza del choque asociado a ésta puede variar. Cabe mencionar que, además del choque asociado a la CME, ésta puede o no presentar algunas regiones asociadas (Figura 3), el choque que ya hemos mencionado, una región de plasma turbulento llamada magnetofunda y un obstáculo conocido como nube magnética caracterizado por una topología magnética con forma de bucle. Debido a que una sonda solo puede atravesar una CME a lo largo de una trayectoria 1D, no siempre podrá detectar todos los componentes de su estructura interna.

Aunque las condiciones de la interfaz del choque, sin importar su mecanismo de generación, están básicamente determinadas por la dinámica de los protones como especie iónica más abundantes en el viento solar, existen otras especies menores; por ejemplo, las partículas alfa (He^{++}) que son la más importante constituyendo entre el 4 y 5 % de

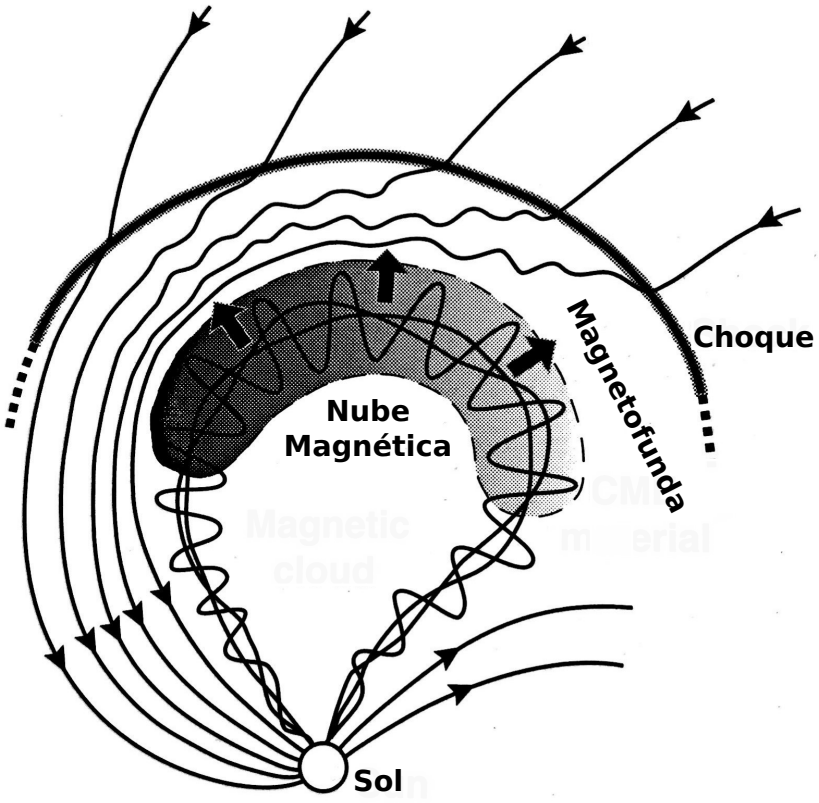

Figura 3: Esquema de un choque interplanetario producido por una eyección de masa coronal. Las líneas con flechas superimpuestas representan el campo magnético y su polaridad. Las flechas representan el movimiento de la nube magnética con respecto al Sol. Adaptado de Burgess and Scholer (2015)

la densidad numérica de iones (Ipavich et al., 1984). Aunque este porcentaje puede ser considerado bajo, su contribución a la densidad y presión dinámica, río arriba de los choques interplanetarios, puede constituir hasta del 20 % (Gedalin, 2017). Desde el punto de vista cinético, su sola presencia como segunda especie puede dar lugar a diferentes tipos de inestabilidades.

En esta tesis, formada por cuatro artículos ya publicados, hemos estudiado de manera observacional y teóricamente, a través de simulaciones numéricas, diferentes aspectos y características asociados con la microfísica de choques interplanetarios sin colisiones: La estructura rugosa del choque, la influencia de las partículas alfa y la geometría en diferentes procesos que se llevan a cabo en éstos, así como el estudio de estructuras encontradas

recientemente en la región río abajo del choque terrestre, a saber jets y plasmoides. Dichos estudios son relevantes en el contexto del reciente lanzamiento de diferentes misiones (MMS, CLUSTER, Parker Solar Probe, Solar Orbiter) con instrumentos cuya resolución, sin precedentes, nos permitirá entender mejor la microfísica de los fenómenos estudiados en esta tesis y el futuro contraste de nuestros resultados con las observaciones.

Debido a que se optó por la modalidad de titulación por artículos publicados, a continuación y siguiendo los lineamientos del Posgrado en Ciencias de la Tierra, se presenta un breve resumen de cada uno de éstos, seguido por la versión original correspondiente. Se finaliza la tesis con una conclusión general del conjunto de publicaciones que la conforman.

Capítulo 1

Observaciones de irregularidades, a escalas iónicas, en la superficie de choques interplanetarios usando Cluster.

1.1. Resumen del trabajo y metodología

En este trabajo presentamos, por primera vez, evidencia observacional directa de la estructura rugosa en los frentes de choques interplanetarios a escala iónica. Los datos fueron obtenidos a partir de observaciones multi nave usando los datos de las cuatro naves que forman la misión Cluster (Escoubet et al., 1997). El estudio comprende el análisis observacional de cuatro choques interplanetarios con números de Mach Alfvénicos (M_A) $3.5 \leq M_A \leq 4.4$. De los choques observados, tres poseen un valor alto de $\beta = 2.2,\ 2.4,\ 3.7$ (donde β es el cociente entre la presión térmica y magnética del plasma) mientras que el cuarto posee un valor inferior a uno ($\beta = 0.22$). El ángulo θ_{Bn} entre el vector normal $\mathbf{n}$ al choque y el campo magnético ($\mathbf{B_{sw}}$) río arriba, para los choques observados, cubre un rango de $13° \leq \theta_{Bn} \leq 74°$. Para el cálculo de la normal al choque, en cada nave y entre pares de éstas, se diseñó un nuevo método para estimar el error en la medición de θ_{Bn},

resultando ser $\sim 5°$. La distancia entre las naves que realizaron las observaciones varía desde $<$ 1 hasta 100 longitudes inerciales iónicas ($d_i = c/\omega_i$ con c la velocidad de la luz y ω_i la frecuencia iónica del plasma). El análisis de las observaciones muestra que tanto los perfiles de campo magnético como los vectores localmente normales a los choques son muy similares cuando las naves se encuentran separadas por distancias cercanas a 1 d_i. En cambio, dichos parámetros resultan ser bastante diferentes cuando la distancia entre las naves es mayor ($\geq 10d_i$). Estos resultados sugieren que las diferencias entre las mediciones se deben a que las naves atraviesan zonas a lo largo del frente del choque que presentan arrugamientos (Winske and Quest, 1988; Ofman and Gedalin, 2013; Krauss-Varban et al., 2008) o irregularidades debidas tanto a la no estacionalidad (Lowe and Burgess, 2003) como a los procesos de reformación en choques estudiados (Biskamp and Welter, 1972; Leroy et al., 1982).

Para corroborar esta interpretación se compararon los perfiles de los choque observados con simulaciones híbridas realizadas con el código HYPSI (Burgess and Scholer, 2015; Gingell et al., 2017) en las que los parámetros de entrada eran similares a los obtenidos en las observaciones i.e. M_A, θ_{Bn} y β para después reproducir los perfiles en campo magnético con separaciones equivalentes a las distancias inter-nave de Cluster. Los resultados de las simulaciones concuerdan con el análisis observacional. De las simulaciones además se infiere que la causa de las irregularidades observadas en los choques pueden ser las estructuras magnéticas (ondas) en la región río arriba que son transportadas por el flujo hacia el choque. Para confirmar esta hipótesis se realizó el análisis wavelet del campo magnético en la regiones río arriba de los choques observados por Cluster 1 identificando la presencia de ondas. Los resultados muestran que en todos los choques existen fluctuaciones en el rango de las ondas de frecuencia ultrabajas (0.01-0.1 Hz) (Burgess, 1989; Krauss-Varban and Omidi, 1991; Schwartz and Burgess, 1991) probablemente generadas en la región del antechoque terrestre en la que Cluster 1 entró $\sim$20 minutos antes de observar el choque y que son identificados por incrementos en el flujo de iones supratérmicos en los espectrogramas correspondientes a estas regiones. En dichas fluctuaciones la potencia de la componente transversal resultó ser mayor que la compresiva.

1.2. Publicación en Astrophysical Journal Letters (ApJL) (2019)

The Astrophysical Journal Letters, 874:L13 (11pp), 2019 April 1 https://doi.org/10.3847/2041-8213/ab0e84

First Observations of Irregular Surface of Interplanetary Shocks at Ion Scales by *Cluster*

Primož Kajdič[1], Luis Preisser[1], Xóchitl Blanco-Cano[1], David Burgess[2], and Domenico Trotta[2]
[1] Instituto de Geofísica, Universidad Nacional Autónoma de México, Circuito de la investigación Científica s/n, Ciudad Universitaria, Delegación Coyoacán, C.P. 04510, Mexico City, Mexico; primoz@igeofisica.unam.mx
[2] School of Physics and Astronomy, Queen Mary University of London, London E1 4NS, UK
Received 2018 October 24; revised 2019 February 17; accepted 2019 February 26; published 2019 March 27

Abstract

We present the first observational evidence of the irregular surface of interplanetary (IP) shocks by using multispacecraft observations of the *Cluster* mission. In total we discuss observations of four IP shocks that exhibit moderate Alfvénic Mach numbers ($M_A \leqslant 6.5$). Three of them are high-β shocks with upstream $\beta = 2.2$–3.7. During the times when these shocks were observed, the *Cluster* spacecraft formed constellations with inter-spacecraft separations ranging from less than one upstream ion inertial length (d_i) up to $100\,d_i$. Expressed in kilometers, the distances ranged between 38 km and $\sim 10^4$ km. We show that magnetic field profiles and the local shock normals of observed shocks are very similar when the spacecraft are of the order of one d_i apart, but are strikingly different when the distances increase to 10 or more d_i. We interpret these differences to be due to the irregular surface of IP shocks and discuss possible causes for such irregularity. We strengthen our interpretation by comparing observed shock profiles with profiles of simulated shocks. The latter had similar characteristics (M_A, θ_{BN}, upstream ion β) as observed shocks and the profiles were obtained at separations across the simulation domain equivalent to the *Cluster* inter-spacecraft distances.

Key words: acceleration of particles – interplanetary medium – shock waves

Supporting material: animations

1. Introduction

Interplanetary (IP) shocks are ubiquitous in the heliosphere and are mostly associated with interplanetary coronal mass ejections (e.g., Sheeley et al. 1985) and stream interaction regions (e.g., Gosling & Pizzo 1999). Since the solar wind (SW) is a collisionless plasma, the heliospheric shocks are also collisionless. Marshall (1955) realized that purely resistive dissipation mechanisms cannot sustain collisionless shocks when their Mach number exceeds some critical value M_c. Sagdeev (1966) suggested that particle acceleration and reflection at the shock surface could be an efficient mechanism to dissipate the kinetic energy of the incoming SW.

Numerical simulations show that one of the characteristics of supercritical collisionless shocks is the nonstationarity or reformation of their surface which leads to its irregularity. Depending on the shock properties (Alfvénic Mach number M_A, the angle θ_{BN} between the upstream B-field and the shock normal, and the ratio β of the upstream thermal to magnetic pressure), the nonstationarity may be due to the self-reformation of the shock surface (e.g., Biskamp & Welter 1972; Leroy et al. 1982), the whistler mode waves emitted in the foot/ramp (Hellinger et al. 2007; Scholer & Burgess 2007; Lembge et al. 2009) or the upstream ultra-low frequency (ULF) waves and steepened foreshock structures (e.g., Burgess 1989; Krauss-Varban & Omidi 1991; Schwartz & Burgess 1991; Krauss-Varban et al. 2008).

Self-reformation is favored by large M_A and small upstream β and produces shock rippling at small spatial scales along the shock surface ($\lesssim$1 ion inertial length, d_i). Large amplitude whistler waves emitted in the foot cause rippling at spatial scales of a few d_i. Finally, irregularities due to upstream ULF waves occur at spatial scales of several tens of d_i.

Shock surface rippling was first studied by comparing with 2D hybrid (kinetic ions, massless fluid electrons) simulations by Winske & Quest (1988) and later by, for example, Lowe & Burgess (2003) and Ofman & Gedalin (2013). The latter showed that the difference between the global shock normal (determined by the far upstream and far downstream states) and the local normal (determined by the local direction of the fastest variation of the magnetic field) due to rippling can be as large as 40°. Burgess (2006a, 2006b) studied simulated high Mach number ($M_A = 9.7$), almost perpendicular ($\theta_{BN} \lesssim 90°$) shocks and showed that the B-field profiles observed by virtual probes varied even when the probes were closely separated ($\leqslant 2.5\,d_i$) and that the shock surface ripples cause large variations of the local θ_{BN}.

Larger-scale irregularity of shock surface was reproduced by Krauss-Varban et al. (2008) who performed local hybrid simulations of a shock with $M_A = 4.7$ and $\theta_{BN} = 50°$. They observed that in the case of large-scale shocks, such as IP shocks, even a very small amount of reflected ions generate upstream compressional waves that bend the B-field lines and change the local θ_{BN}. The portions of the shock that become more parallel eject more protons back upstream and further enhance the compressional waves there. These regions were found to travel along the shock surface leading to irregularities with a wavelength of $100\,d_i$ or more.

Shock ripples and their importance for particle acceleration and for formation of downstream phenomena have been the subject of several works (i.e., Gedalin 2001; Hietala et al. 2009; Yang et al. 2011, 2018; Hao et al. 2016). Rippling was observed at the Earth's bow-shock by several authors by using multi-spacecraft data from *Cluster* (Horbury et al. 2001, 2002; Moullard et al. 2006; Lobzin et al. 2008) and *Magnetospheric Multiscale* mission (Johlander et al. 2016; Gingell et al. 2017).

As for the IP shocks, several authors (i.e., Russell & Alexander 1984; Russell et al. 2000; Szabo et al. 2001, 2003; Szabo 2005; Pulupa & Bale 2008; Koval & Szabo 2010; Kajdič et al. 2017) discussed and/or observed their nonplanar structure at scales of several tens of Earth radii (R_E), but never at ion scales.

Although the particle acceleration mechanisms at Earth's bow-shock and at IP shocks should be the same, the IP shocks at 1 au have much larger curvature radii (~0.5 au) and the majority exhibit smaller magnetosonic Mach numbers (up to four, e.g., Blanco-Cano et al. 2016). This is reflected in the way the ions are accelerated at IP shocks. For example, Kajdič et al. (2017) reported first observations of field-aligned ions upstream of an IP shock with much higher energies than those observed at the Earth's bow-shock (e.g., Gosling et al. 1978).

Here we use the multi-spacecraft capabilities of the *Cluster* mission to study the structure of IP shock fronts. At the times of the shocks the four probes were separated between several tens to several thousands of kilometers, which corresponds to less than one to several tens of upstream ion inertial lengths (d_i). All the shocks exhibit moderate Alfvénic Mach numbers ($M_A \leqslant 6.5$). Three of the shocks also exhibit upstream ion β values (ratio between ion thermal and magnetic pressures) larger than unity. This is different from the studies of the rippling of the Earth's bow-shock surface where β was either larger than 1 but M_A were also very large (e.g., Moullard et al. 2006) or β was much smaller than 1 and M_A was moderate (e.g., Johlander et al. 2016; Yang et al. 2018).

We compare shock profiles, local shock normals, and geometries at each spacecraft and show that these vary even at small ($<10\,d_i$) spacecraft separations. We attribute these differences to irregular IP shock surface and further strengthen our case with 2D hybrid simulations.

2. Observations: Shock Profiles

In this section we compare *B*-field profiles of four shocks observed on 2001 January 17, 2010 April 5, 2012 February 26, and 2012 March 8. We use data obtained by the Flux Gate Magnetometers (FGM, Balogh et al. 1997, 2001) on board the four identical *Cluster* (Escoubet et al. 1997) probes.

Figure 1 shows *Cluster* FGM data with time resolution of 22 vectors per second at four different times during which the shocks were observed. Different colors correspond to different spacecraft with black, blue, green, and red lines representing the *Cluster* 1 (*C1*), *2* (*C2*), *3* (*C3*), and *4* (*C4*) data, respectively. The IP shocks were selected from the Catalog of IP shocks observed in the Earth's neighborhood by multiple spacecraft available at http://usuarios.geofisica.unam.mx/primoz/IPShocks.html. Basic shock parameters are exhibited on each panel: the range of angles θ_{BN}, the shock's Alfvénic (M_A), and magnetosonic (M_{ms}) Mach numbers (if all the data are available, otherwise only M_A is provided) and the upstream ion β. If the data were missing in the catalog, values were obtained from the *Comprehensive database of interplanetary shocks* at www.ipshocks.fi. During these times the *Cluster* probes formed different constellations. Separations of pairs of spacecraft are provided in Table 1.

2.1. 2001 January 17 Shock

On 2001 January 17 a fast forward shock (panel (a) in Figure 1) was detected at 16:27:48 UT by the *C1* and *C3* spacecraft. *C2* detected the shock about a second earlier, while *C4* observed the initial *B*-field increase at the same time as *C1* and *C3*, but the increase was much more gradual in its data. We see from Table 1 that in this case the spacecraft separations were between 530 km (7.4 d_i) and 1300 km (18.1 d_i).

C2 was the most sunward spacecraft, therefore detecting the shock first. It was followed by *C3* and *C4*, while *C1* was closest to the Earth. Although *C3* and *C4* had the most similar X_{GSE} coordinates it was *C1* and *C3* that detected the shock ramp simultaneously. The spacecraft positions and the local shock orientation in the Y_{GSE}–Z_{GSE} plane probably account for this.

We find that shock profiles observed by the four spacecraft are not the same (Figure 1(a)). *C2* (blue) observed a ramp, an overshoot, and possibly a foot. A small peak just upstream of the shock ramp could be a small whistler wave precursor. The *B*-field magnitude of the overshoot was 7.2 nT, which is more than in the other three cases. *C1* and *C3* (black and green) observed the shock ramp simultaneously but the *B*-field magnitudes were slightly different (7.0 nT and 6.5 nT, respectively). Just after the ramp, both spacecraft observed an overshoot, a short lasting undershoot, and another peak with similar *B*-field magnitude value as the first peak. Finally, the shock ramp observed by *C4* (red) is not as steep as in the other three cases. After the overshoot there is a strong dip (undershoot) after which the *B*-field magnitude rises again. Just before the shock ramp, *C1* (black) observes a small peak similar to that observed by *C2*. *C4* does not observe any foot; however, it detects a distinct compressive structure that lasts ~2 s peaking at 16:27:46 UT. Similar structures are observed by *C1* at 16:27:35.5 UT and 16:27:42.5 UT.

2.2. 2010 April 5 Shock

This shock was detected at 08:24:59 UT by *C1* (Figure 1(b)). *C2* detected it about two seconds earlier while *C3* and *C4* observed it simultaneously some 4 s later. The positions of the spacecraft were such that *C3* and *C4* were separated by only 200 km (1.5 d_i), so they observed almost identical shock profiles. These two probes observe a well defined ramp and overshoot followed by two dips and peaks. The latter could be old overshoots from previous reformation cycles or compressive waves. *C3* detected a short lasting (~1 s) whistler precursor with frequency of ~3 Hz that can barely be distinguished in *C4* data. *C2* (blue) observed a steep ramp and an overshoot followed by a very short lasting dip and another increase of *B*. Upstream of the ramp *C2* observed a short lasting whistler precursor. Further downstream there is a deep dip in the *C2* data, similar to that observed by *C3* and *C4*. *C1* (black) observed a much more gradual shock transition, typical of quasi-parallel ($\theta_{BN} \leqslant 45°$) shocks.

2.3. 2012 February 26 Shock

C1 observed this shock at 21:38:18 UT (Figure 1(c)) followed by *C3* and *C4* spacecraft that observed it simultaneously ~3 s later, while *C2* observed it ~5 s later. *C3* and *C4* were separated by only 38 km (0.37 d_i), while the other separations were much larger. It is interesting that while all θ_{BN} values (13°–39°) indicate that this is a quasi-parallel shock, all profiles resemble those of quasi-perpendicular ($\theta_{BN} > 45°$) shocks with steep ramps and overshoots. *C1* and *C2* observed a high frequency whistler precursor just upstream of the shock. These waves exhibit small amplitudes (0.1–0.2 nT) and

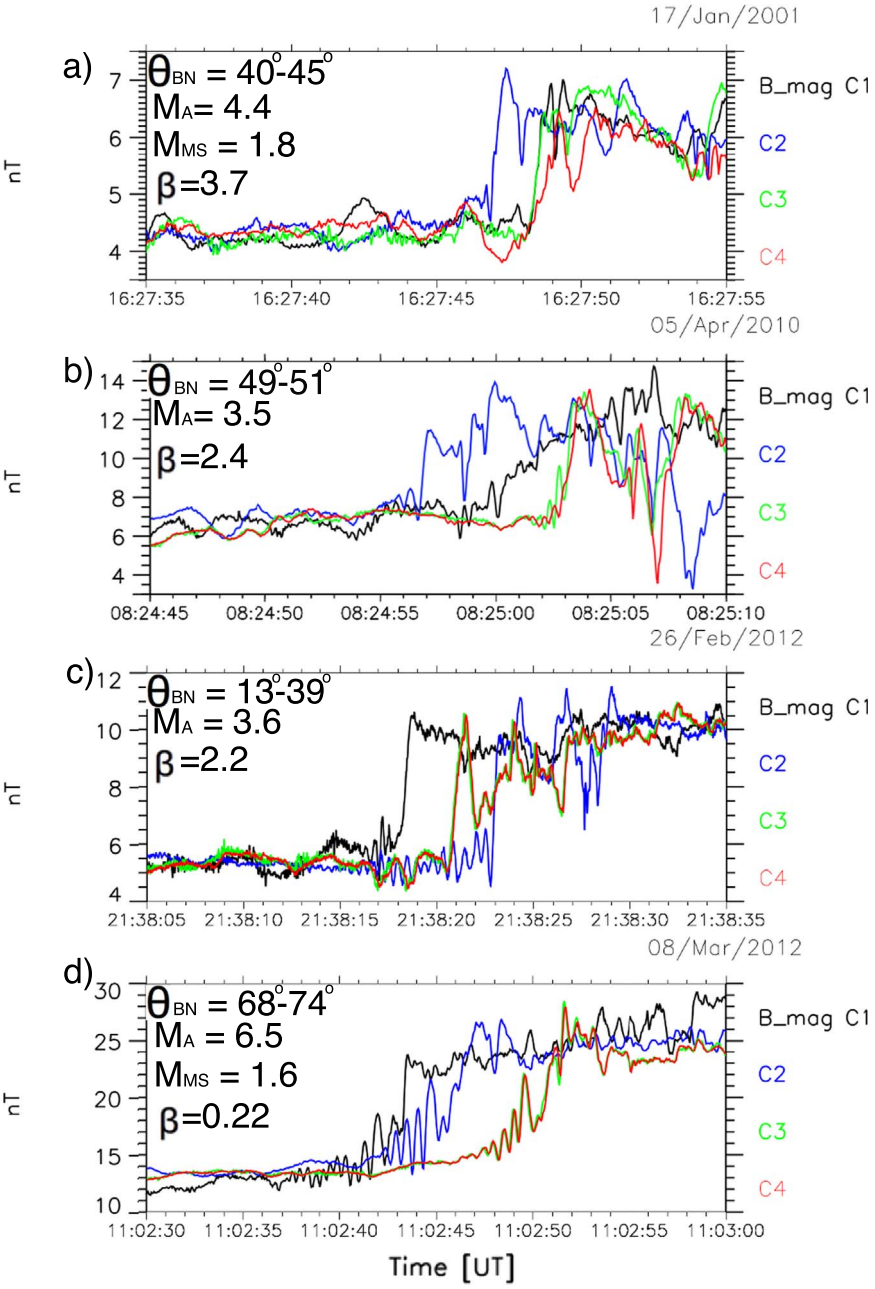

Figure 1. *B*-field profiles during four intervals when IP shocks were detected. The black, blue, red, and green lines represent the data from *C1*, *C2*, *C3*, and *C4* spacecraft, respectively.

frequencies of ∼2 Hz. In the case of *C1* the precursor lasts for ∼1.5 s while in *C2* data it lasts for ∼7 s. *C2*, *C3*, and *C4* profiles show three well defined peaks separated by two dips. Although these peaks could be some compressive waves they could also be overshoots from previous reformation cycles (see Section 3). In the case of *C2* the first peak is actually separated from the shock ramp and exhibits higher *B*-field magnitude than the actual overshoot. *C1* profile also shows these features but with much smaller amplitudes.

2.4. 2012 March 8 Shock

Our last shock was observed by *C1* at ∼11:02:43 UT (Figure 1(d)), then by *C2* about 3 s later and lastly by *C3* and *C4* spacecraft simultaneously. *C3* and *C4* were separated by 55 km (0.92 d_i), while the other separations were much larger (Table 1). *C3* and *C4* profiles are thus almost identical. All spacecraft observe whistler mode precursors upstream of the shock ramp but their appearance varies from spacecraft to spacecraft. In *C1* data the whistlers lasted for ∼7 s featuring at least three wave-trains, while the other three spacecraft observed one wave-train during ∼5 s time interval. Frequencies of these waves were ∼2 Hz and their amplitudes increased with proximity to the shock ramp. The shock ramp was steepest in *C1* data, while the other profiles show whistler waves inside the shock ramps.

3. Observations: Local Shock Normals

The θ_{BN} angles shown in Figure 1 were obtained using the magnetic coplanarity theorem. This requires averaging of upstream and downstream fields during chosen time intervals

Table 1
Results from Local Shock Normal Calculations By Using the Maximum Variance Analysis

Spacecraft	2001 Jan 17		2010 Apr 5		2012 Feb 26		2012 Mar 8	
	θ_{NN}[°]	Distance (D_i)	θ_{NN}[°]	Distance (D_i)	θ_{NN}[°]	Distance (D_i)	θ_{NN}[°]	Distance (D_i)
C1–C2	4 ± 4	15.4	29 ± 4	66.9	17 ± 2	77.8	35 ± 8	77.5
C1–C3	8 ± 3	9.3	16 ± 3	37.3	1 ± 1	24.2	29 ± 8	91.9
C1–C4	10 ± 4	14.3	11 ± 3	38.7	1 ± 1	24.3	27 ± 8	92.1
C2–C3	10 ± 3	18.1	21 ± 4	82.5	16 ± 2	64.5	8 ± 11	55.2
C2–C4	8 ± 4	18.1	22 ± 4	83.2	17 ± 2	64.7	11 ± 11	55.8
C3–C4	8 ± 3	7.4	4 ± 3	1.48	1 ± 1	0.37	3 ± 11	0.92
				θ_{BN}[°]				
C1	19		14		15		57	
C2	22		21		15		21	
C3	30		14		10		32	
C4	26		10		10		30	

Note. Top: angles between pairs of normals. Bottom: θ_{BN} angle at each spacecraft.

(but exclude the shock transition), which are then used to calculate the shock normal and θ_{BN}. Thus one obtains some time-averaged values. When multiple inter-spacecraft separations are small ($\lesssim 100\, d_i$), one would expect the shock normals calculated this way to coincide within the margin of error. This is because nonstationarity is quasi-cyclic so local shock normals and θ_{BN} vary in time around some average value (see Section 4). In order to study shock surface irregularity, we need local shock normals at the times when the shocks were observed by each spacecraft and see how they vary as a function of inter-spacecraft separation.

For this we use a novel one-spacecraft method based on the shock normal coordinate system (SNCS). The latter contains three perpendicular axes, n, l, and m. The n-axis is parallel to the shock normal, the l-axis contains a projection of the upstream B-field on the shock plane, while the m-axis completes the right-hand coordinate system. In this coordinate system only the B_l component changes from upstream to downstream.

This is of course strictly true only for MHD shocks. In the case of collisionless shocks there exist an out-of-plane component of the magnetic field produced in the shocks' foot and overshoot. However, the largest variation of the B-field is still produced due to the shock ramp itself and it occurs in the l direction.

In order to find the SNCS using a given interval, we first smooth the B-field data by using a 4 s sliding window in order to remove the upstream whistlers. We then perform minimum variance analysis (MVA; Sonnerup & Scheible 1998) of the B-field across the shock and postulate that the direction of maximum variance gives us the l direction. We also obtain two more vectors, perpendicular to l. We then rotate one of them around the l-axis and calculate the absolute value of the mean of the B-field projection along it. Once this value reaches its minimum close to 0, we take the corresponding vector to point along the m-axis and the remaining vector has to point along n.

This method is not without errors. The main sources are the intrinsic error of the MVA and the choice of time intervals used for the MVA. Details on how the errors were estimated and examples of B-field profiles of shocks in the SNCS are provided in the Appendix A and 10.5281/zenodo.2587992.

Figure 2 shows angles between pairs of normals (θ_{NN}) as a function of spacecraft separation in units of upstream d_i. The results are summarized in Table 1. It can be seen that θ_{NN} angles match very well at small spacecraft separations. As long as the spacecraft are $\lesssim 5\, d_i$ apart, their normals are within $\leqslant 4°$. As the spacecraft separation increases to $\sim 100\, d_i$, the θ_{NN} angles grow to $\sim 30°$.

Table 1 also shows local θ_{BN} angles. We estimate the errors of θ_{BN} to be $\sim \pm 5°$. These stem mostly from errors of normal directions and the errors due to selection of time intervals used for calculating the upstream B-field. It can be seen that the average θ_{BN} angles vary substantially from probe to probe.

4. Simulation Results

In order to further strengthen our case in favor of IP shock irregularity at ion scales, we use the 2D HYPSI numerical code (Burgess & Scholer 2015; Gingell et al. 2017) to carry out two simulations of collisionless shocks.

We use a grid of $N_x \times N_y = 1000 \times 800$ cell with cell size of $0.5\, d_i$ in both directions. The SW is injected at the left boundary with velocities of $3.0\, V_A$ and $4.5\, V_A$ resulting in $M_A \sim 4.4$ and 6, respectively, for the shock. The upstream β values were 2.4 and 0.2, respectively, which is close to the observed values. Density and B-field are normalized to their upstream values. Initially there were 100 simulation particles per cell. At the right boundary the particles are reflected while periodic boundary conditions are applied in the y direction. The upstream B-field lies in the simulation plane at an angle of 50° with respect to the x-axis. This is also the value of the average θ_{BN} which we denominate as $\theta_{BN,0}$.

In Figure 3(a) we show simulation results for high-β, low M_A shock at time $t = 222.5\, \Omega_i^{-1}$ (Ω_i is the upstream proton gyrofrequency) with $x = [-25,\ 25]\, d_i$ and $y = [40,\ 120]\, d_i$. Results for high-M_A shock can be seen in the Appendix B and 10.5281/zenodo.2587992. $x = 0$ is the average shock position obtained from the averaged (in y) B-field profile. The colors represent the B-field magnitude. The white curve marks the shock front determined by $B \geqslant 2.2$ and then smoothed with an 11-cell ($5.5\, d_i$) wide running window. Finally, we calculate the local shock normals (blue arrows).

In the upstream region, there are compressive structures shaded in darker-orange shades. These features are convected toward the shock surface and are the primary cause of its reformation. To show this, four animations are available in 10.5281/zenodo.2587992. Two of those animations

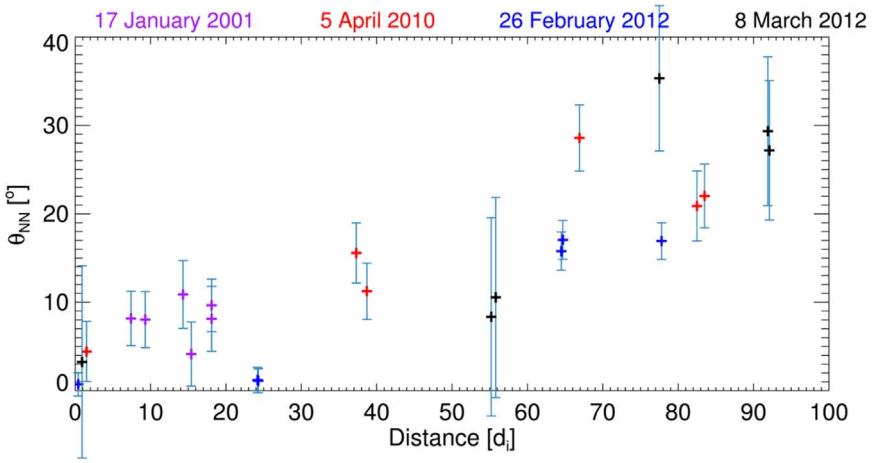

Figure 2. Angles between pairs of local shock normals shown as a function of inter-spacecraft separations in units of ion inertial lengths. The error bars show the standard deviation of θ_{NN}.

correspond to Figure 3(a)). The long animation begins at $t = 102.5\ \Omega^{-1}$, ends at $t = 327.5\ \Omega^{-1}$, and is 30 s long. The shorter animation is 5 s long and shows the shock evolution during $t = 220\ \Omega^{-1}$ and $t = 232.5\ \Omega^{-1}$. The other two animations corresponding to Figure 7(a)), have durations of 5 and 36 s and show shock evolution during time intervals of 210–232 Ω^{-1} and 52.5–317.5 Ω^{-1}, respectively. The longer animations are also available with Figures 3(a)) and 7(a)). In both cases, we can observe compressive upstream magnetic structures being convected toward the shock front. When they get really close and start touching the shock, their amplitudes rise sharply. They merge with the shock front and their upstream edges become new shock ramps.

Figure 3(b) shows four B-field profiles for $y = 50\ d_i$ (black), $60\ d_i$ (red), $65\ d_i$ (cyan), and $100\ d_i$ (magenta). The black profile exhibits a gradual rise and several downstream peaks and dips. The red profile shows upstream whistlers and a steep ramp. The cyan profile does not show any whistlers, only a steep ramp. The magenta profile exhibits a more gradual rise and a strong downstream dip.

We can see in Figure 3(a) that the upstream variations seen in black, red and cyan profiles are due to upstream structures that have arrived close to the shock and/or the whistler precursors. The multiple downstream peaks may be due to old overshoots from previous reformation cycles (red profile). The large dips seen in black and magenta profiles coincide with downstream regions with B values similar to those in the upstream region. These regions, although downstream of the shock, have not yet been fully compressed.

Figure 3(c) shows the distribution of θ_{BN} angles at time $t = 222.5\ \Omega_i$. The average and median (μ) θ_{BN} angles are close to $\theta_{BN,0}$, but the local θ_{BN} have values anywhere between $\sim 10°$ and $\sim 90°$.

Figure 3(d) shows the time evolution of the θ_{BN} for the point on the shock surface at $y = 100\ d_i$. We see that θ_{BN} oscillates around $\theta_{BN,0}$. The Fourier spectrum of the θ_{BN} variation (Figure 3(e)) reveals the presence of several periods.

Figure 3(f) shows θ_{NN} angles for all pairs of normals in panel (a) as a function of distance. These angles increase and decrease due to the shock irregularities as seen in panel (a). There is no real tendency between θ_{NN} and the distance, although θ_{NN} tend to be smaller at small distances.

The high-M_A, low-β run (see Appendix B and the 10.5281/zenodo.2587992 repository) differs from the one discussed here mainly in that upstream and downstream compressive structures and the shock exhibit larger amplitudes, the standard deviation of the θ_{BN} distribution is larger, the periods in the θ_{BN} spectra are shorter, and the shock is more structured especially at smaller separations ($\lesssim 10\ d_i$), so there is even less correlation between θ_{NN} and the distance.

5. Discussion and Conclusions

In this work we present the first direct observational evidence for an irregular surface of IP shocks at ion scales. We show four case studies (Figure 1) that were observed by the four *Cluster* probes with inter-spacecraft separations between 38 km and $\sim 10^4$ km ($0.37\ d_i$–$92\ d_i$). We show that B-field shock profiles vary from probe to probe. When the spacecraft were $\lesssim 1\ d_i$ apart (Table 1), the profiles are very similar. When the spacecraft are separated by more than $10\ d_i$ the shock profiles differ significantly. We attribute these differences to being associated with an irregular shock front.

We further strengthen our argument by calculating local shock normals at each spacecraft for which we design a new one-spacecraft analysis method (see Section 3). We plot the angle between pairs of single spacecraft normals, θ_{NN}, as a function of the distance between the probes. On average these angles tend to be smaller when the spacecraft are $\lesssim 5\ d_i$ apart and then increase as the distance increases up to $\sim 100\ d_i$.

We also calculate θ_{BN} angles at each spacecraft and show that these can be very different at different points on its surface (Table 1). This should be taken into account in any interpretation of data from IP shocks.

Our findings fit well with the 2D hybrid simulation results which show that:

1. Shock profiles and local θ_{BN} may vary significantly at separations of the order of $5\ d_i$ and more.
2. At any given time, different locations on the shock surface exhibit values of θ_{BN} anywhere between 10° and 90°.
3. The geometry at the particular point on the shock surface varies with time and the location on the shock surface.
4. The cause of irregularities of observed shocks may be upstream magnetic structures that are convected toward

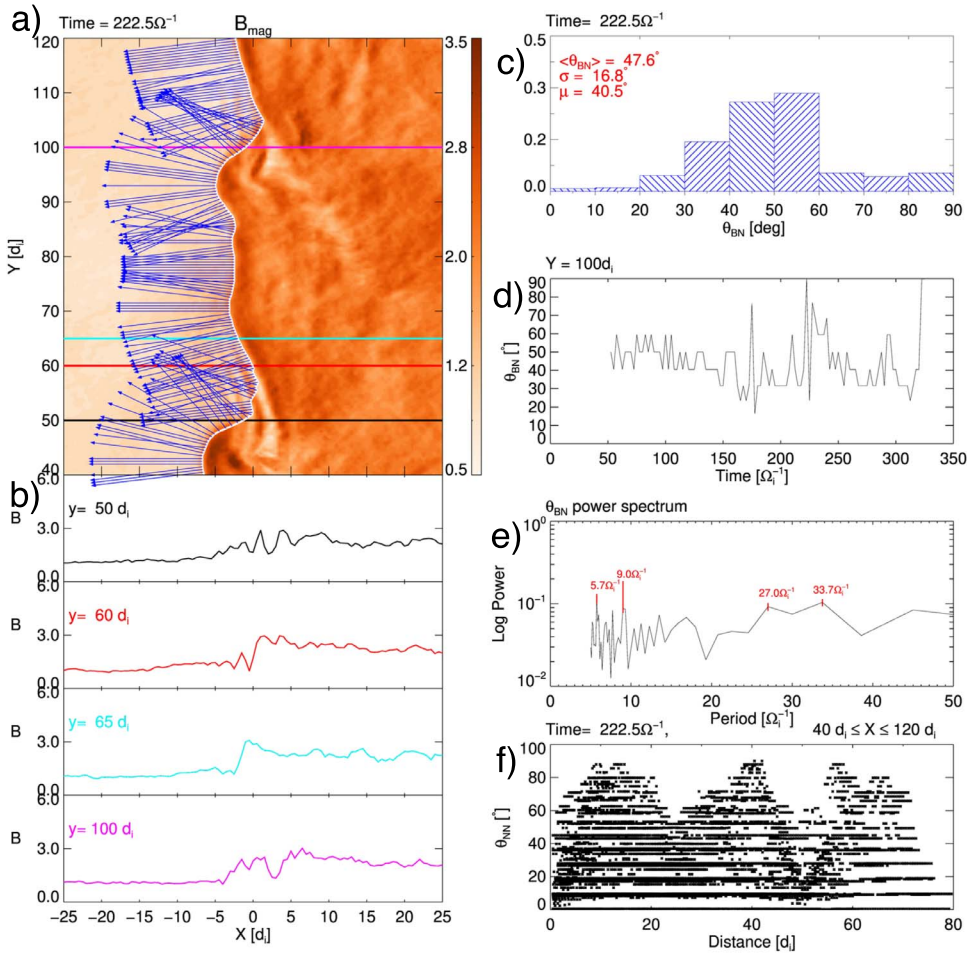

Figure 3. Simulation results from the 2D HYPSI run at the simulation time $t = 222.5\ \Omega_i^{-1}$. (a) B-field magnitude. $x = 0$ is the coordinate of the shock obtained from the average (over y) B-field profile. Horizontal lines show the coordinates of the B-field profiles shown on panel (b). White curve marks the shock surface. (b) B-field profiles at $y = 50\ d_i$ (black), $60\ d_i$ (red), $65\ d_i$ (cyan), and $100\ d_i$ (magenta). (c) Histogram of all angles θ_{BN} on the shock surface at $t = 11.25\ \Omega_i^{-1}$. (d) Evolution of θ_{BN} for a point on the shock surface with $y = 100\ d_i$. (e) Power spectrum of θ_{BN}. (f) θ_{NN} as a function of distance between pairs of normals shown in panel (a). An animation of panels (a) and (b) is available. The animation begins at $t = 102.5\ \Omega^{-1}$ and ends at $t = 327.5\ \Omega^{-1}$. The video duration is 30 s.

(An animation of this figure is available.)

the shocks. These can arise due to a small amount of backstreaming ions reflected by the shocks.

The fact that irregularities of simulated shock surfaces may occur at quite small spatial scales is not reflected in our observations (Figure 2), possibly due to the low number of our case studies.

In the 10.5281/zenodo.2587992 repository and Appendix B we show that fluctuations in the ULF frequency range (0.01–0.1 Hz) exist upstream of all four shocks (Figure 1), although in the case of the 2012 February shock their compressive component is weak. These fluctuations could be responsible for irregular structure of observed shocks.

There is a possibility that the upstream B-field fluctuations have already been present in the upstream SW and the shocks just caught up with them. In the 10.5281/zenodo.2587992 and Appendix B we show ion spectra for the 2001 January and 2010 April shocks in Figure 2. The ion particle energy flux peaks at shock transitions, suggesting the ions are accelerated by the IP shocks (for the other two shocks the data were not available). In the case of the 2010 April shock part of these ions and ULF fluctuations may have actually come from the Earth's bow-shock, as the data suggest that the *Cluster* probes have entered and exited it on several occasions before the IP shock arrival. These excursions are marked by increased suprathermal ion fluxes (green trace in the middle panel of the Figure 2(b)). The last excursion into the foreshock occurred ∼20 minutes prior to the IP shock arrival and may have lasted some minutes after the shock was observed.

Authors acknowledge ClWeb and *Cluster* Science Archive teams for easy access and visualization of the data. P.K.'s work was supported by PAPIIT grant IA101118. X.B.C.'s work was supported by PAPIIT IN-105218 and Conacyt 255203 grants. D.T. acknowledges support of a studentship funded by the Perren Fund of the University of London. The authors acknowledge support from the Royal Society Newton International Exchange Scheme (Mexico) grant NI150051. Simulations were run on MIZTLI supercomputer in the frame of DGTIC LANCAD-UNAM-DGTIC-337 grant.

Appendix A

In this section we explain how the shock normals were calculated and how the errors of θ_{NN} and θ_{BN} were estimated.

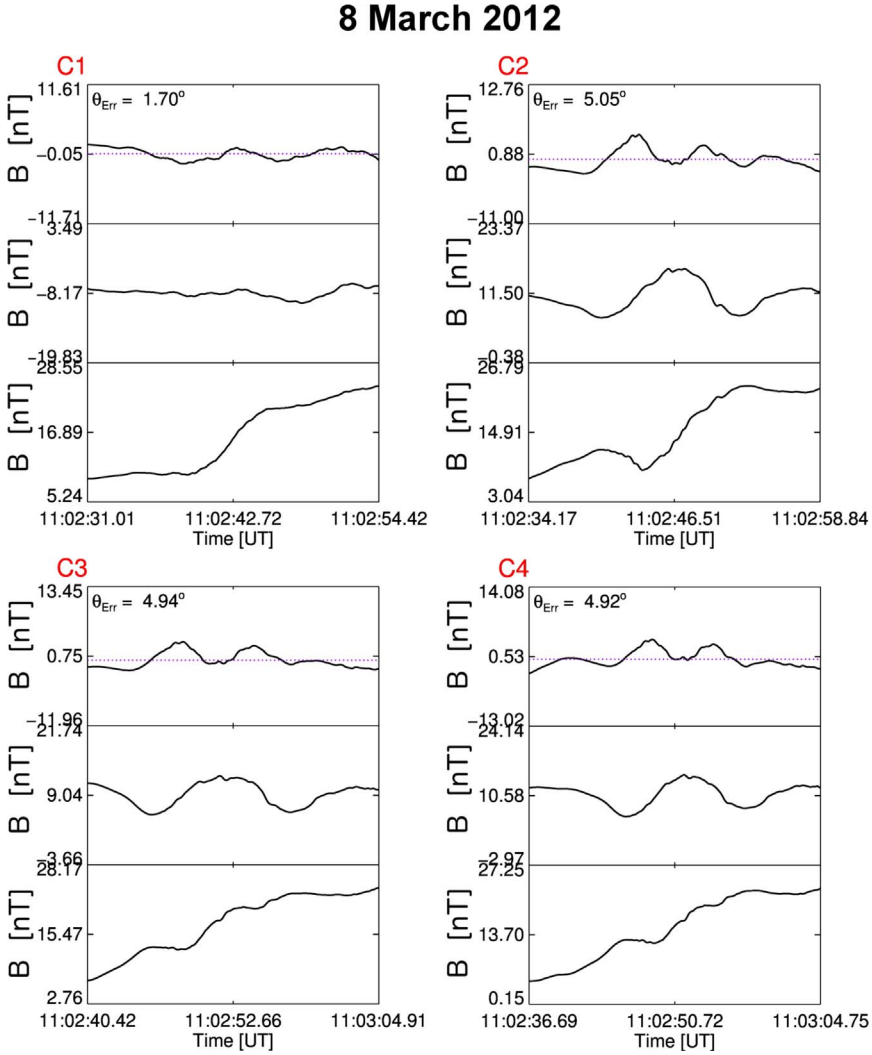

Figure 4. Magnetic field profiles of the 2012 March shock. The *B*-field components are in the shock-normal coordinate system. The dotted horizontal lines indicate zero value. All 160 profiles may be seen in the supplement located online at http://usuarios.geofisica.unam.mx/primoz/IPShockRipplingSupplement/SNCS.pdf and in the 10.5281/zenodo.2587992 repository.

There are two main sources of errors. The first is the error of the MVA method itself which depends on the number of measurement points and the calculated eigenvalues (Sonnerup & Scheible 1998):

$$\theta_{\rm Err} = \sqrt{\frac{\lambda_3}{M-1}\frac{\lambda_2}{\lambda_2-\lambda_3}}. \quad (1)$$

Here λ_2, λ_3, and M are the intermediate and minimum eigenvalues and the number of measurement points, respectively. This error is stated in the Figure 4.

The second source of errors comes from determining time intervals that are used for the MVA. These intervals need to include the shock transition but also some upstream and downstream regions. One needs to select the intervals carefully so not to include large *B*-field rotations that are not associated with shocks and could affect the determination of the direction of maximum variance. We select the time intervals by hand. We repeat the process for each shock and spacecraft 10 times. We then proceed to calculate angles between pairs of normals from different spacecraft (θ_{NN}) and calculate the the average angles and the error of the mean. Next we sum this error with $\theta_{\rm Err}$ in order to estimate the total error of our method. The latter is shown in Table 1 and in Figure 2 in the form of error bars.

The θ_{BN} errors stem from the MVA method and the selection of the upstream time intervals over which we calculate the average *B*-field direction. They are typically ∼15 s long. After repeating this selection 10 times we estimate the errors to be ∼5°.

Appendix B

Here we present (a) wavelet spectra of magnetic field fluctuations observed by *Cluster* 1 spacecraft upstream of the four interplanetary (IP) shocks (Appendix B.1); (b) ion spectrograms and energy fluxes around two of the shocks for which the data were available (Appendix B.2); and (c) simulation results of our high-$M_{\rm A}$, low-β run (Appendix B.3).

B.1. Wavelet Spectra of Upstream Waves

Figure 5 shows magnetic field data and the corresponding wavelet spectra for the four IP shocks observed on 2001

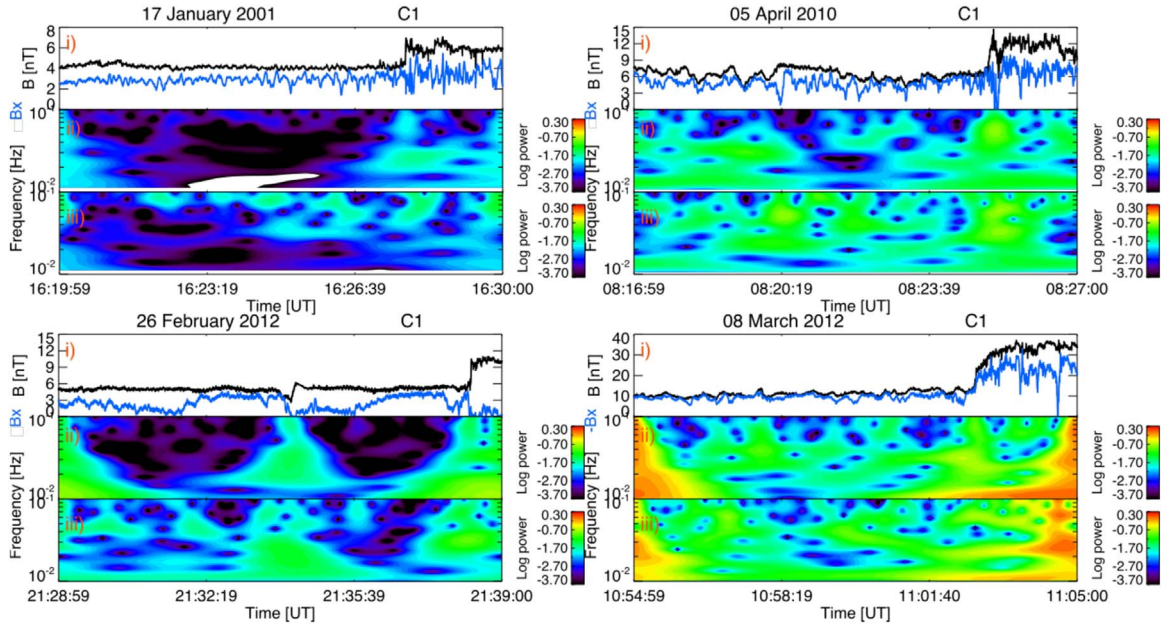

Figure 5. Magnetic field data and wavelet spectra during time periods when the four IP shocks were observed. Black traces on panels labeled (i) represent the magnetic field magnitude. Blue traces on panels labeled (i) show the $B_{x,\mathrm{GSE}}$ or $-B_{x,\mathrm{GSE}}$ magnetic field component. Panels labeled (ii) and (iii) exhibit wavelet spectra of the B and B_x, respectively.

January 17, 2010 April 5, 2012 February 26, and 2012 March 3. Panels labeled (i) show B-field magnitude data as black lines, while the $B_{x,\mathrm{GSE}}$ or $-B_{x,\mathrm{GSE}}$ component is represented by the blue line. Panels labeled (ii) and (iii) exhibit B and $B_{x,\mathrm{GSE}}$ wavelet spectra, respectively. We can see that compressive and/or transverse B-field fluctuation in the frequency range 10^{-2}–10^{-1} Hz is present upstream of all four shocks. In general, there is more power in the transverse component of these fluctuations than in the compressive component.

B.2. Particle Data

Figure 6 shows magnetic field, particle spectrogram, and particle energy fluxes at time when (a) 2001 January 17 and (b) 2010 April 5 shocks were observed. In both cases the suprathermal ion energy fluxes in units (in units of keV/(s cm^{-2} sr keV)) start increasing before the shock arrival and peak at shock transition, suggesting that they are accelerated by the shocks. The suprathermal ion energy flux (and magnetic ULF fluctuations) in the case of the 2010 April 5

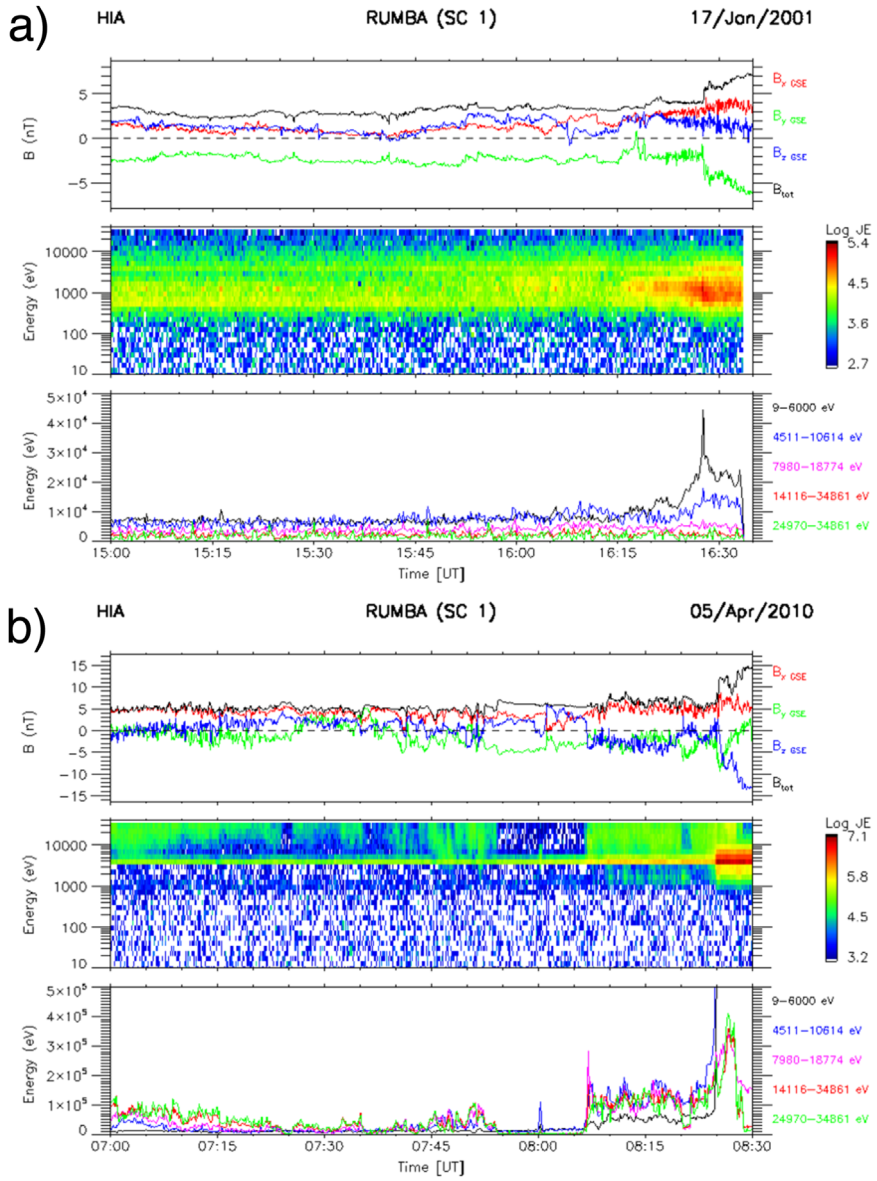

Figure 6. Panels (a) and (b) show magnetic field data from FGM and particle spectrograms and fluxes for 2001 January 17 and 2010 April 5 shocks.

could partially arrive from the Earth's bow-shock, because the ion spectrogram suggests that prior to and possibly during the shock encounter, the Earth's foreshock has been observed intermittently.

B.3. Simulation Results for high-M_A*, low-*β *Run*

Figure 7(a) shows results from our high-M_A (=6.5), low-β (=0.2) run at time $t = 112.5\ \Omega_i^{-1}$) with $x = [-25, 25]\, d_i$ and

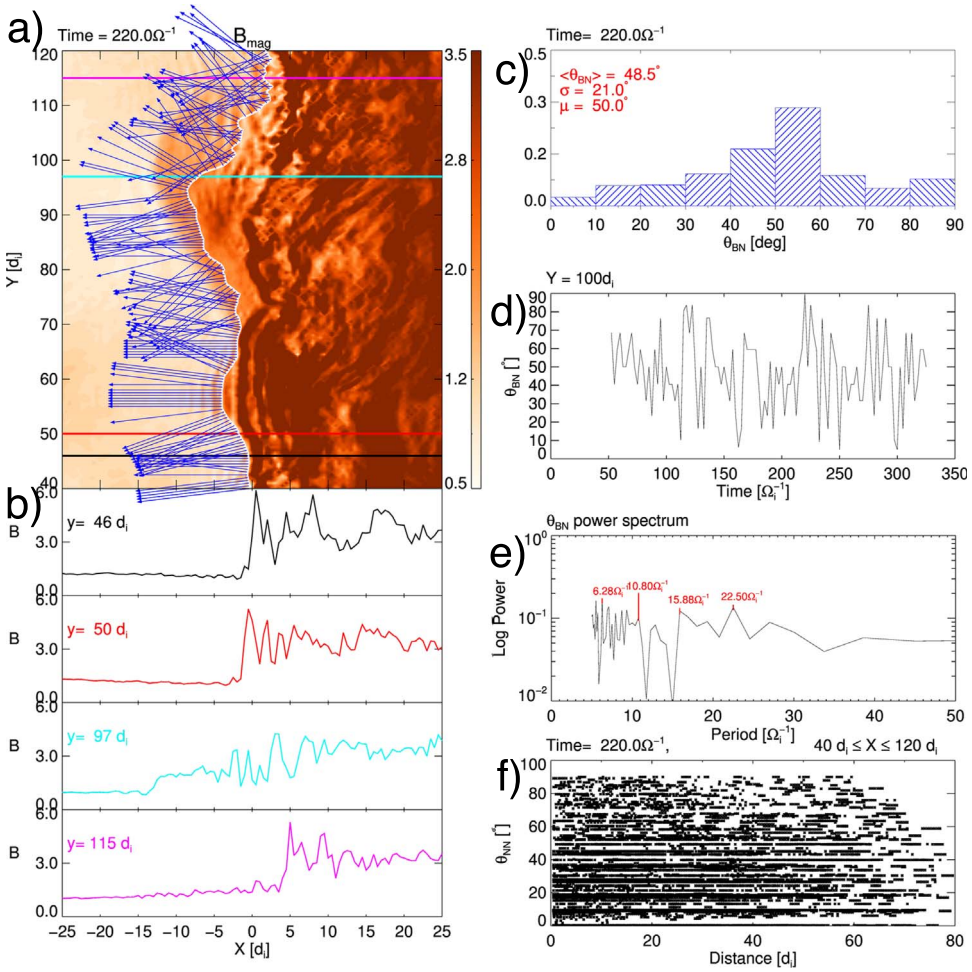

Figure 7. Results from our high-M_A, low-β run. An animation of panels (a) and (b) is available. The animation begins at $t = 52.5\ \Omega^{-1}$ and ends at $t = 317.5\ \Omega^{-1}$. The video duration is 36 s.

(An animation of this figure is available.)

$y = [40, 120]\, d_i$. $x = 0$ is the average shock position obtained from the averaged (in y direction) B-field profile. The colors represent the B-field magnitude. The white curve marks the shock front and blue arrows show the directions of local shock normals.

Figure 7(b) shows four B-field profiles for $y = 46\, d_i$ (black), $50\, d_i$ (red), $97\, d_i$ (cyan), and $115\, d_i$ (magenta). Animations for this run can be found at http://usuarios.geofisica.unam.mx/primoz/IPShockRipplingSupplement/ and are titled BfieldLowBeta.avi, BfieldHighLowShort.avi.

Figure 7(c) shows the distribution of θ_{BN} angles at time $t = 112.5\ \Omega_i$.

Figure 7(d) shows the time evolution of the θ_{BN} for the point on the shock surface at $y = 97\, d_i$.

Figure 7(e) shows θ_{NN} angles for pairs of normals shown on panel (a).

ORCID iDs

Primož Kajdič https://orcid.org/0000-0002-0625-8892
Luis Preisser https://orcid.org/0000-0002-5636-2014
Xóchitl Blanco-Cano https://orcid.org/0000-0001-7171-0673
David Burgess https://orcid.org/0000-0002-8175-9056
Domenico Trotta https://orcid.org/0000-0002-0608-8897

References

Balogh, A., Carr, C. M., Acuña, M. H., et al. 2001, AnGeo, 19, 1207
Balogh, A., Dunlop, M. W., Cowley, S. W. H., et al. 1997, SSRv, 79, 65
Biskamp, D., & Welter, H. 1972, JGR, 77, 6052
Blanco-Cano, X., Kajdič, P., Aguilar-Rodrguez, E., et al. 2016, JGRA, 121, 992
Burgess, D. 1989, GeoRL, 16, 345
Burgess, D. 2006a, JGRA, 111, a10210
Burgess, D. 2006b, ApJ, 653, 316
Burgess, D., & Scholer, M. 2015, Collisionless Shocks in Space Plasmas: Structure and Accelerated Particles (Cambridge: Cambridge Univ. Press)
Escoubet, C., Schmidt, R., & Goldstein, M. 1997, SSRv, 79, 11
Gedalin, M. 2001, JGRA, 106, 21645
Gingell, I., Schwartz, S. J., Burgess, D., et al. 2017, JGRA, 122, 11003
Gosling, J., & Pizzo, V. 1999, SSRv, 89, 21
Gosling, J. T., Asbridge, J. R., Bame, S. J., Paschmann, G., & Sckopke, N. 1978, GeoRL, 5, 957
Hao, Y., Lembege, B., Lu, Q., & Guo, F. 2016, JGRA, 121, 2080
Hellinger, P., Trvnek, P., Lembge, B., & Savoini, P. 2007, GeoRL, 34, L14109
Hietala, H., Laitinen, T. V., Andréeová, K., et al. 2009, PhRvL, 103, 245001
Horbury, T. S., Cargill, P. J., Lucek, E. A., et al. 2001, AnGeo, 19, 1399
Horbury, T. S., Cargill, P. J., Lucek, E. A., et al. 2002, JGRA, 107, 1208
Johlander, A., Schwartz, S. J., Vaivads, A., et al. 2016, PhRvL, 117, 165101
Kajdič, P., Hietala, H., & Blanco-Cano, X. 2017, ApJL, 849, L27
Koval, A., & Szabo, A. 2010, JGRA, 115, A12105
Krauss-Varban, D., Li, Y., & Luhmann, J. G. 2008, in AIP Conf. Proc. 1039, Particle Acceleration and Transport in the Heliosphere and Beyond, ed. G. Li (Melville, NY: AIP), 307
Krauss-Varban, D., & Omidi, N. 1991, JGRA, 96, 17715

Lembge, B., Savoini, P., Hellinger, P., & Trvnek, P. M. 2009, JGRA, 114, A03217
Leroy, M. M., Winske, D., Goodrich, C. C., Wu, C. S., & Papadopoulos, K. 1982, JGRA, 87, 5081
Lobzin, V. V., Krasnoselskikh, V. V., Musatenko, K., & Dudok de Wit, T. 2008, AnGeo, 26, 2899
Lowe, R. E., & Burgess, D. 2003, AnGeo, 21, 671
Marshall, W. 1955, Proc. R. Soc. London, Ser. A, 233, 367
Moullard, O., Burgess, D., Horbury, T. S., & Lucek, E. A. 2006, JGRA, 111, A09113
Ofman, L., & Gedalin, M. 2013, JGRA, 118, 5999
Pulupa, M., & Bale, S. D. 2008, ApJ, 676, 1330
Russell, C., & Alexander, C. 1984, AdSpR, 4, 277
Russell, C. T., Wang, Y. L., Raeder, J., et al. 2000, JGRA, 105, 25143
Sagdeev, R. Z. 1966, RvPP, 4, 23
Scholer, M., & Burgess, D. 2007, PhPl, 14, 072103
Schwartz, S. J., & Burgess, D. 1991, GeoRL, 18, 373
Sheeley, N. R., Howard, R. A., Koomen, M. J., et al. 1985, JGRA, 90, 163
Sonnerup, B. U. Ö., & Scheible, M. 1998, in Analysis Methods for Multi-Spacecraft Data, ed. G. Paschmann & P. Daly (Noordwijk: ESA), 185
Szabo, A. 2005, in AIP Conf. Proc. 781, The Physics of Collisionless Shocks, ed. G. Li, G. P. Zank, & C. T. Russell (Melville, NY: AIP), 37
Szabo, A., Lepping, R. P., Merka, J., Smith, C. W., & Skoug, R. M. 2001, in Proc. First Solar Orbiter Workshop ESA SP-493, Solar Encounter, ed. B. Battrick & H. Sawaya-Lacoste (Noordwijk: ESA), 383
Szabo, A., Smith, C. W., & Skoug, R. M. 2003, in AIP Conf. Proc. 679, Solar Wind Ten, ed. M. Velli, R. Bruno, & F. Malara (Melville, NY: AIP), 782
Winske, D., & Quest, K. B. 1988, JGRA, 93, 9681
Yang, J., Toffoletto, F. R., Wolf, R. A., & Sazykin, S. 2011, JGRA, 116, A05207
Yang, Z., Lu, Q., Liu, Y. D., & Wang, R. 2018, ApJ, 857, 36

Capítulo 2

La influencia de He^{++} y θ_{Bn} en los choques interplanetarios usando simulaciones numéricas híbridas.

2.1. Resumen del trabajo y metodología

En este trabajo se investigó la influencia que tiene el contenido de partículas alfa (He^{++}) en la evolución temporal y espacial de choques sin colisiones con características similares a las reportadas observacionalmente en el medio interplanetario e.g. $M_A \sim 4.4$, que puede ser considerado como un valor estadístico intermedio-alto para éstos (Blanco-Cano et al., 2016). Se realizó un grupo de simulaciones 2D con las mismas escalas espaciales (i.e. tamaños de las cajas de la simulación) generadas por el código híbrido HYPSI (Burgess and Scholer, 2015; Gingell et al., 2017). Hay que recalcar que no hay muchos estudios que incorporen He^{++} en el análisis de los choques.

Para este estudio paramétrico se realizaron simulaciones con diferentes valores iniciales del ángulo θ_{Bn} a saber, 15°, 30°, 50° y 65°, para cada una de los cuales se varió el porcentaje de He^{++} (1, 5 y 10 %) dando un total de 12 simulaciones. De los datos arrojados por las simulaciones se analizó la evolución temporal de diferentes parámetros tales como el campo magnético, la densidad y la anisotropía de la temperatura tanto para protones como

He^{++}. Además se analizaron estos parámetros a un tiempo dado para el cual el choque había evolucionado lo suficiente, alcanzando la mitad del dominio de la simulación. De los datos correspondientes a este tiempo se calcularon también las funciones de distribución de ambas especies cerca de la interfaz del choque y en regiones lejanas a éste para la geometría más parecida a un choque paralelo (i.e. θ_{Bn} =15°) y más parecida a un choque perpendicular (i.e. θ_{Bn} =60°).

Nuestro estudio revela que los cambios en la transición del choque así como en los perfiles de la anisotropía de temperatura son función tanto de la geometría del choque como de la abundancia de He^{++}. El cambio en el valor de θ_{Bn} modifica la eficiencia con la que las partículas pueden escapar hacia la región río arriba del choque facilitando o no la formación de estructuras magnéticas compresivas lo que a su vez produce incrementos en la anisotropía de la temperatura. Las regiones donde hay mayor anisotropía en la temperatura coinciden con aquellas donde las fluctuaciones compresivas del campo magnético están presentes. El tamaño de estas regiones está modulado por la concentración de He^{++} en la simulación, tendiendo a ser mas extensas y con mayor amplitud en las fluctuaciones magnéticas a medida que el contenido de He^{++} aumenta. Las funciones de distribución para ambas especies de partículas también resultan ser diferentes debido, principalmente, a la geometría del choque que tiende a isotropizar a éstas de manera más eficiente para valores $\theta_{Bn} \leq 50°$. Para $\theta_{Bn} = 65°$ debido a la diferencia en el parámetro q/m (donde q y m son la carga y masa de cada especie respectivamente), la función de distribución de He^{++} forma un anillo en el plano V_x-V_z (con V_x y V_z las componentes de la velocidad a lo largo del eje x y z respectivamente).

Ya que para el choque con $\theta_{Bn} = 65°$ la anisotropía en la región río abajo aumenta de manera abrupta para ambas especies (protones y He^{++}) y es mayor con respecto a las demás simulaciones con otras geometrías, se realizó un análisis para el crecimiento de ondas ion/ciclotrón y modo mirror (Gary, 1993). Para el estudio de las ondas ion/ciclotrón se usó la condición $T_\perp/T_\parallel < 1+\beta_\parallel^{0.5}$ (donde los subíndices $\parallel$ y $\perp$ indican el cálculo de los parámeros en dirección paralela y perpendicular al campo magnético local respectivamente) basada en el trabajo observacional de Anderson et al. (1996) mientras que para las ondas modo mirror se usó el umbral teórico $T_\perp/T_\parallel > 1 + 1/\beta_\perp$ basado en el trabajo de Southwood and

Kivelson (1993) y Gary (1993). Dicho análisis se realizó para el caso con 1 % y 10 % de He^{++}. Los resultados demuestran que las ondas ion/ciclotrón pueden crecer río abajo en regiones extensas ($\geq 50 d_i$) en comparación con las ondas mirror que tienden a crecer solo cerca del choque y abarcar regiones más estrechas ($<10 d_i$). El incremento en el contenido de He^{++} en la simulación tiende a facilitar el crecimiento de ondas mirror, disminuyendo el crecimiento de las ondas ion/ciclotrón.

2.2. Publicación en Journal of Geophysical Research (JGR) (2020)

JGR Space Physics

RESEARCH ARTICLE
10.1029/2019JA027442

Influence of He^{++} and Shock Geometry on Interplanetary Shocks in the Solar Wind: 2D Hybrid Simulations

L. Preisser[1], X. Blanco-Cano[1], D. Trotta[2], D. Burgess[2], and P. Kajdič[1]

[1]Instituto de Geofísica, Universidad Nacional Autónoma de México, Circuito de la investigación Científica s/n, Ciudad Universitaria, Delegación Coyoacán, Mexico City, Mexico, [2]School of Physics and Astronomy, Queen Mary University of London, London, UK

Key Points:
- He^{++} content modifies the shock profile, temperature anisotropy, and distribution functions in the upstream and downstream regions
- θ_{Bn} and He^{++} content affects the efficiency with which particles escape to the upstream region
- Increase in magnetic fluctuations and He^{++} content modify regions with higher temperature anisotropy downstream of quasi-perpendicular shocks

Supporting Information:
- Supporting Information S1
- Figure S1
- Figure S2

Correspondence to:
L. Preisser,
preisser@igeofisica.unam.mx

Citation:
Preisser, L., Blanco-Cano, X., Trotta, D., Burgess, D., & Kajdič, P. (2020). Influence of He^{++} and shock geometry on interplanetary shocks in the solar wind: 2D Hybrid simulations. *Journal of Geophysical Research: Space Physics*, *125*, e2019JA027442. https://doi.org/10.1029/2019JA027442

Received 9 OCT 2019
Accepted 1 APR 2020
Accepted article online 16 APR 2020

Abstract After protons, alpha particles (He^{++}) are the most important ion species in the solar wind, constituting typically about 5% of the total ion number density. Due to their different charge-to-mass ratio, protons and He^{++} particles are accelerated differently when they cross the electrostatic potential in a collisionless shock. This behavior can produce changes in the velocity distribution function (VDF) for both species generating anisotropy in the temperature, which is considered to be the energy source for various phenomena such as ion cyclotron and mirror mode waves. How these changes in temperature anisotropy and shock structure depend on the percentage of He^{++} particles and the geometry of the shock is not completely understood. In this paper, we have performed various 2D local hybrid simulations (particle ions, massless fluid electrons) with similar characteristics (e.g., Mach number) to interplanetary shocks for both quasi-parallel and quasi-perpendicular geometries self-consistently including different percentages of He^{++} particles. We have found changes in the shock transition behavior as well as in the temperature anisotropy as functions of both the shock geometry and He^{++} particle abundance: The change of the initial θ_{Bn} leads to variations of the efficiency with which particles can escape to the upstream region facilitating or not the formation of compressive structures in the magnetic field that will produce increments in perpendicular temperature. The regions where both temperature anisotropy and compressive fluctuations appear tend to be more extended and reach higher values as the He^{++} content in the simulations increases.

1. Introduction

Collisionless shocks are a phenomenon of crucial importance in heliospheric/space plasma physics and astrophysics. Along with solar flares, they are the main particle accelerators near the Sun and in the interplanetary (IP) medium. The energy dissipation produced by collisionless shocks is a complex consequence of the interaction between particles and the electric and magnetic fields at the shock interface together with wave-particle interactions in the wave field driven by instabilities at the shock and in the upstream and downstream regions. In addition, due to the lack of collisions, a small fraction of particles can be reflected toward the upstream side of the shocks, reaching high energies (Burgess & Scholer M., 2015; Gosling & Thomsen, 1985; Gosling et al., 1989).

Depending on the shock normal angle θ_{Bn}, defined as the angle between the upstream magnetic field and the shock normal direction, collisionless shocks can be divided in two types: quasi-parallel ($\theta_{Bn} < 45°$) and quasi-perpendicular ($\theta_{Bn} > 45°$). Ion acceleration at the shock can be caused by different processes: Shock drift acceleration (Burgess, 1987a) is usually considered to be the main mechanism operating in quasi-perpendicular shocks, while diffusive shock acceleration (Blandford & Ostriker, 1978) works more efficiently in quasi-parallel shocks (see Burgess & Scholer M., 2015, for a detailed description).

In quasi-parallel shocks, the reflected ions can escape back to the upstream side along the magnetic field lines where their interaction with the solar wind (SW) particles can lead to excitation of upstream waves including ultra-low-frequency (ULF) waves, which can evolve into shocklets, and other large-amplitude magnetic structures (Blanco-Cano, 2016; Russell & Hoppe, 1983; Wilson, 2016). Consequently, the region upstream of a quasi-parallel shock is intimately linked to the generation of high-energy upstream ions and is in particular related to the extraction of thermal particles from the upstream side of the shock into the population of energetic ions (Burgess, 2005; Scholer & Burgess, 1992, 1993; Su et al., 2012a, 2012b; Sundberg et al., 2016).

In quasi-perpendicular shocks, the specularly reflected ions gyrate in the upstream magnetic field generating a foot region, penetrating the shock potential back to the downstream side with high tangential velocities, producing an anisotropic distribution with the perpendicular temperature larger than the parallel one near the shock front. Linear theory and simulations have shown that such an anisotropic distribution can be unstable to ion cyclotron and mirror mode waves (Gary,1993; Hada et al., 2003; Lembège & Savoini, 1992; Yang et al., 2009, 2012). These waves have been observed in the Earth's magnetosheath behind the quasi-perpendicular bow shock (Anderson & Fuselier, 1993), downstream of shocks associated to stream interaction regions (SIRs) (Blanco-Cano, 2016) and also in complex events formed by two or more large-scale solar wind structures that interact in the interplanetary space (Enriquez-Rivera et al., 2010, 2013; Siu-Tapia et al., 2015).

In the solar wind, the shock interface conditions are basically determined by the dynamics of protons, which are the most abundant ion species. However, there are also various kinds of minor ions. Among these, He^{++} is the most important ion species and although it constitutes typically only about 4–5% of the total ion number density (Ipavich et al., 1984; Neugebauer & Snyder, 1966; Wurz, 2005), its contribution to the upstream mass density and dynamical pressure can be as large as 20%. Therefore, He^{++} effects in shock dynamics should not be ignored as has been pointed previously (Geiss et al., 1970; Gedalin, 2017; Kasper et al., 2007).

One of the most interesting features that hybrid simulations of quasi-parallel shocks have revealed is a cyclic behavior (Burgess, 1989a) in their structure above an Alfvénic Mach number of $M_A = V_u/V_A \sim 2$: upstream waves are convected toward the shock, being compressed as they approach producing a gradual shock profile. These arriving waves steepen up at the upstream edge which becomes the newly reformed shock (Burgess, 1989a; Hao et al., 2016; Scholer & Terasawa, 1990). In 1D simulations of quasi-parallel shocks with $\theta_{Bn} \gtrsim 20°$, the low frequency upstream waves evolve to large amplitude pulsations very close to the shock to later interact with the shock, producing an associated increased density of diffuse and/or nearly specularly reflected ions. At 1 AU the observations of interplanetary shocks show different micro-structure even for similar θ_{Bn} values (Blanco-Cano, 2016; Kajdic et al., 2012). This can be attributed to time evolution of the shock front and/or local geometry irregularities, which have been reported and studied at different spatial scales via multispacecraft analysis and hybrid simulations (Aguilar-Rodriguez et al., 2011; Kajdic et al., 2019).

In the past, quasi-parallel hybrid simulations with He^{++}as second heavy ion species have been performed (Trattner & Scholer, 1991, 1994), showing that solar wind alpha particles penetrate the shock ramp rather unaffected and gyrate in the downstream magnetic field. In the case of low (~ 0.1) upstream β (ratio of thermal to magnetic pressures), this gyration is in general well behind the shock ramp, and no diffuse alpha particles are generated. However, occasionally the whole distribution is able to gyrate back to the shock ramp and gets accelerated into the upstream region by the electric field in the shock ramp. This leads to the formation of localized backstreaming He^{++} clouds, which are the source of diffuse alpha particles. At higher Mach number ($M_A \sim 9$), the gyroradii increase, which makes it easier for the beam-like alpha particles behind the shock to reach the shock ramp for a second time. This causes a strong increase of the number of backstreaming alpha particles. Trattner & Scholer (1993) performed 1D hybrid simulations with different alpha particles to proton ratio. Assuming an upstream alpha particle-to-proton temperature ratio (T_α/T_p) of 4, the downstream temperature ratio of alpha particles to protons was enhanced ($\sim$ 5-7). A recent work (Caprioli et al., 2017) has studied the thermalization, injection, and acceleration of ions with different mass/charge ratios (A/Z) in nonrelativistic collisionless shocks via hybrid simulations finding that in general, ions thermalize to a postshock temperature proportional to A. When diffusive shock acceleration was efficient, the ions develop a nonthermal tail whose extent scales with Z, so that incompletely ionized heavy ions are preferentially accelerated.

Various works concerning quasi-perpendicular shock hybrid simulations including He^{++} ions (McKean et al., 1995a, 1996) have been carried out in order to study the wave evolution in the downstream region for low and high Mach number (M_A) shocks. These works show how the proton cyclotron and mirror mode waves can be excited near the shock front to be convected further downstream. The energy of the proton cyclotron waves driven by the proton temperature anisotropy $T_\perp/T_\parallel > 1$ (e.g., Gary et al., 1996) can be absorbed by the He^{++} particles leading to thermalized He^{++} distributions. In these simulated shocks, both ion species are decelerated differently due to their different charge-mass ratios when they cross the electrostatic shock potential, producing the formation of a ring-beam distribution of He^{++} downstream of the shock

(Fuselier & Schmidt, 1994, 1997; Lu & Wang, 2006). This He^{++} ring-beam distribution can drive helium cyclotron waves, which then scatter He^{++} into a shell-like distribution (Hao et al., 2014; Lu & Wang, 2005, 2006). Geotail spacecraft recent observations have made it possible to identify stable He^{++} ring beams in velocity space perpendicular to the magnetic field generated during a bow shock crossing (Tsubouchi et al., 2016). In the context of interplanetary shocks, a recent work (Ofman et al., 2019) compares the observed magnetic and density structure of different oblique shocks at 1 AU with 2D hybrid simulations to demonstrate the effects of He^{++} on the magnetic and density profiles, the dynamics of the downstream shock oscillations as well as the nonstationarity of the shocks.

Given the presence of He^{++} in the solar wind, in this work, we investigate its influence on different interplanetary shock signatures performing a group of 2D hybrid simulations of collisionless shocks (Burgess, 1987; Krauss-Varban, 2005; Winske & Leroy, 1985). We use the HYPSI code (Burgess et al., 2015; Gingell, 2017; Trotta & Burgess, 1994) varying the He^{++} number density fraction (1%, 5%, and 10%) and shock geometry ($\theta_{Bn} = 15°$, 30°, 50°, and 65°) for an intermediate Alfvén Mach number ($M_A \sim 4.4$) similar to IP shocks. In this context, observational IP shocks with parameters similar to those presented here can be found in the WIND data set (https://ipshocks.fi/) where, for instance, 48 fast forward IP shocks with Mach numbers ($4 < M_A < 5$) are listed covering $0.46 < \beta < 13.07$ and $8° < \theta_{Bn} < 88°$ as well as in past investigations (Blanco-Cano, 2016) and recent case-study works (Enriquez-Rivera et al., 2013; Ofman et al., 2019) where observational He^{++} content is similar to the values in our study. This work is organized as follows: In section 2, we describe the hybrid simulation model and setup, the simulation results are presented in section 3, and in section 4, we discuss and summarize our results.

2. Simulation Setup

We performed 2D hybrid simulations to investigate the influence of He^{++} on shock dynamics and particle thermalization for different θ_{Bn} initial values and different number content of He^{++} particles. The two dimensional simulations were performed using the hybrid Particle-In-Cell (PIC) code HYPSI (Burgess et al., 2015; Sundberg et al., 2016), which is based on the CAM-CL (see Matthews, 1994for details) algorithm. Under this approach, protons and He^{++} particles are treated kinetically and advanced using the standard PIC method. Electrons are considered as a charge-neutralizing massless fluid (see A.3 in Burgess & Scholer M., 2015). Electron inertial and kinetic effects are assumed to be negligible.

Spatial and temporal scales in the simulation are expressed in units of proton inertial length $d_i = c/\omega_p$ (where ω_p is the proton plasma frequency and c is the speed of light) and Ω_p^{-1} (where Ω_p is the proton gyro frequency) respectively, and velocity is normalized to the simulation Alfvén speed $V_A = B_u/\sqrt{\mu_o n_p m_p}$ that does not change with He^{++} fraction. The proton density $n_p m_p$ and magnetic field B_u used to calculate these parameters are also normalized to the initial upstream values. The number of grid cells for all the runs is $n_x \times n_y = 1{,}000 \times 800$ having cell sizes $\Delta x = \Delta y = 0.5\ c/\omega_p$ with velocity, magnetic field, and electric field vectors including all three-dimensional components. The time step Δt was chosen so that $\Omega_p\, \Delta t = 0.005$. In all cases, the plasma is initialized with an inflow speed V_{in} of 3.3 V_A along the x direction and with the magnetic field in the x-y simulation plane.

The injection method has been used to create and sustain the shock transition. The plasma flows along the x direction at the (super-Alfvénic) speed V_{in}. The right boundary of the simulation acts as a perfectly reflecting wall, and plasma is continuously injected at the left (open) boundary. As a consequence of the interaction between the reflected and injected plasma, a shock is produced, and it propagates in the negative x direction. In the simulation frame, the downstream side of the shock is at rest, and the shock normal is antiparallel to the inflow speed. The simulation is periodic in the y direction.

We perform different runs varying the initial angle between the upstream B-field direction and the x-axis (15°, 30°, 50°, and 65°), which also corresponds to the nominal angle θ_{Bn} of the shocks. Alpha particles are included in the simulations self-consistently. For each θ_{Bn} value, we vary the relative number density fraction of He^{++}, that is, $n_\alpha/n_p = 0.01$, 0.05, 0.10, with n_α and n_p being the number density fraction of He^{++} and protons, respectively. We thus perform 12 simulation runs (see Figure 1).

A finite resistivity, $\eta = 0.06\ \omega_p^{-1}$, is used in the simulations with the upstream ion populations having an isotropic Maxwellian VDF, with an upstream $\beta = 0.5$. In order to keep the statistical noise typical of PIC simulations to a minimum, the number of particles per cell for all the simulations is ~ 100 per species

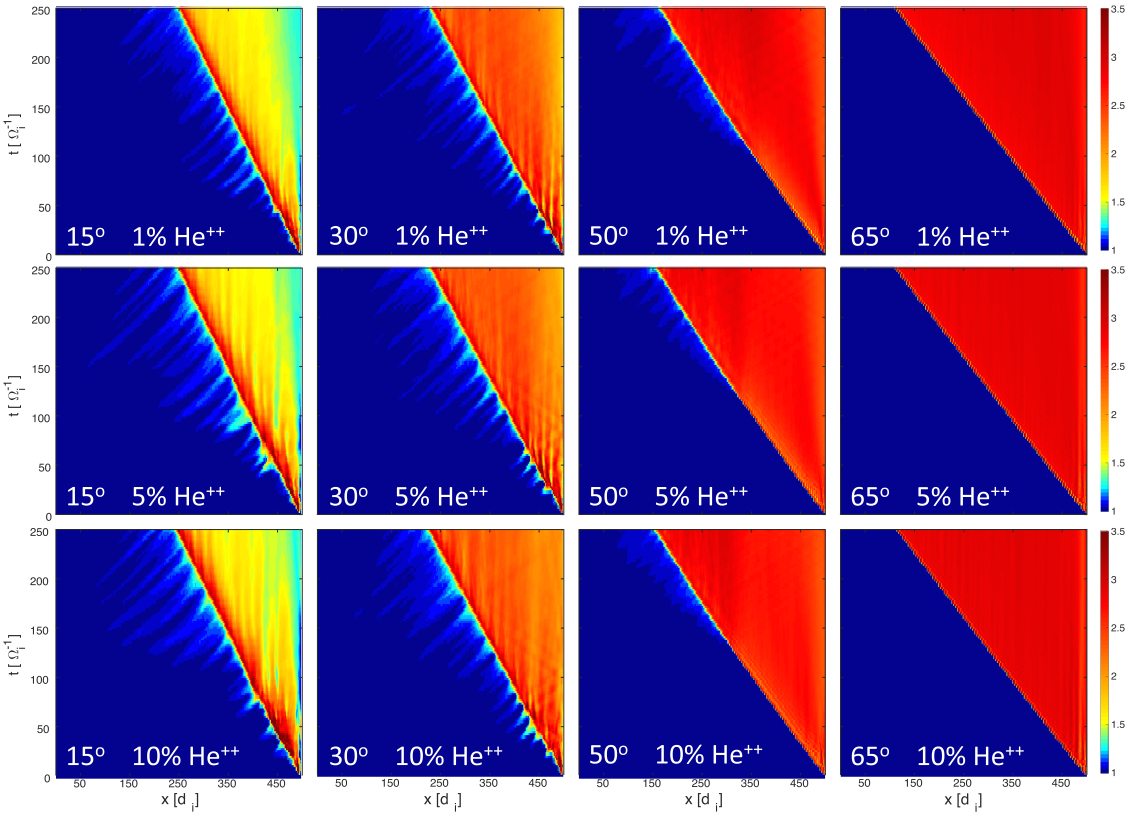

Figure 1. Figure matrix showing the time evolution of total magnetic field (averaged over y-axis) for all the runs in this work. θ_{Bn} increases from left to right while the He^{++} number density fraction increases from top to bottom. The change in color from navy to aqua occurs at ~1.25 while the change from green to yellow occurs at ~1.5.

(upstream). This is done to correctly model minor species, even if its fraction is small. It should be noted that the different values of θ_{Bn} for each simulation results in slightly different shocks velocities (Caprioli & Spitkovsky, 2014) in the simulation frame (and therefore slightly different M_A) depending on the θ_{Bn} value. We study the shocks once they have reached the same x position (i.e., $x \sim 250\ d_i$) in the middle of the box; hence, due to different shock velocities, the simulation times of the shocks will differ.

3. Simulation Results

3.1. Magnetic Field

Figure 1 shows the time evolution of the average magnetic field profile obtained by averaging in the y-direction. In the figure, the shock θ_{Bn} values increase from left to right from 15°, 30°, 50°, to 65°. The He^{++} number density fraction increases from 1% (top panel), 5% (middle) to 10% (bottom).

The color scale has the same range (from 1 to 3.5) in all plots. The shock can be identified by the abrupt jump in the magnetic field magnitude by a factor of $\gtrsim 2$, with the color changing from blue to red. Although the inflow velocity is the same for all the runs, due to the different θ_{Bn} values the shock velocity and thereby the Alfvénic Mach number vary, being higher as the θ_{Bn} increases: $M_A = 4.2, 4.3, 4.5, 4.8$ for $\theta_{Bn} = 15°$, 30°, 50°, and 65°, respectively. The He^{++} number density fraction does not seem to influence the Mach number in a significant manner.

Clear differences can be observed in the averaged magnetic field profile time evolution as θ_{Bn} increases. For the 15° case, the magnetic field magnitude exhibits maximum values $\lesssim 3$ in the downstream region (red color) within 25 d_i from shock transition. The width of this plateau tends to increase as the He^{++} number density fraction increases. Further downstream, the magnetic field magnitude decreases to ~ 1.5.

In the upstream region, the magnetic field fluctuations exhibit amplitudes up to 1.5 near the shock. These upstream fluctuations start to form at the beginning of the simulations very close to the shock, reaching larger distances from the shock as the simulation evolves.

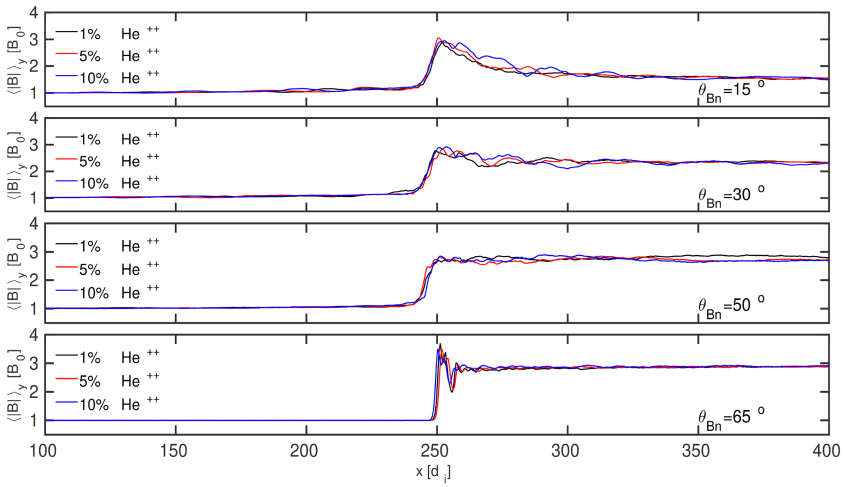

Figure 2. Total magnetic field profile (average over *y*-axis) for the all the different θ_{Bn} values used in this work when the shock arrives to $\sim 250\ d_i$. The θ_{Bn} angle increases from top to bottom, He^{++} number density fraction is indicated by different colors (black: 1%, red: 5%, blue: 10%).

Although not shown here (see Figure S1 in the Supporting Information), the plots of magnetic field magnitude for an horizontal cut in the simulation box at different consecutive times show different compressive waves and whistler wave packets formed upstream of the shock. These waves convect into the shock causing the shock transition to change from a gradual to an abrupt profile contributing to the reformation of the shock as suggested in past works (Burgess, 1989a; Hao et al., 2017). These waves have different characteristics depending on the content of He^{++} particles and will be studied in the future.

In the 30° case, the magnetic field magnitude reaches similar maximum values in the downstream region as in the 15° case (< 3), but B values do not decrease as much further downstream, settling at ~ 2. The upstream fluctuations tend to have smaller amplitudes than in the 15° case. They do however behave similarly in the sense that in the beginning they form close to the shock and extend to larger distances from it as the simulation evolves.

For the 50° geometry, the downstream B-field magnitude reaches values of $\lesssim 3$ and there is no clear decrease with distance from the shock in the downstream region. The compressive magnetic fluctuations in the upstream side exhibit considerably smaller amplitudes compared with the previous geometries and begin to appear later in the simulations, after $t \sim 100\ \Omega^{-1}$. Their upstream extensions are much smaller. These upstream increased B-field fluctuations appear later in time as the He^{++} number density fraction increases The onset times are approximately 100, 125, and 170 Ω_p^{-1} for 1%, 5%, and 10% of He^{++}, respectively. Downstream magnetic field fluctuations decrease their amplitude considerably compared with the less oblique cases and almost no differences are observed in the magnetic signature as the He^{++} percentage changes in the simulations (see also Figure 2).

For the 65° case, there are no compressive fluctuations in the upstream region. The shock transition is very abrupt and the B-field increases to values up to ~ 4. A very narrow overshoot is formed immediately behind the shock ramp (see Figure 2) and is followed by a fast decrease to a constant value of ~ 3. The downstream fluctuations for this case have amplitudes similar to those in the 50° case.

Figure 2 shows the average total magnetic field profiles for all the θ_{Bn} values at the time when the shock arrives to $\sim 250\ d_i$. This time has been chosen based on Figure 1 and corresponds to the time when the upstream waves have properly formed. The three profiles plotted in each panel correspond to different He^{++} number density fractions (black: 1%, red: 5%, blue: 10%).

Figure 2 exhibits clear variations of the averaged shock magnetic field profile. Well-developed compressive B-field variations in the upstream region can be identified decreasing in amplitude as θ_{Bn} increases except for the 65° geometry where they do not develop. These variations extend farther upstream for the 15° and 30° cases. The averaged shock front becomes steeper as the shock becomes more oblique. As the θ_{Bn} increases, the shock profile changes from a peak-like to a step-like signature. When $\theta_{Bn} = 65°$, a sharp overshoot forms

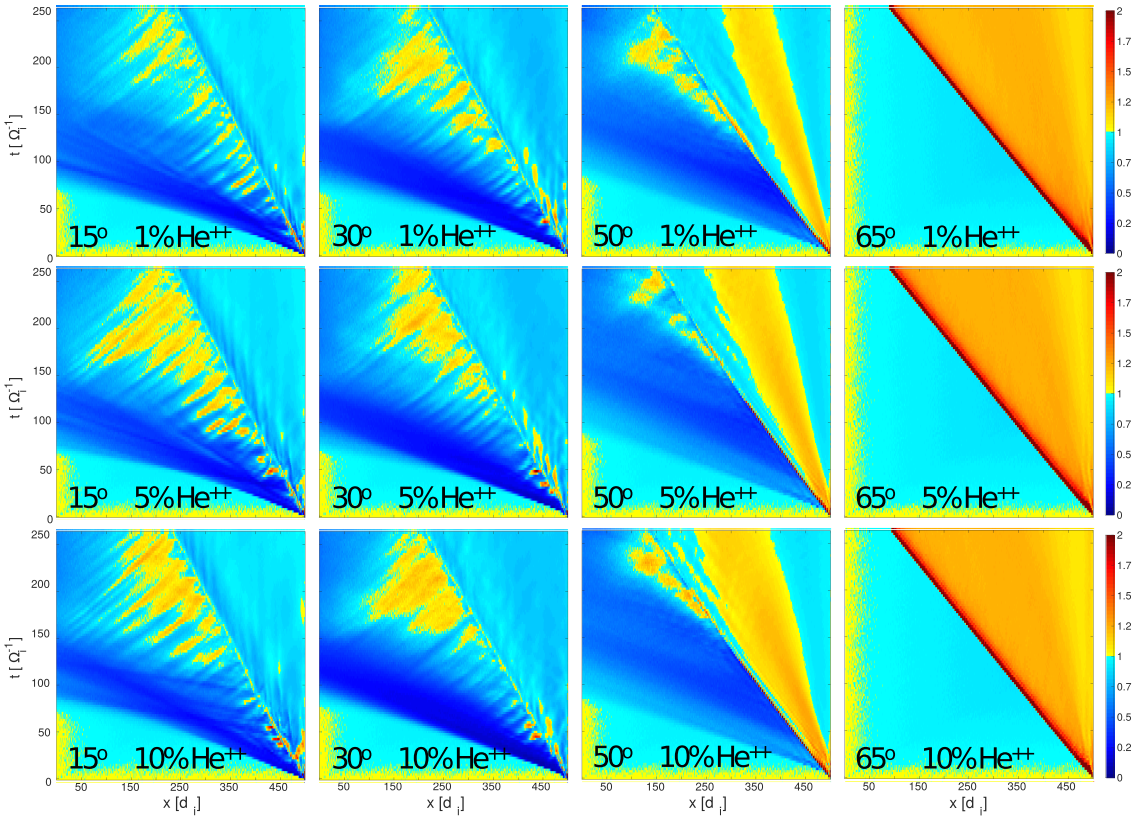

Figure 3. Figure matrix showing the time evolution of temperature anisotropy for protons (averaged over *y*-axis) for all the runs in this work. θ_{Bn} increases from left to right while the He^{++} number density fraction increases from top to bottom. The color palette is chosen to show anisotropy values less (in blue) and greater (in yellow-red) than 1.

just behind the shock followed by an undershoot. For the quasi-parallel cases ($\theta_{Bn} = 15°$ and 30°), the magnetic field fluctuations after the shock decrease more gradually as the content of He^{++} particles increases. The downstream fluctuations tend to have smaller amplitudes as the θ_{Bn} increases. For the more oblique case ($\theta_{Bn} = 65°$), downstream quasi-periodic fluctuations after the undershoot can be observed growing in amplitude as the content of He^{++} particles increases in agreement with a similar recent work (Ofman et al., 2019) where simulations of shocks with $\theta_{Bn} = 60°$ and different percentages of He^{++} are performed and compared with DSCOVR observations. After $\sim 350\ d_i$, the downstream compressive fluctuations have almost disappeared, regardless of the He^{++} content. The asymptotic downstream B value is larger as the shock geometry becomes more oblique going from a magnitude of 1.5 for $\theta_{Bn} = 15°$ to 3 for $\theta_{Bn} = 65°$ as expected from the fluid shock conservation (Rankie-Hugoniot) relations.

3.2. Temperature Anisotropy

Figure 3 shows the time evolution of proton temperature anisotropy $A_p = (T_\perp/T_\parallel)_p$ averaged over the *y*-axis for each of our simulations following the same procedure as in Figure 1. The parallel and perpendicular temperatures are calculated from the second velocity moment of the distribution function (see, e.g., Gary, 1993) in each cell. The color bar palette was divided in two colors: dark to aqua-blue color to represent the anisotropy values less than one and yellow to red color for anisotropy values from one to two. Figure 3 shows that there are three types of behavior for A_p, which are correlated with shock geometry as follows:

- In the case of quasi-parallel shocks with $\theta_{Bn} = 15°$ and 30°, the upstream region that is filled initially with an isotropic flux ($T_\parallel \sim T_\perp$) starts to be permeated by backstreaming particles coming from the shock leading to $T_\parallel > T_\perp$ as can be observed in dark blue color. As the simulation evolves and more backstreaming particles interact with the incoming plasma near the shock, upstream regions with $A_p > 1$ begin to develop as a consequence of fluctuations in magnetic field, which can be corroborated by examining Figure 1. For $\theta_{Bn} = 15°$, these upstream regions where $A_p > 1$ seem more fragmented, also their extension to the upstream side is smaller for the case with 1% of He^{++} in comparison with those with higher He^{++} number density

fraction. This behavior is also observed for the $\theta_{Bn} = 30°$ case being less fragmented in comparison to the less oblique case. The downstream region for both quasi-parallel cases has $A_p \sim 1$ throughout all the simulation, for the $\theta_{Bn} = 30°$ case. Small zones with $A_p > 1$ in the immediate downstream region can be observed at early times in the simulations, being less extended for the case with higher He^{++} number density fraction.

• In the case of the oblique shock with $\theta_{Bn} = 50°$, a well-defined region with $A_p > 1$ develops very early in the simulation just downstream of the shock, appearing closer to it, being larger in extension as the percentage of He^{++} particles increases. A narrow high anisotropy layer with $A_p \sim 2$ is located exactly at the shock transition reducing its magnitude before upstream regions near the shock with $A_p > 1$ start to appear extending more and more toward the upstream side as the simulation evolves. As for the quasi-parallel cases, the upstream region where the incident plasma flow initially has an isotropic distribution start to be permeated by zones with $T_{\parallel} > T_{\perp}$ (dark blue) due to backstreaming particles aligned to the magnetic field lines. As the simulation continues to evolve, upstream regions with $A_p > 1$ appear in the upstream region coinciding with zones with compressive magnetic field fluctuations as discussed in Figure 1. These upstream regions where $A_p > 1$ appear at earlier times ($t < 150 \quad \Omega_i^{-1}$) for the simulation with 1% of He^{++} particles in comparison with the 10% case ($t > 150 \quad \Omega_i^{-1}$). The upstream transition region from $T_{\parallel} \sim T_{\perp}$ to $T_{\parallel} > T_{\perp}$ is not as sharp as in the quasi parallel cases and the extent of this region lasts longer since the regions with $A_p > 1$ begin to develop at more advanced times for this geometry. Also the region with $T_{\parallel} > T_{\perp}$ appears in the upstream region later in time ($t > 100\ \Omega_i^{-1}$) in comparison with its quasi parallel counterpart ($t \sim 100\ \Omega_i^{-1}$), which is in agreement with the less efficient parallel transport of particles expected for this quasi-perpendicular geometry. In contrast to the other geometries, for this case, the different behavior in the immediate upstream side of the shock after $t \sim 150\ \Omega^{-1}$ when upstream B-field fluctuations starts to develop allowing the increase in temperature anisotropy that define a characteristic simulation time associated with growth and convection of upstream fluctuations that could not be observed if the simulation had not lasted so long. It must also be mentioned that the "wall effect" observed near the right wall is not physical but a falsely perceived effect due to the high contrast colors near $A_p \sim 1$.

• In the case of the shock with $\theta_{Bn} = 65°$, the value of A_p is greater than one through all the downstream region reaching the maximum value (> 8) in the region adjacent to the shock transition during the whole time of the simulation. The proton anisotropy value is ~ 1 throughout all the upstream region in agreement with the fact that the rate of backstreaming particles is almost null for this high θ_{Bn} case and no upstream magnetic field fluctuations are present in Figure 1.

Figure 4 shows semi-log plots of $T_{\perp}/T_{\parallel}$ (averaged over *y*-axis) for protons (blue) and He^{++} (orange) at the time when the shocks arrive to ~ 250 d_i. The shock position is marked with a vertical dashed line while the horizontal dashed line indicates $T_{\perp}/T_{\parallel} = 1$. For clarity only a range from 100 d_i to 300 d_i in the x-axis and from 0.5 to 5 (with minor ticks spaced each 0.25) in the *y*-axis are plotted. As before, the temperature anisotropy profiles show three distinct behaviors:

• Quasi parallel cases ($\theta_{Bn} = 15°, 30°$): For both geometries, the upstream value of $A_p \sim 0.75$ at $x = 100\, d_i$ increases to values $\gtrsim 1$ in some *x*-intervals near the shock region that are more extended and reach higher values as the He^{++} number density fraction increases. In general, A_p is greater than the He^{++} temperature anisotropy $A_\alpha = (T_{\perp}/T_{\parallel})_\alpha$ in the upstream region. In the downstream region, A_p exhibits a decrement to values less than 1 while A_α rises sharply reaching a maximum peak value (~ 1.5 for 15° and ~ 1.75 for 30°) at the shock transition to then decrease to ~ 1. For the case with $\theta_{Bn} = 30°$, the A_α peak at the shock transition tends to be wider as the He^{++} percentages increase.

• Oblique case ($\theta_{Bn} = 50°$): In contrast to the quasi parallel geometries, here A_p at x =100 d_i becomes increasingly smaller as the He^{++} content grows. *x*-intervals with $A_p > 1$ that are less extended and reach lower values as the He^{++} number density fraction increases can be observed. Then A_p drops significantly in the upstream region adjacent to the shock. This drop is less pronounced in the case of the 10% He^{++} run. Unlike for the quasi parallel cases, for this geometry, $A_p < A_\alpha$ along all the upstream side except for the 1% He^{++} case where a region with $A_p \sim A_\alpha$ at about $x \sim 200\, d_i$ can be observed. Downstream of the shock A_p decreases to values less than one. The value of A_α rise sharply reaching a peak at the shock transition that increases in value (2.75, 3.75, 4.25) as the He^{++} percentage does and then drops in the downstream region. This fall becomes more abrupt, making the width of the peak thinner as the content of He^{++} particles increases.

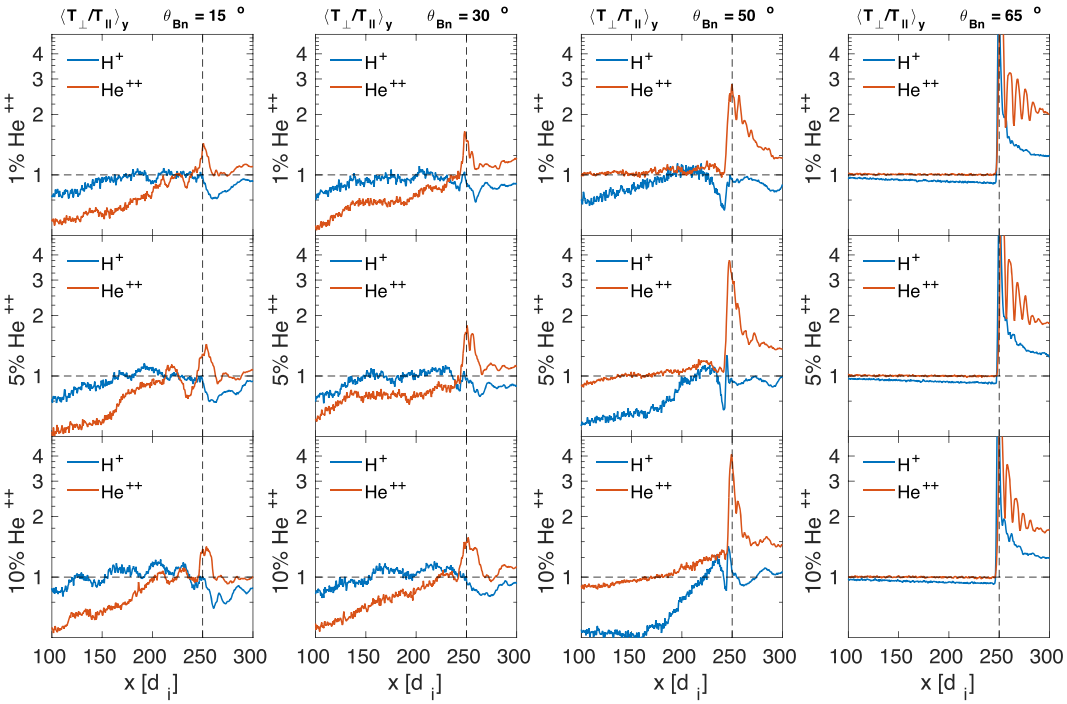

Figure 4. Semi-log temperature anisotropy profiles (average over y-axis) for protons (blue) and He^{++} (orange) at the time when the shock arrives to $\sim 250\, d_i$ for all the θ_{Bn} values and He^{++} percentages in this work. The vertical dashed line indicates the shock localization and the horizontal dashed line indicates $T_\perp/T_\parallel = 1$

• Quasi-perpendicular geometry ($\theta_{Bn} = 65°$): Here, the value of A_α is 1 throughout all the upstream region, then rises sharply at the shock transition reaching smaller peak values (8.2, 7.8, 7.5) as the He^{++} number density fraction increases, and then decreasing in the downstream region. This drop is not monotonic since downstream oscillations of A_α can be observed as a consequence of the coherent gyration of He^{++} particles as pointed in previous works (Hao et al., 2014; McKean et al., 1996) and discussed here in section 3.3. For protons, the upstream values of A_p are just below 1, then increase substantially at the shock transition to values that are, in contrast to A_α, greater (8.8, 8.9, 9.31) as the He^{++} content increases. Then A_α drop to $\sim$ 1.25 in the downstream region. The decrease here does not show downstream oscillations, which can be explained in terms of the differences in charge to mass ratios for both species.

Additionally, we performed an extra simulation (not shown) with $\theta_{Bn} = 75°$ in order to see if there are differences comparing with the $\theta_{Bn} = 65°$ case. We did not find significant changes beyond the expected increment in the downstream overshoot magnitude.

3.3. Velocity Distribution Functions

We also investigate the behavior of the velocity distribution functions (VDFs) for both ion species in the shock interface zone along the shock surface as well as at different x coordinates for the time when the shock is at $x = 250 d_i$. We show four cases corresponding to $\theta_{Bn} = 15°$, 65° with 1% and 10% of He^{++} since they exemplify the main VDF characteristics due to variations in the angle θ_{Bn} from quasi-parallel to quasi-perpendicular and the low and high number density fraction in He^{++} particles. It is important to mention that the number density of points in VDFs depends on the number of particles per cell so that the relative fraction of He^{++} to protons is not seen when comparing VDFs for the two species.

Figure 5 displays the cases for $\theta_{Bn} = 15°$ with 1% and 10% of He^{++}. By comparing Figures 5a and 5c, we can observe that the downstream region exhibits higher amplitude magnetic fluctuations reaching values (> 3) along a larger range of x in the case of the shock with 10% of He^{++}. In Figures 5b and 5d, where cuts along $y = 100\, d_i$ (red) and $y = 250\, d_i$ (blue) are shown, variations in downstream magnetic field are clearly observed. In addition, for the 10% case, the variations between both cuts along y-direction are more pronounced compared to the case with lower He^{++} number density fraction. Upstream of the shock whistler

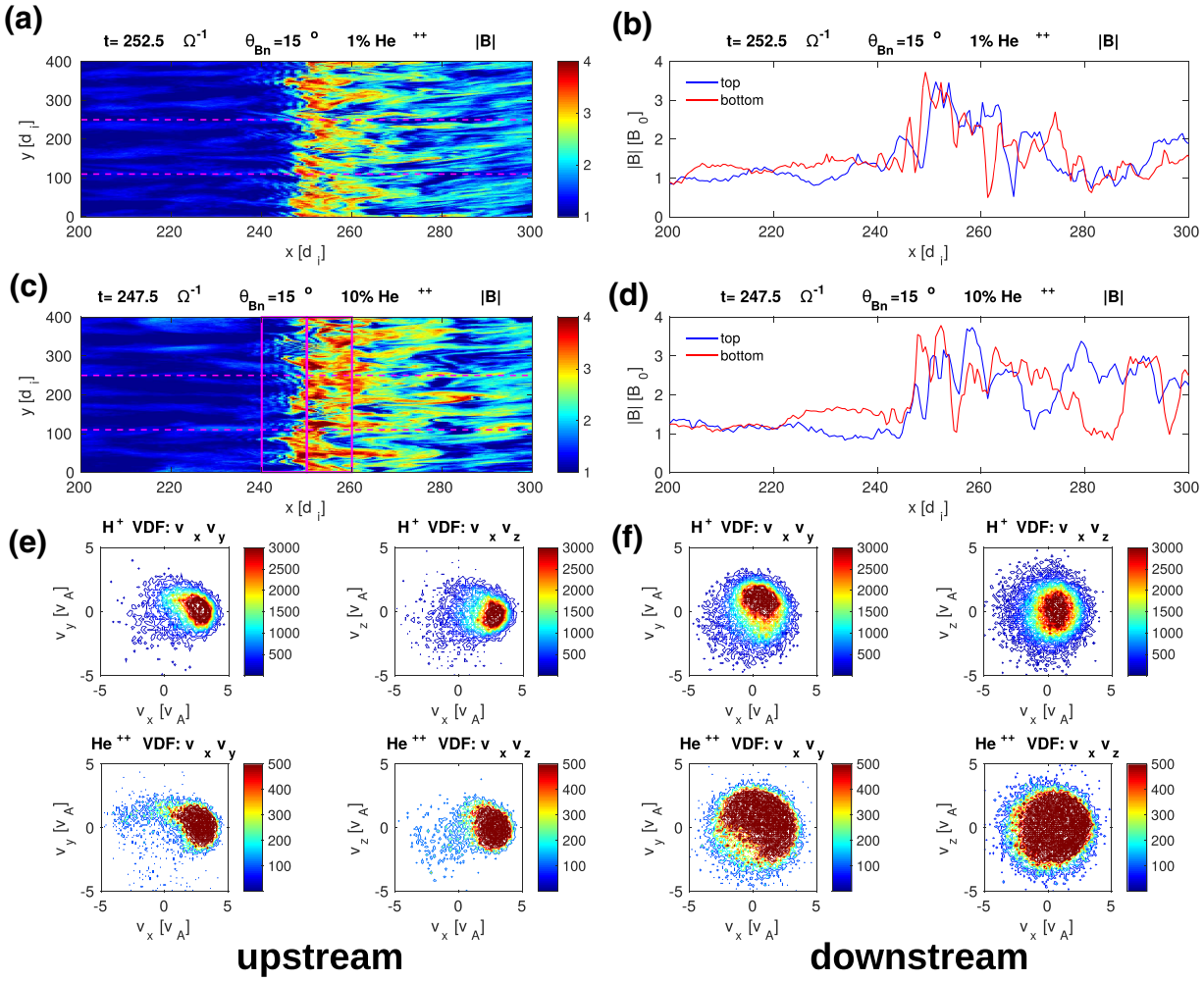

Figure 5. Plots corresponding to the simulation with $\theta_{Bn} = 15°$ at the time when the shock arrives to $x = 250\, d_i$: Contour plot of total magnetic field (a) and magnetic field (b) along two horizontal cuts at the upper (blue line) and lower (red line) dashed lines in panel (a) for the case with 1% of He^{++} particles. Panels (c) and (d) show the same results for the case with 10% of He^{++} particles. The VDF's for both species for the case with 10% of He^{++} particles contained inside the left (upstream side) magenta box on panel (c) are shown in panels (e). The same results for the right (downstream side) magenta box on panel (c) are shown in panels (f). The color bar in VDF's indicates the particle counts.

precursors are observed in both He^{++} cases for the bottom cut (in red) due to the irregular shock front profile. Whistlers are not found in the top cut (in blue).

Figures 5e and 5f show the upstream and downstream VDFs, respectively, for both species in the regions inside the magenta boxes in Figure 5c corresponding to the case with 10% of He^{++} particles. The proton VDF in the upstream region (V_x–V_y space) has two principal components (Figure 5e): A main beam centered at (V_x, V_y, V_z) = (3.3, 0, 0) V_A corresponding to the inflow particles and a secondary component of backstreaming particles ($V_x < 3.3$). Comparing the upstream VDFs of both species, we notice that the secondary component of the VDF corresponding to protons is more populated and reaches higher values in velocity than its He^{++} counterpart.

Although they are qualitatively similar, the differences between VDFs at different vertical locations in the upstream side (not showed) can be attributed to the deformation of the shock front, which produces different local geometry (Figures 5a and 5c) that leads to different plasma processing along the shock and inside the collecting boxes as can be corroborated by observing the differences in magnetic profiles in Figures 5b and 5d for regions on both sides of the shock.

For the downstream side (Figure 5f), the thermalization of particles through the shock potential produces a spread of the VDF for both species in all directions. Again, the VDF in V_x-V_y space tends to be more isotropic

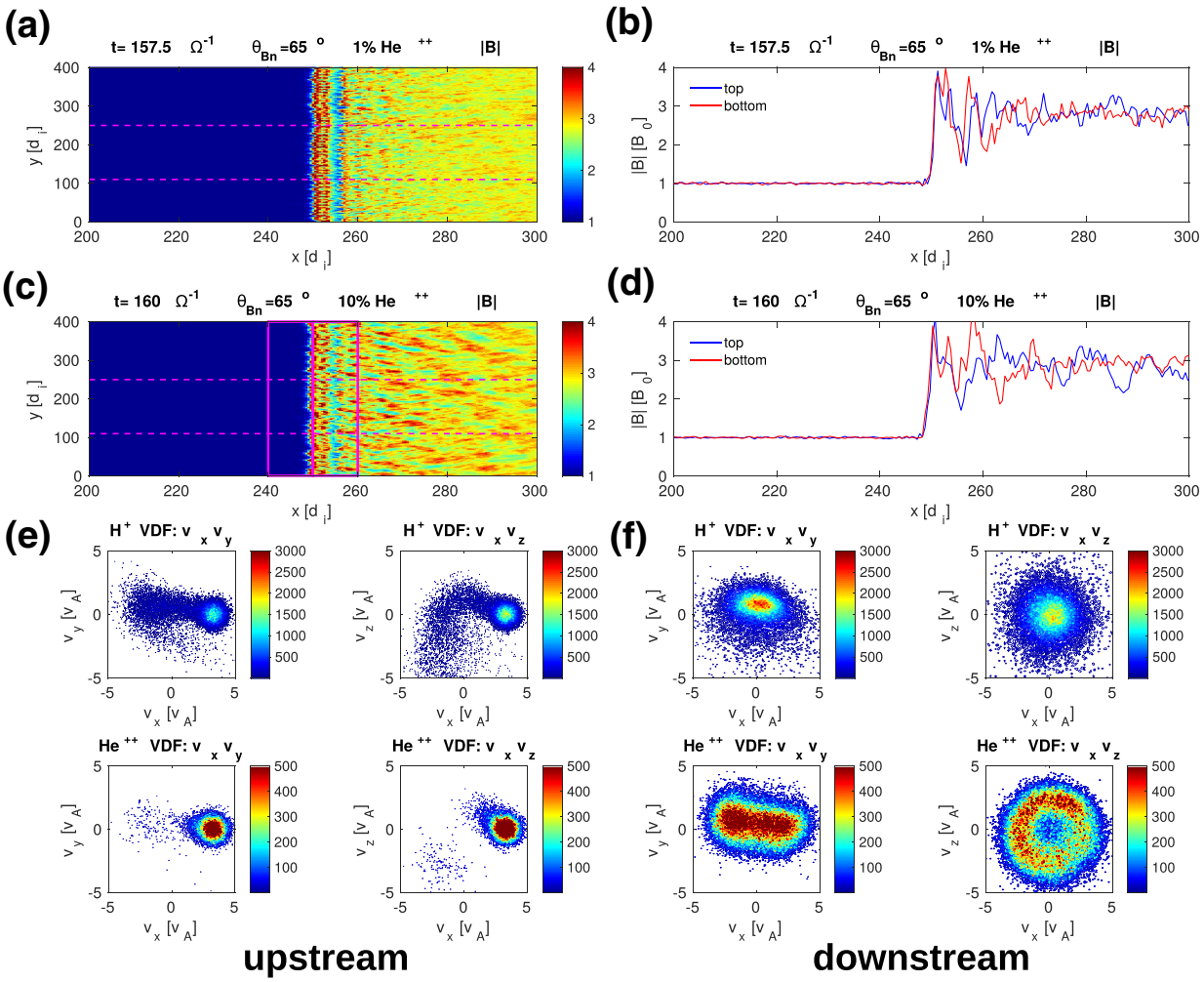

Figure 6. Plots corresponding to the simulation with $\theta_{Bn} = 65°$ at the time when the shock arrives to $x = 250\, d_i$: Contour plot of total magnetic field (a) and magnetic field (b) along two horizontal cuts at the upper (blue line) and lower (red line) dashed lines in panel (a) for the case with 1% of He^{++} particles. Panels (c) and (d) show the same results for the case with 10% of He^{++} particles. The VDF's for both species for the case with 10% of He^{++} particles contained inside the left (upstream side) magenta box on panel (c) are shown in panels (e). The same results for the right (downstream side) magenta box on panel (c) are shown in panels (f). The color bar in VDF's indicates the particle counts.

$(T_\perp/T_\parallel \sim 1)$ for protons than for alphas (Figure 5f), which is in agreement with Figure 4. As for the upstream side, there are differences in the VDF's at different y-coordinates in the downstream side but they are not so pronounced, and this can be explained in terms of the differences in the turbulent magnetosheath region as can be observed for both profiles in magnetic field in Figure 5d.

Figure 6 shows the $\theta_{Bn} = 65°$ simulation with 1% and 10% of He^{++} particles in the same format as Figure 5. As in the previous case, Figures 6a and 6c show that the downstream region is permeated by larger amplitude field fluctuations when the number density fraction of He^{++} is higher. This behavior is corroborated comparing Figures 6b and 6d where the profiles show more turbulence in magnetic field for the case with 10% of He^{++}. Also, the differences in magnetic field profiles are more pronounced for the case with the highest percentage of helium He^{++}. For the upstream side, no differences between cases with different He^{++} percentage are found for the magnetic field. In contrast to the quasi parallel cases, here the shock transition is sharp and presents a clear overshoot.

Figure 6e for the $\theta_{Bn} = 65°$ shows clearly less particles for both species in the upstream side in comparison with the $\theta_{Bn} = 15°$ case in Figure 5. The VDF only shows some of the reflected-gyrating ions that will eventually end up in the downstream region. In addition, for this case, very few backstreaming He^{++} particles can be observed when comparing with protons (lower panels in 6e). This can be explained by the differences of

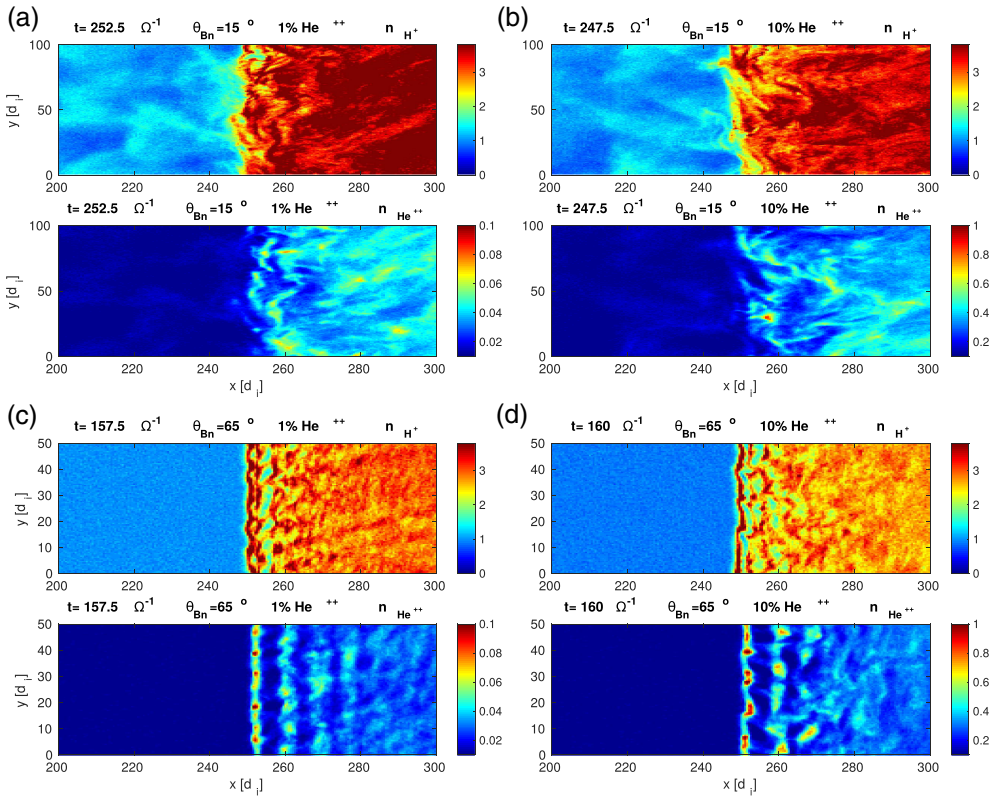

Figure 7. Contour plots of protons and He^{++} densities corresponding to the simulations with $\theta_{Bn} = 15°$ for 1% (a) and 10% (b) of He^{++} particles and with $\theta_{Bn} = 65°$ for 1% (c) and 10% (d) of He^{++}. The time of the plots correspond to those magnetic field magnitude plots in Figures 5 and 6.

mass for both species that facilitates protons to be more efficiently reflected to the upstream side than their He^{++} counterpart as reported in previous simulation works (see, e.g., Burgess, 1989b) and in agreement with Broll et al. (2018), where data and hybrid simulations of a bow shock observed by the Magnetospheric Multiscale (MMS) mission indicate that the amount of He^{++} that reflects at the shock is smaller than the proton population.

Figure 6f shows different behaviors for proton and He^{++} particles in the downstream region. He^{++} particles tend to form a ring-like distribution centered in $(V_x, V_z) = (0, 0)$ in agreement with previous works such as Hao et al. (2014), who explained this ring as a consequence of differentially deceleration of He^{++} particles compared to protons due to their different charge-to-mass ratio as they cross the shock potential. On V_x–V_y panels in Figure 6f, it is possible to see that both species differ mainly in the width of their distributions functions along V_x as expected from the results from Figure 4, where the anisotropy value has a broader and higher peak in the immediate downstream region for He^{++} particles than for protons. Because of the quasi-perpendicular geometry for this case, there are no pronounced irregularities along the shock front as can be observed in Figures 6b and 6d in contrast with the $\theta_{Bn} = 15°$ case (panels b and d in Figure 5). Although not showed here (see Figure S2 in the Supporting Information) when compared VDFs between different He^{++} percentages for this quasi-perpendicular case, it can be observed that the downstream VDFs for both species tend to be more diffuse for the case with higher He^{++} percentage; this can be explained as a consequence of the more perturbed magnetic field on the downstream side of the shock as the He^{++} number density fraction increases as can be observed from the differences between horizontal cuts for both He^{++} cases here (Figures 6b and 6d).

The characteristics of VDFs found here are in agreement with previous works (Motschmann & Glassmeier, 1993), that is, whereas in quasi-parallel configurations the scattering of protons in V_x–V_y space is rather isotropic (Figure 5f), in the quasi-perpendicular case, it remains anisotropic (Figure 6f). In the last case, the

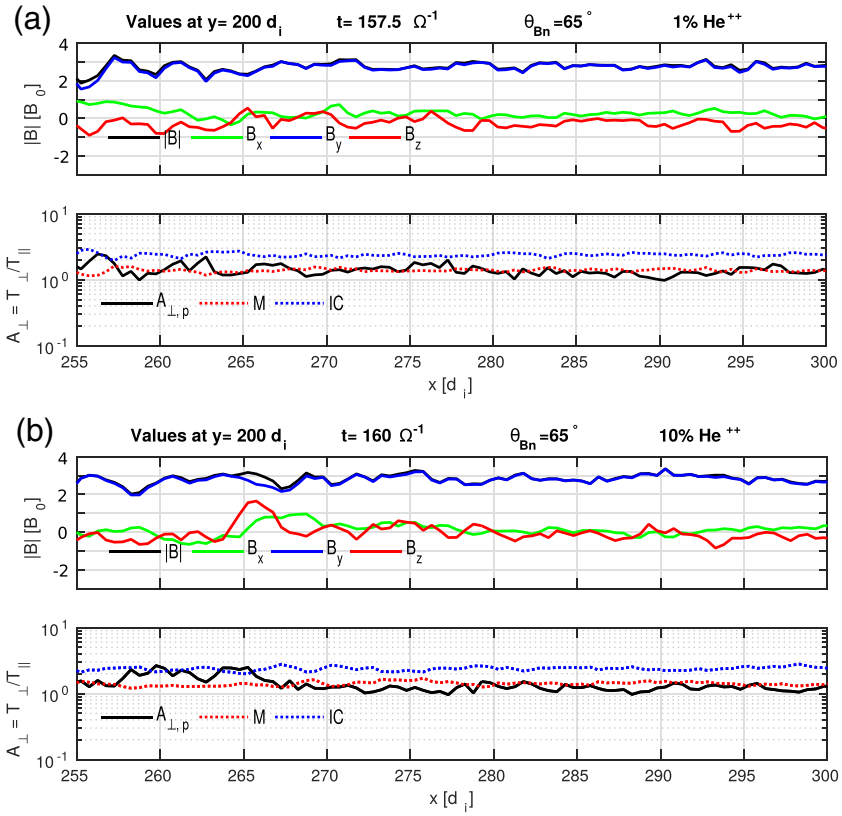

Figure 8. Magnetic field and proton temperature anisotropy ($T_\perp/T_\parallel$) cuts along downstream region at $y = 200\ d_i$ corresponding to simulations with $\theta_{Bn} = 65°$ for 1% (a) and 10% (b) of He^{++}. Temperature anisotropy as well as the parameters ($M = 1 + 1/\beta_\perp$) in red and ($IC = 1 + \beta_\parallel^{0.5}$) in blue are shown in the same panels. The condition for the growing of the mirror instability is fulfilled by the threshold $T_\perp/T_\parallel > M$, the corresponding condition for ion/cyclotron instability is $T_\perp/T_\parallel < IC$. The time of the plots correspond to those in Figure 7.

He^{++} distribution in V_x–V_z space is a ring around the magnetic field vector mainly pointed in y direction (Figure 6f).

Figure 7 shows the densities of protons and He^{++} particles corresponding to the same simulations and times as in Figures 5 and 6. Clear differences can be observed when comparing both geometries. While for the quasi-parallel case (panels a and b) the shock interface is not well defined and presents the typical rippling as well as not coherent fluctuations at both sides of the shock, for the quasi-perpendicular shock (panels c and d), the shock interface is well defined, no upstream density structures can be observed, and a wave-like structure is evident behind the shock decreasing in amplitude further in the downstream region. When we analyze the differences for the same geometries taking in account the He^{++} content in the simulations, the effect is more evident for the quasi-perpendicular case (panels c and d) where the fluctuations are more defined but with lower amplitudes for the cases with less He^{++} content. This feature is correlated with both the temperature anisotropy and the magnetic field magnitude in the same regions as can be corroborated in Figures 4, 5, and 6. This is in agreement with (Ofman et al., 2019), who explained this behavior in terms of the He^{++} "surfing" (Lee et al., 1996) along the shock front evidenced by the strong localized density peaks.

3.4. Mirror and Ion/Cyclotron Instability Analysis

In this section, we study the growing of mirror and ion/cyclotron waves (Gary, 1993) using instability thresholds related with temperature anisotropy and plasma beta parameters in order to know when these modes can grow. This analysis is valid for cases where the condition $T_\perp/T_\parallel > 1$ is well fulfilled for protons (Gary,1993; McKean et al., 1995a, 1995b), namely, in the downstream region for our $\theta_{Bn} = 65°$ cases as can be corroborated in Figures 4 and 6f where the downstream VDFs are shown. For this purpose, in Figure 8, some cuts of proton anisotropy ($T_\perp/T_\parallel$) and magnetic field at $y = 200\ d_i$ and just behind the shock corresponding to the same simulation times of those in Figures 7c and 7d are shown. In addition to $T_\perp/T_\parallel$, the

parameters $M = 1 + 1/\beta_{\perp}$ (in red) and $IC = 1 + \beta_{\parallel}^{0.5}$ (in blue) are shown in the same panel. From these, it follows that the growing threshold of mirror instability is fulfilled when $T_{\perp}/T_{\parallel} > M$ (Southwood & Kivelson, 1993) while the corresponding condition for the ion/cyclotron instability approximate threshold is $T_{\perp}/T_{\parallel} <$ IC (Anderson et al., 1996; Gary et al., 1996). As can be observed in Figure 8 for both He^{++} concentrations simulations, the ion/cyclotron threshold is fulfilled along the cut. For the mirror instability, the threshold is barely fulfilled only at some located intervals near the shock interface. These results are in agreement with Hao et al. (2014) and McKean et al. (1995a, 1995b), who studied with hybrid simulation quasi-perpendicular shocks with similar parameters finding that ion/cyclotron waves can grow in the downstream region by the energy provided by the ion temperature anisotropy. Not many differences are observed when comparing the results for both He^{++} relative abundances except for an increase in the size of the regions where the mirror instability threshold is met for the 10% He^{++} case, which leads to a reduction in the size of regions near the shock where the ion/cyclotron threshold is fulfilled. These results could be improved with a full kinetic instability calculation in a future work.

4. Discussion and Conclusions

Although the dependence of shock dynamics, temperature anisotropy, and VDF evolution with shock geometry (θ_{Bn}) has been widely studied in the past with the help of both observations and computer simulations, the influence of He^{++} number density fraction on interplanetary shock environments has received less attention. In order to study this influence, we have analyzed the results of twelve 2D local hybrid simulations of quasi-parallel ($\theta_{Bn} = 15°, 30°$) and quasi-perpendicular ($\theta_{Bn} = 50°, 65°$) collisionless shocks varying the number density fraction of He^{++} particles (1%, 5%, 10%). Our study shows that both the geometry and the content of He^{++} particles can modify the interplanetary shock profile and the characteristics of the upstream and downstream regions affecting temperature anisotropy, VDF properties, and magnetic fluctuations growth.

The variation of initial θ_{Bn} changes the efficiency with which particles can escape to the upstream side of the shock influencing the formation of compressive structures in the magnetic field profile. Quasi-parallel geometries ($\theta_{Bn} = 15°, 30°$) allow particles to be transported efficiently farther in the upstream region along the magnetic field lines. The interaction between these backstreaming particles and the incoming plasma flow results in upstream magnetic field fluctuations. The upstream variations of the averaged B-field profiles tend to have larger amplitudes and extend further to the upstream region for the 15° case. The shock with oblique geometry ($\theta_{Bn} = 50°$) takes more time to develop these fluctuations, and these reach lower amplitudes and extend less toward the upstream region compared with quasi-parallel cases. For the quasi-perpendicular shock ($\theta_{Bn} = 65°$), no upstream magnetic field fluctuations form. In the downstream region, such fluctuations tend to decrease in amplitude and length as the θ_{Bn} increase.

The magnetic field profile is also affected by shock geometry. The expected increment of magnetic field in the shock interface tends to be more abrupt as the θ_{Bn} increases. For the quasi-parallel geometries ($\theta_{Bn} = 15°$, 30°), the magnetic field magnitude decreases in the downstream side from the shock jump, this decrement is more gradual for the $\theta_{Bn} = 30°$ case. In contrast, for the oblique geometry ($\theta_{Bn} = 50°$), the magnetic field profile has a step-like shape. For the quasi-perpendicular geometry ($\theta_{Bn} = 65°$), the same step-like profile is observed with a clear overshoot just after the shock jump followed by a decrement in magnetic field to an almost constant downstream side value.

The temperature anisotropy for protons (A_p) is also affected by θ_{Bn}. For the quasi-parallel cases ($\theta_{Bn} = 15°$ and 30°), the upstream side starts to be permeated by backstreaming particles since the beginning of the simulation, which produce regions with $T_{\parallel} > T_{\perp}$. As the simulation evolves and backstreaming particles interact with the incoming plasma, upstream regions with $A_p > 1$ start to appear due to the fluctuations in magnetic field, which can heat and scatter the particles in the perpendicular direction to the magnetic field. For the oblique case ($\theta_{Bn} = 50°$), the upstream zones where $A_p > 1$ are less extended and appear later in time in comparison to the quasi-parallel cases, which is due to the fact that backstreaming particles are less efficiently transported to the upstream region far from the shock as the geometry becomes more oblique. In the quasi-perpendicular shock with $\theta_{Bn} = 65°$, there are no zones where $A_p > 1$ in the upstream side, which can be explained in terms of the so oblique geometry that does not allow particles to escape beyond the foot-ramp region. In the downstream region, $A_p \sim 1$ for the quasi-parallel cases ($\theta_{Bn} = 15°$ and 30°), for the oblique geometry ($\theta_{Bn} = 50°$), a zone with $A_p > 1$ appears, with a size that growths as the simulation evolves. For the quasi-perpendicular shock with $\theta_{Bn} = 65°$, the perpendicular temperature

presents a sudden increase in the shock transition due to the gyration of reflected particles that are convected into the downstream region increasing its perpendicular velocity. Then they suffer a rapid isotropization in the region downstream of the overshoot that are associated with the fluctuations present in the downstream region. These then diminish in amplitude with increasing distance downstream of the shock as has been observationally reported by (Sckopke et al., 1990).

The temperature anisotropy for both species (A_p, A_α) also shows a dependency on θ_{Bn}. For the quasi-parallel cases ($\theta_{Bn} = 15°$ and 30°), $A_\alpha < A_p$ in the upstream region and $A_\alpha > A_p$ in the downstream region. For the oblique geometry ($\theta_{Bn} = 50°$), $A_\alpha > A_p$ in general along all the simulation box. In the quasi-perpendicular shock ($\theta_{Bn} = 65°$), $A_\alpha \sim A_p \sim 1$ in the upstream region and then increase suddenly at the shock, decreasing in the downstream region with $A_\alpha > A_p$ and a fluctuating pattern for the He^{++} component. For all the geometries, a peak ($A_\alpha > 1$) is formed at shock transition that tends to be larger as the value of θ_{Bn} increases.

The VDFs for both species are also affected by θ_{Bn}. For the $\theta_{Bn} = 15°$ case, backstreaming particles of both species can be observed in the immediate upstream region in contrast to the quasi-perpendicular case ($\theta_{Bn} = 65°$) where the percentage of particles that do not belong to the inflow beam is much smaller. In contrast to the proton distributions, a ring-like distribution is formed in the immediate downstream side for He^{++} particles as a consequence of differential acceleration due to the different charge to mass ratio of both species. Also, the downstream VDFs for protons are more isotropic and thermalized for the $\theta_{Bn} = 15°$ case than for the $\theta_{Bn} = 65°$ case.

We find that the content of He^{++} also slightly affects the magnetic field structure at both sides of the shock. In quasi-parallel shocks ($\theta_{Bn} = 15°, 30°$), the compressive magnetic fluctuations on both sides of the shock tend to reach higher amplitudes for the cases with more He^{++} content. In contrast, for the shock with $\theta_{Bn} = 50°$, the increment in He^{++} number density fraction does not seem to affect the amplitude of these fluctuations. Although for the quasi-perpendicular case with $\theta_{Bn} = 65°$ no upstream compressive fluctuations are observed, in the downstream side, these fluctuations tend to reach larger amplitudes for the cases with more He^{++} content due to the increase of the temperature anisotropy in the immediate downstream region as the percentage of He^{++} particles increases (as will be discussed below).

The temperature anisotropy for protons (A_p) is also affected by the He^{++} content: The upstream zones where $A_p > 1$ coincide with those where compressive magnetic fluctuations are present as expected because fluctuations in magnetic field can produce heating and scattering of particles in the perpendicular direction relative to the magnetic field. For the quasi-parallel cases ($\theta_{Bn} = 15°$ and 30°), the upstream zones where $A_p > 1$ are less fragmented for the simulations where the number density fraction of He^{++} is higher. For the oblique case ($\theta_{Bn} = 50°$), this behavior is repeated while for the downstream region the zone with $A_p > 1$ is closer to the shock zone for the case where the He^{++} number density fraction is larger. When comparing the temperature anisotropy for both species (A_p, A_α), we can observe that although the content of He^{++} particles does not affect significantly the shape of the peak at the shock transition for the quasi-parallel cases, for the oblique case ($\theta_{Bn} = 50°$), a clear increment is observed as the number density fraction of He^{++} increases, and for the quasi-perpendicular simulations ($\theta_{Bn} = 65°$), the opposite happens: The peak decreases as the number density fraction of He^{++} increases.

The fact that for all our simulations, except in the more oblique case ($\theta_{Bn} = 65°$), upstream zones where $T_\perp > T_\parallel$ coincide with those where compressive magnetic field fluctuations are present is in agreement with recent results of Gingell (2017), where MMS observations show $T_\perp > T_\parallel$ in the upstream side of a marginally quasi-parallel bow shock ($\theta_{Bn} \sim 45°$) in regions where compressive fluctuations in the magnetic field occur.

The percentage of He^{++} particles also affects the VDF distributions, making them more spread as the percentage of He^{++} increases in both quasi-parallel and quasi-perpendicular cases. This is a consequence of the enhanced fluctuations in magnetic field, which occur when the He^{++} content is higher.

Finally, the results obtained in this work are relevant for the study of IP shocks driven by coronal mass ejections in the context of Parker Solar Probe and Solar Orbiter missions, which will collect data with high resolution at different helio-distances close to the Sun. This will allow us to directly compare our simulation models with observations for shocks at different stages of evolution. Future work include an in-depth analysis on the evolution of waves and kinetic instabilities at and near the shock for both quasi-parallel and quasi-perpendicular cases, shock reformation, and physical mechanisms concerning particle reflection and heating as well as VDF behavior through the upstream region to determine the helium foreshock extension.

Acknowledgments
We thank Dirección General de Cómputo y de Tecnologías de Información y Comunicación (DGTIC) of the Universidad Nacional Autónoma de México (UNAM) for the allocation and support received in the use of the HP Cluster Platform 3000SL supercomputer (MIZTLI). Contract grant sponsor: DGTIC-UNAM resources (project LANCAD-UNAM-DGTIC-337). The authors acknowledge support from the Royal Society Newton International Exchange Scheme (Mexico) grant NI150051. L.P. thanks CONACYT becas nacionales 2015–2019 grant 174700. X. B. C. is supported by CONACyT grant (255203) and DGAPA project (IN105218-3). D. B. was supported by the UK Science and Technology Facilities Council (STFC) grant ST/P000622/1. D.T. acknowledges support of a studentship funded by the Perren Fund of the University of London. P.K. is supported by PAPIIT grant (IA101118). Simulation data used in this research are publicly available online (https://doi.org/10.5281/zenodo.3697360).

References

Aguilar-Rodriguez, E., Blanco-Cano, X., Russell, C. T., Luhmann, J. G., Jian, L. K., & Ramirez Velez, J. C. (2011). Dual observations of interplanetary shocks associated with stream interaction regions. *Journal Geophysical Research*, *116*, A12109. https://doi.org/10.1029/2011JA016559

Anderson, B. J., Denton, R. E., Ho, G., Hamilton, D. C., Fuselier, S. A., & Strangeway, R. J. (1996). Observational test of local proton cyclotron instability in the Earth's magnetosphere. *Journal Geophysical Research*, *101*, 21,527.

Anderson, B. J., & Fuselier, S. A. (1993). Magnetic pulsations from 0.1 to 4.0 Hz and associated plasma properties in the Earth's subsolardepletion magnetosheath and plasma depletion layer. *Journal Geophysical Research*, *98*, 1461–1479. https://doi.org/10.1029/92JA02197

Blanco-Cano, X. (2016). Interplanetary shocks and foreshocks observed by STEREO during 2007-2010. *Journal of Geophysical Research: Space Physics*, *121*, 992–1008. https://doi.org/10.1002/2015JA021645

Blandford, R. D., & Ostriker, J. P. (1978). Particle Acceleration by astrophysical shocks. *Journal Astrophysical Part 2 - Letters to the Editor April 221*, *1*, L29–L32.

Broll, J. M., Fuselier, S. A., Trattner, K. J., Schwartz, S. J., Burch, J. L., Giles, B. L., & Anderson, B. J. (2018). MMS Observation of shock-reflected He^{++} at Earth's quasi-perpendicular bow shock. *Geophysical Research Letter*, *45*, 49–55. https://doi.org/10.1002/2017GL075411

Burgess, D. (1987). Numerical simulation of collisionless shocks. In K. Szego (Ed.), *Inproceedings of International Conference on Collisionless Shocks, Balatonfured, Hungary* (pp. 89–111). Budapest: Central Research Institute for Physics of Hungarian Academy of Sciences.

Burgess, D. (1987a). Shock drift acceleration at low energies. *Journal of Geophysical Research*, *92*(Feb. 1, 1987), 1119–1130.

Burgess, D (1989a). Cyclical behavior at quasi-parallel collisionless shocks. *Geophysical Research Letter*, *16*, 345–349.

Burgess, D (1989b). Alpha particles in field-aligned beams upstream of the bow shock: Simulations. *Geophysical Research Letter*, *16*, 163–166.

Burgess, D. (2005). Quasi-parallel shock structure and processes. *Space Science Review*, *118*, 205–222.

Burgess, D., & Scholer M. (2015). *Collisionless shocks in space plasmas, by David Burgess, Manfred Scholer*. Cambridge, UK: Cambridge University Press.

Burgess, D., Hellinger, P., Gingell, I., & Trávnícek, P. M. (2015). Microstructure in two and three-dimensional hybrid simulations of perpendicular collisionless shocks. *Journal of Plasma Physics*, *82*, 905820401.

Caprioli, D., & Spitkovsky, A. (2014). Simulations of ion acceleration at non-relativistic shocks. I. Acceleration Efficiency. *Astrophysics Journal*, *783*(2), 91.

Caprioli, D., Yi, D., & Spitkovsky, A. (2017). Chemical enhancements in shock-accelerated particles ab initio simulations. *Physical Review Letters*, *119*(17), 1101.

Enriquez-Rivera, O., Blanco-Cano, X. C. T., Russell, L. K., Jian, J. G., & Luhmann (2010). Mirror mode structures in the solar wind: STEREO observations. *AIP Conference Proceedings 2010*, *1216*, 276. https://doi.org/10.1063/1.3395854

Enriquez-Rivera, O., Blanco-Cano, X., Russell, C. T., Jian, L. K., Luhmann, J. G., Simunac, K. D., & Galvin, A. B. (2013). Mirror-mode storms inside stream interaction regions and in the ambient solar wind: A kinetic study. *Journal Geophysical Research: Space Physics*, *118*, 17–28. https://doi.org/10.1029/2012JA018233

Fuselier, S. A., & Schmidt, W. K. H. (1994). H^+ and He^{2+} heating at the Earth's bow shock. *Journal Geophysical Research*, *99*, 11,539–11,546. https://doi.org/10.1029/94JA00350

Fuselier, S. A., & Schmidt, W. K. H. (1997). Solar wind He^{2+} ring-beam distributions downstream from the Earth's bow shock. *Journal Geophysical Research*, *102*, 11,273–11,280. https://doi.org/10.1029/97JA00643

Gary, S. P. (1993). *Theory of space plasma microinstabiblities*. Cambridge: Cambridge University Press.

Gary, S. P., McKean, M. E., & Winske, D. (1996). Proton temperature anisotropy in the magnetosheath: Hybrid simulations. *Geophysical Research Letter*, *23*, 2887–2890.

Gedalin, M. (2017). Effect of alpha particles on the shock structure. *Journal of Geophysical Research: Space Physics*, *122*, 71–76. https://doi.org/10.1002/2016JA023460

Geiss, J., Hirt, P., & Leutwyler, H. (1970). On acceleration and motion of ions in corona and solar wind. *Solar Physical*, *12*, 458.

Gingell (2017). MMS Observations and hybrid simulations of surface ripples at a marginally quasi-parallel shock. *Journal of Geophysical Research: Space Physics*, *122*, 11,003–11,017. https://doi.org/10.1002/2017JA024538

Gosling, J. T., & Thomsen, M. F. (1985). Specularly reflected ions, shock foot thicknesses, and shock velocity determinations in space. *Journal of Geophysical Research*, *90*(Oct. 1, 1985), 9893–9896.

Gosling, J. T., Thomsen, M. F., Bame, S. J., & Russell, C. T. (1989). Ion reflection and downstream thermalization at the quasi-parallel bow shock. *Journal of Geophysical Research*, *94*(Aug. 1,1989), 10,027–10,037.

Hada, T., Oonishi, M., Lembége, B., & Savoini, P. (2003). Shock front nonstationarity of supercritical perpendicular shocks. *Journal Geophysical Research*, *108*(A16), 1233. https://doi.org/10.1029/2002JA009339

Hao, Y., Gao, X., Lu, Q., Huang, C., Wang, R., & Wang, S. (2017). Reformation of rippled quasi-parallel shocks: 2-D hybrid simulations. *Journal Geophysical Research: Space Physics*, *122*, 6385–6396. https://doi.org/10.1002/2017JA024234

Hao, Y., Lu, Q., Gao, X., Huang, C., Lu, S., Shan, L., & Wang, S. (2014). He^{2+} dynamics and ion cyclotron waves in the downstream of quasi-perpendicular shocks: 2-D hybrid simulations. *Journal Geophysical Research: Space Physics*, *119*, 3225–3236. https://doi.org/10.1002/2013JA019717

Hao, Y., Lu, Q., Gao, X., & Wang, S. (2016). Ion dynamics at a rippled quasi-parallel shock: 2D hybrid simulations. *Astrophysics Journal*, *823*(1), 7.

Ipavich, F. M., Gosling, J. T., & Scholer, M. (1984). Correlation between the He/H ratios in upstream particle events and in the solar wind. *Journal of Geophysical Research*, *89*(March 1, 1984), 1501–1507.

Kajdic, P., Blanco-Cano, X., Aguilar-Roriguez, E., Russel, C. T., Jian, L. K., & Luhmann, J. G. (2012). Waves upstream and downstream of interplanetary shocks driven by coronal mass ejections. *Journal Geophysical Research*, *117*, A06103. https://doi.org/10.1029/2011JA017381

Kajdic, P., Preisser, L., Blanco-Cano, X., Burgess, D., & Trotta, D. (2019). First observations of irregular surface of interplanetary shocks at ion scales by cluster. *The Astrophysical Journal Letters*, *874*(2), L13.

Kasper, J. C., Stevens, M. L., Lazarus, A. J., Steinberg, J. T., & Ogilvie, K. W. (2007). Solar wind helium abundance as a function of speed and heliographic latitude: Variation through a solar cycle. *Astrophysics Journal*, *660*, 901.

Krauss-Varban, D. (2005). From theoretical foundation to invaluable research tool: Modem hybrid simulations. In *Proceedings of the 7th International Symposium for Space Simulations (ISSS-7)*, Kyoto Univ.,arXiv:physics/0610133, pp. 15–18.

Lee, M. A., Shapiro, V. D., & Sagdeev, R. Z. (1996). Pickup ion energization by shock surfing. *Journal Geophysical Research*, *101*, 4777.
Lembège, B., & Savoini, P. (1992). Nonstationarity of a two-dimensional quasiperpendicular supercritical collisionless shock by self-reformation. *Physical Fluids B*, *4*, 3533–3548. https://doi.org/10.1063/1.860361
Lu, Q. M., & Wang, S. (2005). Formation of He^{2+} shell-like distributions downstream of the Earth's bow shock. *Geophysical Research Letters*, *32*, L03111. https://doi.org/10.1029/2004GL021508
Lu, Q. M., & Wang, S. (2006). Electromagnetic waves downstream of quasi-perpendicular shocks. *Journal Geophysical Research*, *111*, A05204. https://doi.org/10.1029/2005JA011319
Matthews, A. P. (1994). Current advance method and cyclic leapfrog for 2D multispecies hybrid plasma simulations. *JCoPh*, *112*, 102.
McKean, M. E., Omidi, N., & Krauss-Varban, D. (1995b). Wave and ion evolution downstream of quasi-perpendicular bow shocks. *Journal Geophysical Research*, *100*, 3427.
McKean, M. E., Omidi, N., & Krauss-Varban, D. (1996). Magnetosheath dynamics downstream of low Mach number shocks. *Journal Geophysical Research*, *101*, 20,013–20,022. https://doi.org/10.1029/96JA01461
McKean, M. E., Omidi, N., Krauss-Varban, D., & Karimabadi, H. (1995a). Wave and particle evolution downstream of quasi-perpendicular shocks. *Advance Space Research*, *15*, 319–22.
Motschmann, U., & Glassmeier, K. (1993). Simulation of heavy ion ring and shell distributions downstream of the bow shock. *Geophysical Research Letter*, *20*(10), 987–990.
Neugebauer, M., & Snyder, C. W. (1966). Mariner 2 observations of the solar wind: 1. Average properties. *Journal Geophysical Research*, *71*, 4469.
Ofman, L., Koval, A., Wilson, L., & Szabo, A. (2019). Understanding the role of α particles in oblique heliospheric shock oscillations. *Journal Geophysical Research*, *124*, 2393–2405. https://doi.org/10.1029/2018JA026301
Russell, C. T., & Hoppe, M. (1983). Upstream waves and particles. *SSRv*, *34*, 155.
Scholer, M., & Burgess, D. (1992). The role of upstream waves in supercritical quasi-parallel shock reformation. *Journal Geophysical Research*, *97*, 8319–8326. https://doi.org/10.1029/92JA00312
Scholer, M., Fujimoto, M., & Kucharek, H. (1993). Two-dimensional simulations of supercritical quasi-parallel shocks: upstream waves, downstream waves, and shock reformation. *Journal Geophysical Research*, *98*, 18971.
Scholer, M., & Terasawa, T. (1990). Ion reflection and dissipation at quasi-parallel collisionless shocks. *Geophysical Research Letters*, *17*, 119–122. https://doi.org/10.1029/GL017i002p00119
Sckopke, N., Paschmann, G., Brinca, A. L., Carlson, C. W., & Lühr, H (1990). Ion thermalization in quasi-perpendicular shocks involving reflected ions. *Journal Geophysical Research*, *95*(A5), 6337–6352.
Siu-Tapia, A., Blanco-Cano, X., Kajdic, P., Aguilar-Rodriguez, E., Russell, C. T., Jian, L. K., & Luhmann, J. G. (2015). Low-frequency waves within isolated magnetic clouds and complex structures: STEREO observations. *Journal Geophysical Research: Space Physics*, *120*, 2363–2381. https://doi.org/10.1002/2014JA020568
Southwood, D. J., & Kivelson, M. G. (1993). Mirror instability: I. Physical mechanism of linear instability. *Journal Geophysical Research*, *98*, 9181.
Su, Y., Lu, Q., Gao, X., Huang, C., & Wang, S. (2012a). Ion dynamics at supercritical quasi-parallel shocks: Hybrid simulations. *Physical Plasmas*, *19*(092108).
Su, Y., Lu, Q., Huang, C., Wu, M., Gao, X., & Wang, S. (2012b). Particle acceleration and generation of diffuse superthermal ions at a quasi-parallel collisionless shock: Hybrid simulations. *Journal Geophysical Research*, *117*, A08107. https://doi.org/10.1029/2012JA017736
Sundberg, T., Haynes, C. T., Burgess, D., & Mazelle, C. X. (2016). Ion acceleration at the quasi-parallel bow shock: Decoding the signature of injection. *Astrophysical Journal*, *820*, 21.
Trattner, K. J., & Scholer, M. (1991). Diffuse Alpha particles upstream of simulated quasi-parallel supercritical collisionless shocks. *Geophysical Research Letter*, *18*(Oct. 1991), 1817–1820.
Trattner, K. J., & Scholer, M. (1993). Distributions and thermalization of protons and alpha particles at collisionless quasi-parallel shocks. *Annales Geophysicae*, *11*(9), 774–789.
Trattner, K. J., & Scholer, M. (1994). Diffuse minor ions upstream of simulated quasi-parallel shocks. *Journal of Geophysical Research*, *99*(A4), 6637–6650.
Trotta, D., & Burgess, D. (1994). Electron acceleration at quasi-perpendicular shocks in sub and supercritical regimes: 2D and 3D simulations. *Monthly Notices of the Royal Astronomical Society*, *482*(1), 1154–1162.
Tsubouchi, K., Nagai, T., & Shinohara, I. (2016). Stable ring beam of solar wind He^{2+} in the magnetosheath. *Journal Geophysical Research: Space Physics*, *121*, 1233–1248. https://doi.org/10.1002/2015JA021769
Wilson, L. B. (2016). Low frequency waves at and upstream of collisionless shocks. *Washington DC American Geophysical Union Geophysical Monograph Series*, *216*, 269–291.
Winske, D., & Leroy, M. M. (1985). Hybrid simulation techniques applied to the Earth's bow shock. In H. M. T. Sato (Ed.), *Computer Simulation of Space Plasmas* (pp. 255–278). Japan: Terra Science Tokyo.
Wurz, P. (2005). Solar Wind Composition. Proceedings of the 11Th European Solar Physics Meeting "The Dynamic Sun: Challenges for Theory and Observations" (ESA SP-600). 11-16 September 2005, Leuven, Belgium. Editors: D. Danesy S, Poedts A. De Groof and J. Andries."
Yang, Z. W., Lembège, B., & Lu, Q. M. (2012). Impact of the rippling of a perpendicular shock front on ion dynamics. *Journal Geophysical Research*, *117*, A07222. https://doi.org/10.1029/2011JA017211
Yang, Z. W., Lu, Q. M., Lembège, B., & Wang, S. (2009). Shock front nonstationarity and ion acceleration in supercritical perpendicular shocks. *Journal Geophysical Research*, *114*, A03111. https://doi.org/10.1029/2008JA013785

Capítulo 3

Características y mecanismos de formación de jets y plasmoides en la magnetofunda usando simulaciones numéricas híbridas.

3.1. Resumen del trabajo y metodología

En este trabajo se estudiaron las características y mecanismos de formación de dos estructuras típicamente observadas en la magnetofunda terrestre, a saber jets (Plaschke et al., 2018) y plasmoides (Karlsson et al., 2012, 2015). Dicho estudio fue realizado a partir de los resultados de una simulación híbrida de un choque cuasi-paralelo con θ_{Bn} =15° usando el código HYPSI (Burgess and Scholer, 2015; Gingell et al., 2017). La motivación del estudio es la reciente discusión sobre la relación entre estos dos fenómenos (Karlsson et al., 2015; Plaschke et al., 2018). Si bien es cierto que estas estructuras han tratado de ser caracterízadas observacionalmente desde su primera detección hace poco más de veinte años (Němeček et al., 1998), el estudio sobre su formación y evolución ha sido más bien pobre aunque algunos mecanismos de generación han sido propuestos de manera teórica (para un resumen ver Plaschke et al. (2018)).

En la simulación hemos podido identificar ambos tipos de estructura, las cuáles han sido caracterizadas a partir de criterios observacionales reportados en trabajos previos (Karlsson et al., 2015; Plaschke et al., 2013). Sacando provecho de la ventaja que las simulaciones tienen al poder ir en reversa con respecto al tiempo, hemos sido capaces de estudiar de manera detallada los mecanismos de formación de ambas estructuras.

Los resultados de dicho estudio han demostrado por primera vez y de manera clara que los jets y plasmoides que cumplen criterios de identificación observacionales pueden ser generados en la interfaz del choque siguiendo dos mecanismos diferentes: El jet es formado en una de las arrugas del frente de choque donde el plasma río arriba es fácilmente deflectado y después focalizado hacia la región río abajo incrementando, la presión dinámica localmente, de acuerdo al mecanismo propuesto recientemente por Hietala et al. (2009). Por otro lado, el plasmoide se forma cuando dos franjas de plasma con campo magnético opuesto y que son producto de la reformación local del choque (Scholer and Burgess, 1992), interaccionan y son reconectadas, produciendo una estructura magnética en forma de bucle que aisla el plasma contenido en éste. El aislamiento magnético de ésta estructura permite que la densidad dentro de ésta sea mayor que la de los alrededores asi como que la estructura pueda ser transportada por el flujo que lo rodea hacia la región río abajo. Ambas características permiten clasificar este fenómeno como un plasmoide paramagnético embebido de acuerdo con el trabajo observacional de Karlsson et al. (2015).

Nuestro estudio muestra que si bien ambas estructuras poseen la característica de un incremento en la presión dinámica por lo que podrían ser considerados o clasificados como jets, dependiendo de la definición usada (ver para un resumen Plaschke et al. (2018)), no tienen la misma estructura interna ni son producto del mismo mecanismo de formación, al menos con los parámetros utilizados en la simulación lo cual debería ser tomado en cuenta en futuros trabajos tanto observacionales como teóricos.

3.2. Publicación en Astrophysical Journal Letters (ApJL) (2020)

The Astrophysical Journal Letters, 900:L6 (9pp), 2020 September 1 https://doi.org/10.3847/2041-8213/abad2b

Magnetosheath Jets and Plasmoids: Characteristics and Formation Mechanisms from Hybrid Simulations

Luis Preisser[1], Xóchitl Blanco-Cano[1], Primoz Kajdič[1], David Burgess[2], and Domenico Trotta[2]
[1] Instituto de Geofísica UNAM Circuito de la Investigación Científica s/n, Coyoacán 04510, Mexico City, Mexico; preisser@igeofisica.unam.mx
[2] School of Physics and Astronomy, Queen Mary University of London London E1 4NS, UK
Received 2020 May 8; revised 2020 July 28; accepted 2020 August 6; published 2020 August 26

Abstract

Magnetosheath jets and plasmoids are very common phenomena downstream of Earth's quasi-parallel bow shock. As the increase of the dynamic pressure is one of the principal characteristics of magnetosheath jets, the embedded paramagnetic plasmoids have been considered as an special case of the former. Although the properties of both types of structures have been widely studied during the last 20 years, their formation mechanisms have not been examined thoroughly. In this work we perform a 2D local hybrid simulation (kinetic ions – fluid electrons) of a quasi-parallel ($\theta_{Bn} = 15°$), supercritical ($M_A = 7$) collisionless shock in order to study these mechanisms. Specifically, we analyze the formation of one jet and one plasmoid, showing for the first time that they can be produced by different mechanisms related to the same shock. In our simulation, the magnetosheath jet is formed according to the mechanism proposed by Hietala, where at the shock ripples the upstream solar wind suffers locally less deceleration and the flow is focused in the downstream side, producing a compressed and high-velocity region that leads to an increase of dynamic pressure downstream of the shock. The formation of the plasmoid, however, follows a completely new scenario being generated by magnetic reconnection between two plasma layers with opposite *B*-field orientation in the region just behind the shock.

Unified Astronomy Thesaurus concepts: Shocks (2086); Interplanetary medium (825); Interplanetary shocks (829); Planetary bow shocks (1246); Space plasmas (1544); Plasma astrophysics (1261); Plasma physics (2089); Heliosphere (711); Space weather (2037)

1. Introduction

When the super-magnetosonic solar wind (SW) encounters the Earth's bow shock, it is decelerated to sub-magnetosonic speeds (e.g., Tsurutani & Stone 1985; Burgess 1995; Burgess & Scholer 2015). Due to its collisionless nature, the bow shock is strongly rippled especially where its geometry, characterized by the angle θ_{Bn} between the shock's local normal and the upstream interplanetary magnetic field, is quasi-parallel ($\theta_{Bn} < 45°$, e.g., Burgess 1989; Krauss-Varban & Omidi 1991; Schwartz & Burgess 1991; Blanco-Cano et al. 2009). Downstream of the bow shock there is a region called the magnetosheath (Lucek et al. 2005), which, in the case of a quasi-parallel bow shock, is populated by strong *B*-field and plasma fluctuations. Most of the time the observed fluctuations are either turbulence (Omidi et al. 1994; Shevyrev et al. 2003; Shevyrev & Zastenker 2005; Yordanova et al. 2016; Rakhmanova et al. 2018), ion-cyclotron waves, or mirror-mode fluctuations (e.g., Schwartz et al. 1996, and references therein).

There is another type of structures in the magnetosheath, commonly called magnetosheath jets (Plaschke et al. 2018, and references therein). These jets were first described by Němeček et al. (1998) as transient and local ion flux enhancements. Later, they were more commonly defined as enhancements of dynamic pressure ($P_{\rm dyn}$, Archer et al. 2012; Hietala et al. 2012; Archer & Horbury 2013; Savin et al. 2014), increments in dynamic pressure calculated with only the V_x component ($P_{{\rm dyn},x}$, Plaschke et al. 2013) and changes in plasma velocity (Hietala et al. 2012; Gunell et al. 2014). Because the identification of an enhancement requires a threshold, some authors have used values calculated with respect to the background magnetosheath plasma (e.g., Archer & Horbury 2013) while others use upstream SW properties (e.g., Amata et al. 2011; Plaschke et al. 2013).

In order to study the jet formation mechanism triggered for upstream conditions, in this work we will consider as a jet any structure that fulfills the following identification conditions adapted from Plaschke et al. (2013) and illustrated in Figure 1(a).

1. Within a jet $P_{{\rm dyn},x,{\rm jet}} \geqslant 0.5\, P_{{\rm dyn},x,{\rm up}}$, where $P_{{\rm dyn},x,{\rm jet}}$ and $P_{{\rm dyn},x,{\rm up}}$ are values inside the jet and upstream of the bow shock.
2. The jet interval is delimited by the condition $P_{{\rm dyn},x,{\rm jet}} \geqslant 0.25\, P_{{\rm dyn},x,{\rm up}}$.
3. Before and after the jet interval the condition $V_{x,{\rm down}} \geqslant 0.5\, V_{x,{\rm down}}(t_0)$ must be satisfied (t_0 is the time of the peak in $P_{{\rm dyn},x,{\rm jet}}$). This ensures velocity enhancements confined to the respective jet interval, and not simply density enhancements within a steady flow.
4. V_x throughout the jet is negative (anti-sunward propagation).

In addition to its characterization (see Tables 1 and 2 in Plaschke et al. 2018), different formation mechanisms have been proposed for magnetosheath jets. Hietala et al. (2009) suggested that jets are formed at bow-shock ripples. The idea is that at these ripples, the incoming SW plasma is locally decelerated less than the surrounding plasma being focused and additionally compressed in the downstream region leading to a local increase of $P_{\rm dyn}$ observed in the magnetosheath. Archer et al. (2012) linked jets to upstream rotational discontinuities transmitted to the magnetosheath region, while Savin et al. (2012) associated them to hot flow anomalies (e.g., Lucek et al. 2004; Omidi & Sibeck 2007). In a recent work using an hybrid simulation

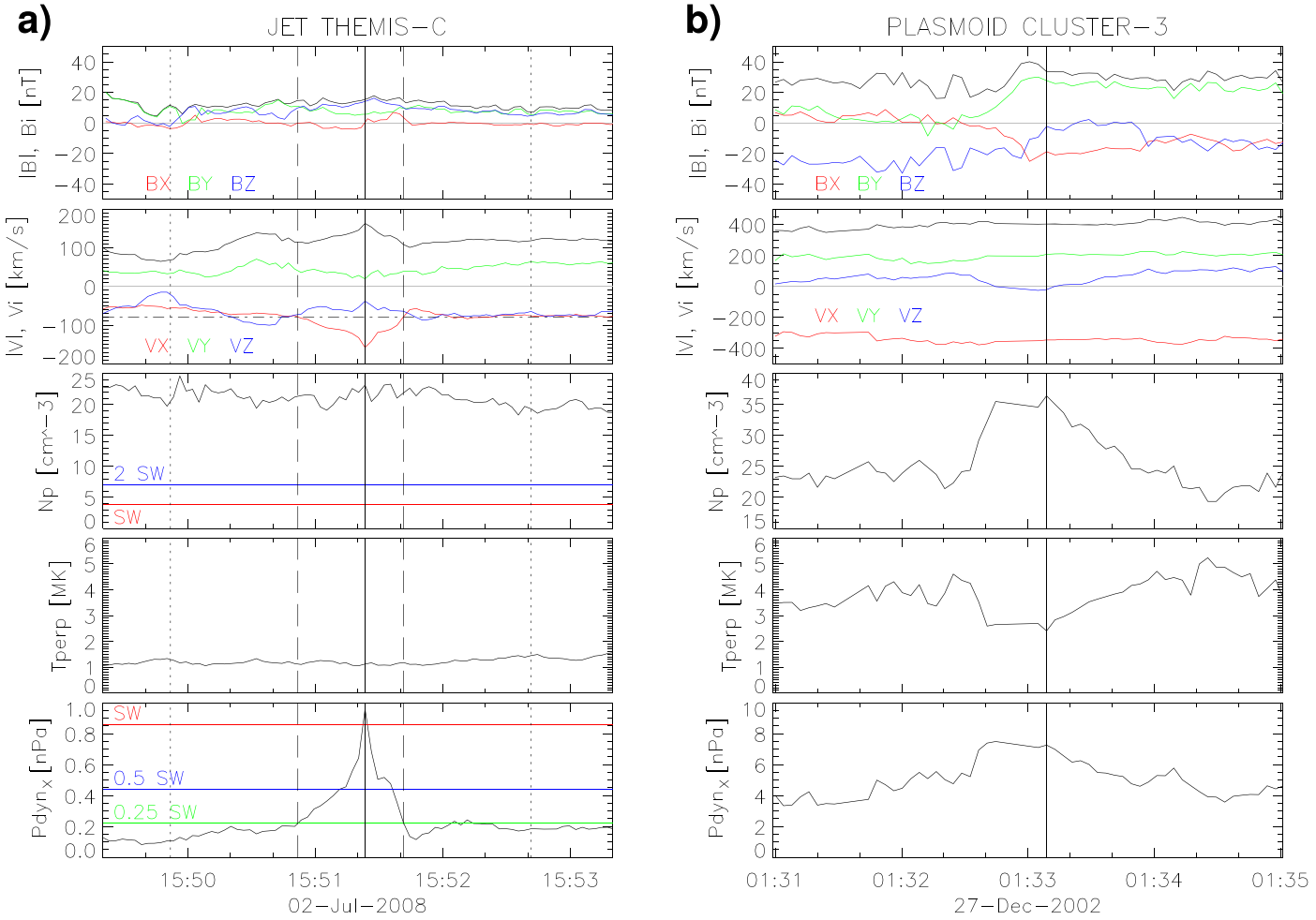

Figure 1. (a) Jet observed by THEMIS-C (adapted from Plaschke et al. 2013). (b) Paramagnetic embedded plasmoid observed by CLUSTER-3 (adapted from Karlsson et al. 2015). From top to bottom, magnetic field and bulk velocity measurements in GSE coordinates, ion density, perpendicular ion temperature and $P_{\mathrm{dyn},x}$.

Hao et al. (2016a) show how a magnetic filamentary structure with high P_{dyn} is formed downstream of a 30° quasi-parallel shock.

On the other hand, closely related structures called plasmoids have been studied from a different point of view, in the form of density enhancements over the background values without any a priori connection to an increase in the flow velocity (e.g., Hubert & Harvey 2000; Karlsson et al. 2012, 2015; Gutynska et al. 2015). In a statistical study Karlsson et al. (2012) found that all of them were associated with magnetic field rotation and an increase or decrease of B-magnitude. Karlsson et al. (2015) showed that two distinct categories of plasmoids can exist. The first category with a diamagnetic signature (decrease in B-field magnitude) is found in both SW and magnetosheath regions. The second plasmoid population were only found in the magnetosheath, exhibiting a paramagnetic signature (increase in magnetic field magnitude) and they could have (or not have) an associated increase in velocity.

Focusing on the latter, here we consider a paramagnetic embedded plasmoid to be any magnetosheath structure that satisfies the following criteria (based on Karlsson et al. 2015) and also illustrated with an observational case in Figure 1(b).

1. Localized ion density enhancement of 30% over the average ambient value.
2. Increment in B-magnitude between 0% and 50% above the average, accompanied by a change in direction of at least one of the magnetic components.
3. Bulk velocity enhancements of $\leqslant$10% compared to ambient values.
4. Decrement in perpendicular temperature $T_{\perp}$.

For the generation of magnetosheath plasmoids Karlsson et al. (2012) proposed that diamagnetic plasmoids from the pristine SW can be transmitted into the magnetosheath, while the paramagnetic plasmoids could be formed when short, large-amplitude magnetic structures (SLAMS; Schwartz et al. 1992; Giacalone et al. 1993; Dubouloz & Scholer 1995; Tsubouchi & Lembège 2004) cross from the foreshock (Eastwood et al. 2005) into the magnetosheath.

As pointed out by Karlsson et al. (2015), a comparison of the properties of jets and plasmoids is of great interest as it could help to determine whether or not their generation mechanisms are the same. Following these arguments, here we study via local hybrid simulations jets and plasmoids as entities with different signatures, showing for the first time that they can be formed by the same shock but by two different mechanisms. For the plasmoid we show for the first time that its formation is related to magnetic reconnection in the region just behind the shock.

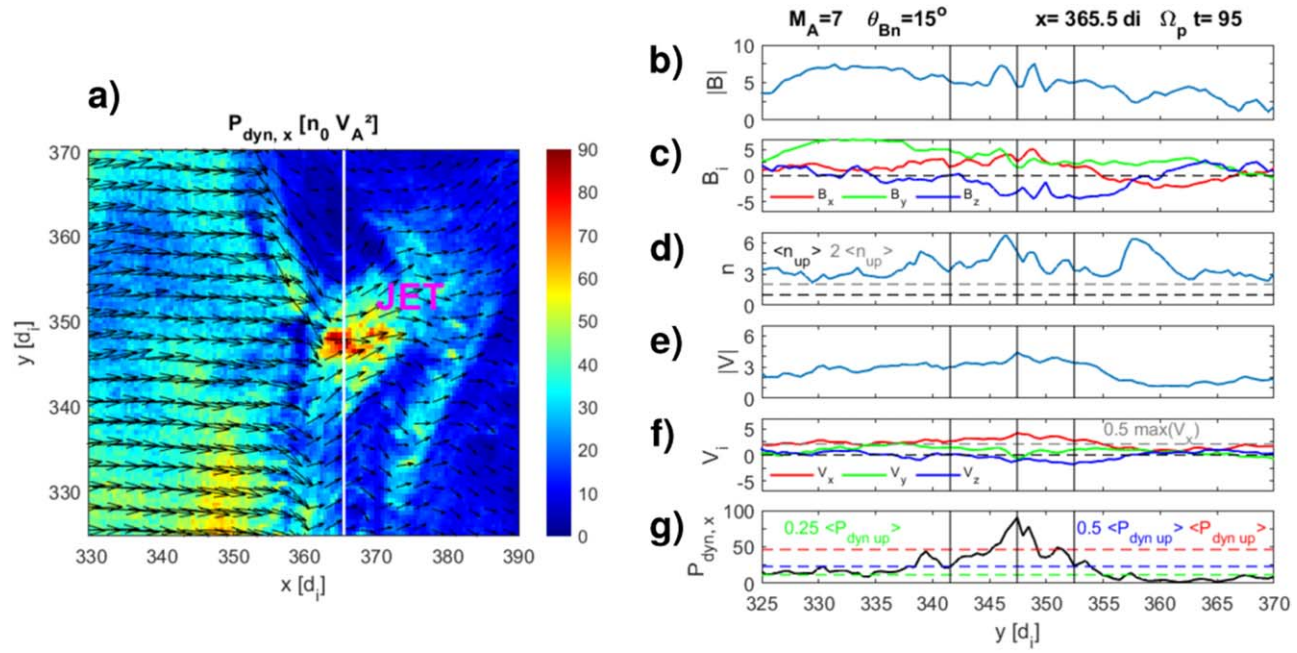

Figure 2. (a) $P_{\mathrm{dyn},x}$ in colors and bulk velocity (vectors) at $\Omega_p\ t = 365.5$. The white line indicates the cut through the jet along which the following spatial profile parameters are plotted: (b) magnetic field magnitude, (c) B-field components, (d) ion density (the horizontal black and gray lines correspond to the upstream value n and $n/2$ respectively), (e) ion bulk velocity, (f) velocity components (the value corresponding to half the maximum of V_x inside the jet is indicated with the gray horizontal line), and (g) $P_{dyn,x}$ (averaged upstream values corresponding to $P_{\mathrm{dyn},x}$, $P_{\mathrm{dyn},x}/2$ and $P_{\mathrm{dyn},x}/4$ are indicated in red, blue, and green lines). The central vertical line on panels (b)–(g) marks the maximum of $P_{\mathrm{dyn},x}$ while the left and the right vertical lines delimit the jet defined as the locations around the $P_{\mathrm{dyn},x}$ maximum where $P_{\mathrm{dyn},x} = 0.5\langle P_{\mathrm{dyn},x}\rangle_{\mathrm{up}}$.

2. Numerical Setup

The simulation was performed using the hybrid particle-In-cell code HYPSI (Burgess & Scholer 2015; Gingell et al. 2017). Under this approach protons are treated kinetically while electrons are considered as a charge-neutralizing massless fluid. Spatial and temporal scales are expressed in units of proton inertial length $d_i = c/\omega_p$ (ω_p is the proton plasma frequency, c is the speed of light) and the inverse of the proton gyrofrequency Ω_p^{-1}, respectively, while the velocity is normalized to the Alfvén speed $V_A = B_{\mathrm{up}}/\sqrt{\mu_o n_o m_p}$. Proton density n_o m_p and magnetic field B_{up} are normalized to the initial upstream values. The number of grid cells is $n_x \times n_y = 1000 \times 800$, with cell sizes of $\Delta x = \Delta y = 0.5\ c/\omega_p$. The time step Δt was chosen so that $\Omega_p\ \ \Delta t = 0.005$. The velocity, magnetic field, and electric field are 3D vectors. The plasma was initialized with an inflow speed $V_{\mathrm{in}} = 5.5\ V_A$ along the x-direction with the magnetic field in the x–y simulation plane forming an angle (the nominal θ_{Bn}) of 15° with the x-axis. The right boundary of the simulation acts as a perfectly reflecting wall to the plasma that is continuously injected from the left open boundary. The simulation is periodic in the y direction. As a consequence of the interaction between the reflected and injected plasma, a shock propagating in the negative x-direction with a $M_A = 7$ is formed. A finite resistivity, $\eta = 0.06\ \omega_p^{-1}$ is used in the simulations with an isotropic upstream Maxwellian velocity distribution function for protons, and upstream plasma beta (the ratio of kinetic to magnetic pressure) $\beta_p = \beta_e = 0.5$. The initial number of particles per cell is ~100. In the box simulation frame the shock moves to the left. The velocities and then the dynamic pressure for this work were computed in the shock reference frame.

3. Simulation Results

Our simulation reproduces the inherent and well-known structures of quasi-parallel shocks, such as ripples along the shock surface and fluctuations in plasma parameters on both sides of the shock in agreement with previous simulation works (Burgess 1989; Krauss-Varban & Omidi 1991; Burgess 1995; Hao et al. 2016a, 2016b, 2017). After an inspection of downstream parameters we identified a jet and a paramagnetic embedded plasmoid based on the criteria defined in Section 1.

3.1. Reproducing the Observational Signatures

Figure 2(a) shows an excerpt of the simulation domain at $\Omega_p\ t = 95$. The colors represent $P_{\mathrm{dyn},x}$ while the black arrows show the local direction of the plasma velocity. The rippled shock front is easily identified by the abrupt change in direction of the velocity around $x = 360\ d_i$, which coincides with the change of $P_{\mathrm{dyn},x}$ from ~35 $n_0 V_A^2$ in the upstream side to ~15 $n_0 V_A^2$ in the downstream region. Most of the downstream region exhibits low $P_{\mathrm{dyn},x}$ values (blue color) with exception of the region marked as "JET" where large $P_{\mathrm{dyn},x}$ values between 40 and 90 $n_0 V_A^2$ are present. This region extends between $x \sim 355$–$380\ d_i$ and $y \sim 340$–$355\ d_i$. This feature is in qualitative agreement with the physical picture of jet generation proposed in Hietala et al. (2009) and Hietala & Plaschke (2013). We analyze the behavior of different plasma parameters along the white line at $x = 365.5\ d_i$ in Figure 2(a) containing the maximum value of $P_{\mathrm{dyn},x} \sim 90\ n_0 V_A^2$ as seen in Figure 2(g). This simulated jet fulfills the observational criteria in Section 1 and exemplified in Figure 1(a).

1. Within the jet $P_{\mathrm{dyn},x}$ exceeds half of the upstream dynamic pressure (horizontal red line in Figure 2(g)). The maximum $P_{\mathrm{dyn},x} \sim 90\ n_0 V_A^2$ located at $x = 47.5\ d_i$ is

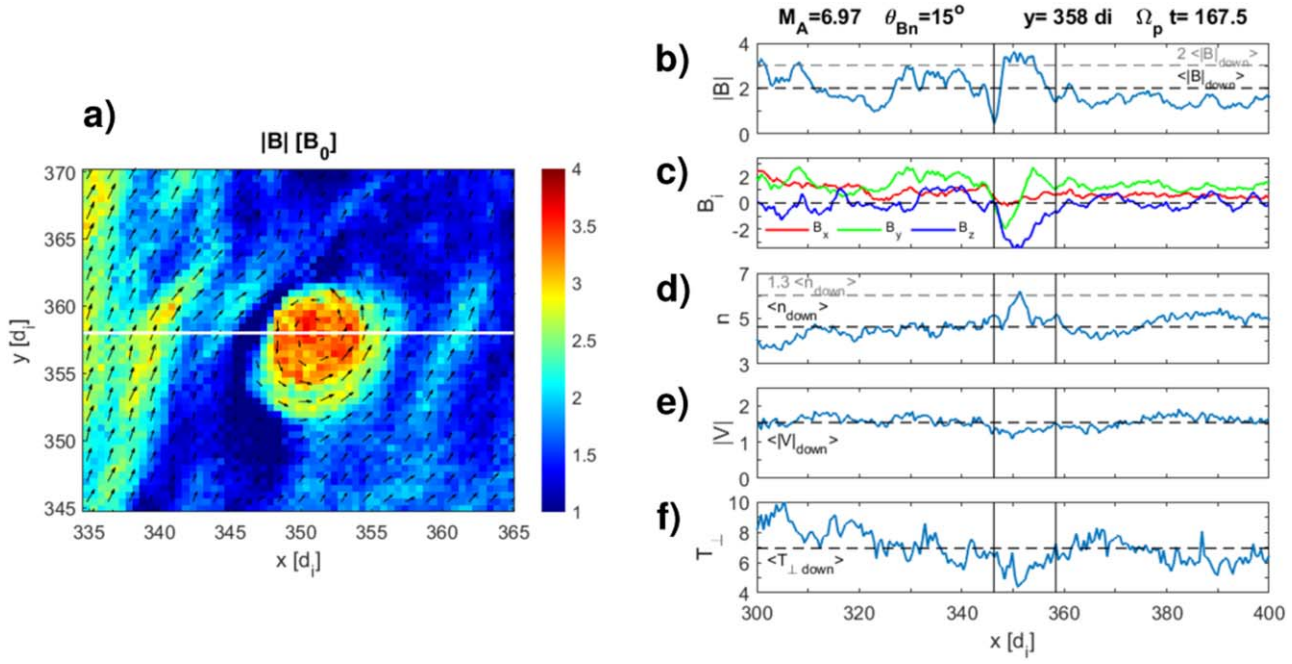

Figure 3. (a) B-field magnitude (colors) and direction (vectors) at $\Omega_p\, t = 167.5$ for a downstream region of the simulation box. The white line indicates the cut through the plasmoid along which the following spatial profile parameters are plotted: (b) B-field magnitude (averaged downstream values corresponding to $|B|$ and $2|B|$ in black and gray), (c) B-field components, (d) ion density (averaged downstream values corresponding to n and $1.3n$ in black and gray), (e) ion bulk velocity (averaged downstream value in black), and (f) perpendicular temperature (averaged downstream value in black). The vertical lines in the right panels identify the boundary of the plasmoid defined as the local minimums around the B-field magnitude peak.

2.6 times greater than the upstream value. The jet spatial width (between the first and third vertical lines) is approximately 16 d_i, which corresponds to 1600 km assuming a typical d_i value in the upstream region of ∼100 km, in agreement with the values between 1200 and 7000 km found by Plaschke et 9l. (2013).

2. Inside the jet, the ion bulk velocity in the x-direction (red trace in Figure 2(f)) is positive, which is equivalent to the anti-sunward propagation as required by Plaschke et al. (2013).
3. Additionally, an increment in ion density (Figure 2(d)) and magnetic field magnitude (Figure 2(b)) inside the jet interval are present.

Figure 3(a) shows a snapshot at $\Omega_p\, t = 167.5$ of a different region of the simulation box. The colors represent the B-field magnitude, while the black arrows indicate its direction. The shock position is not seen because it is located at $x \sim 300\ d_i$. A circular structure with a larger magnetic field ($\sim 3.2\, B_0$) compared with the surroundings can be identified. The B-field vectors inside this structure present rotation in the counterclockwise direction. We examine different plasma parameters along the white line in Figure 3(a) at $y = 358\ d_i$. The ion density (Figure 3(d)) shows an increase ($n \sim 6\ n_0$) inside the structure. We define the boundaries of the structure as the locations of local minimum of the B-magnitude as shown in Figure 3(b). The characteristics listed below fulfill the observational signatures of paramagnetic embedded plasmoids defined in Section 1 and illustrated in Figure 1(b).

1. The ion density enhancement at $x \sim 252\ d_i$ reaches 1.3 times the averaged density value in the downstream region (Figure 3(d)).
2. The increment in B-field magnitude exceeds twice the average value in the downstream region (Figure 3(b)).
3. The magnetic field components inside the plasmoid exhibit smooth rotations (Figure 3(c)).
4. Velocity values are similar to those in the ambient plasma (Figure 3(e)).
5. There is a decrease in perpendicular temperature compared to the downstream average value (Figure 3(f)).

3.2. Formation Mechanisms

In order to study the formation and evolution of the identified jet and plasmoid, we show in Figures 4 and 5 some snapshots of parts of the simulation domain at different times.

The evolution of the jet is presented in Figure 4 where rows show snapshots of different parameters inside the same region at $\Omega_p\, t = 90, 92.5, 95$. From left to right the colors on the panels represent $P_{\mathrm{dyn},x}$, proton density, V_x component of bulk velocity and B-field magnitude. In all panels the plasma velocity vectors are superimposed. The rippled shock transition can be identified by the clear increase of B-field magnitude and density and the decrement in $P_{\mathrm{dyn},x}$ and V_x around $x \sim 360\ d_i$. In the upstream side and along the rippled shock front, the plasma flow is directed approximately parallel to the x-axis. At $\Omega_p\, t = 90$ immediately downstream of the shock $P_{dyn,x}$ is already somewhat enhanced ($y \sim 345$–$360\ d_i$) compared to the surrounding downstream plasma. The initially horizontal flow then evolves at $\Omega_p\, t = 92.5\ d_i$ to a converging and high-velocity plasma downstream of the now more concave part of the ripple that allows the enhancement of local plasma density and the growth of the region with enhanced $P_{\mathrm{dyn},x}$ that extends further downstream. By $\Omega_p\, t = 95$ a clear structure with high $P_{\mathrm{dyn},x}$ due to the corresponding increments in density and velocity in x-direction is created and detached from the shock front. At the downstream edge of the jet the plasma flow seems to diverge. The jet signatures are not clear on the panels showing the B-field magnitude. However, we can see that the jet forms between the shock front

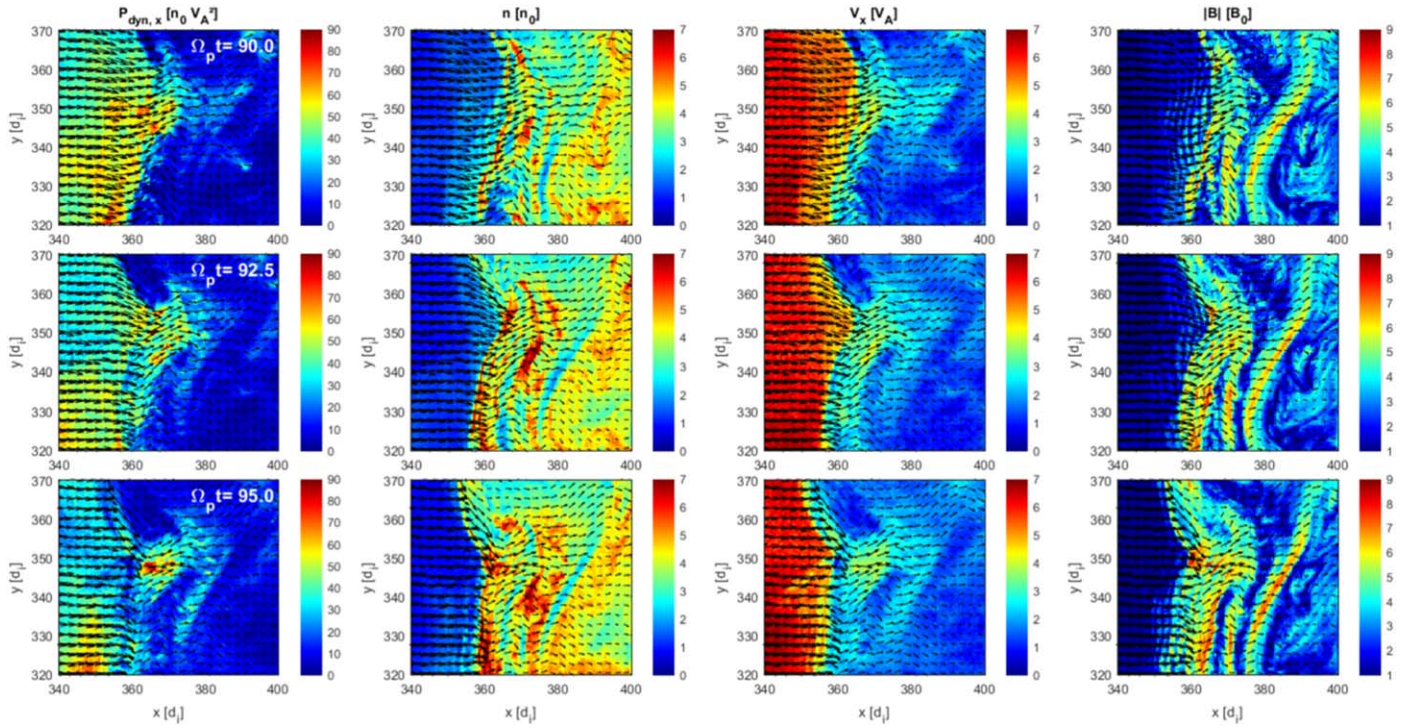

Figure 4. From left to right, isocolor snapshots of $P_{\mathrm{dyn},x}$, proton density, V_x component of bulk velocity, and B-field magnitude. Bulk velocity vectors are superimposed. The different times (rows) correspond to $\Omega_p\, t = 90$, 92.5, 95 and show the evolution of the shock ripple which gives rise to the formation of the jet reported in Figure 2 in agreement with Hietala et al. (2009).

and a filament of enhanced B, which corresponds to the peak from a previous shock reformation cycle (Burgess 1989, 1995; Scholer & Burgess 1992; Su et al. 2012; Hao et al. 2017). Due to the diverging plasma flow at the downstream edge of the jet at $\Omega_p\, t = 95$, the region of enhanced B-field spreads but it does not coincide with the enhanced $P_{\mathrm{dyn},x}$ region of the jet.

The formation of the plasmoid is presented in Figure 5, where plots show a region of the simulation domain at $\Omega_p\, t = 95$, 105, 112.5, 117.5. Intermediate times can be examined in Figures A1 and A2 in the Appendix. The colors from left to right in the panels represent plasma density, B-field magnitude, B_y magnitude colored according to its positive (fading red) or negative (fading blue) direction, and B-field magnitude and direction (white arrows) inside the fixed white square on the first three columns. The shock front is identified by the abrupt jump in plasma density and B-field magnitude. Unlike the jet formation mechanism, the evolution of the plasmoid occurs over a longer period of time ($\Omega_p\, t > 10$). The plasmoid starts to form just behind the shock at $\Omega_p\, t = 95$ when two layers of plasma, product of shock reformation, having opposite B_y magnetic fields are brought together. By $\Omega_p\, t = 105$ as can be identified in the panel corresponding to enlarged view of B-field an elongated and deformed "U"-shaped red structure with an aligned magnetic field is formed in the region at $x \sim 355$–$365\ d_i$ and $y \sim 340$–$350\ d_i$. At $\Omega_p\, t = 112.5$ this structure continues to travel to the downstream region shrinking as the legs of the "U" approach each other. By $\Omega_p\, t = 117.5$ the B-field vectors already show a counter-clockwise loop, indicating that reconnection has closed the magnetic loop. As the simulation evolves by $\Omega_p\, t = 130$ (see Figures A1 and A2 in the Appendix), the plasmoid can be easily identified on density and B panels. This magnetically confined density bump is convected downstream with the surrounding plasma. The fact that the plasmoid stays in the same location ($x \sim 355\ d_i$) from the early stages of formation corroborates the embedded nature of the plasmoid, namely that it is transported with the downstream flow. The plasmoid stays embedded throughout its existence (see Figures A1 and A2 in the Appendix), which lasts until $\Omega_p\, t \sim 200$.

4. Discussion and Conclusions

In this work we present a simulation study where we reproduce the observational signatures of a magnetosheath jet and a paramagnetic embedded plasmoid. We show for the first time that these structures are formed by different mechanisms. For the paramagnetic embedded plasmoid the formation mechanism has not been previously proposed. In this sense, and for the parameters of the simulation similar to those found at the bow shock, jets and plasmoids can be considered as different entities in both their properties and formation mechanisms.

The formation of the simulated jet follows the mechanism proposed by Hietala et al. (2009) along the rippled quasi-parallel shock interface, that is, at the ripple where the shock normal and the flow velocity are not parallel, the incident plasma is less decelerated and more deflected than the surrounding material leading to a local concurrence of material in the downstream region. Both features produce the formation of the enhanced $P_{\mathrm{dyn},x}$ structure that we identified as the jet. Our results differ from those recently found in an hybrid simulation by Hao et al. (2016a), who did not observe the focusing effect mentioned by Hietala et al. (2009), although they did observe increased B-field magnitude along its filamentary jet. Moreover, their mechanism includes a downstream secondary shock as an obstacle that allows the deflection of the flow in the downstream region. The discrepancies between our results and theirs can be due to the differences in their simulation setup (e.g., $\theta_{Bn} = 30^\circ$ and $M_A = 5.5$).

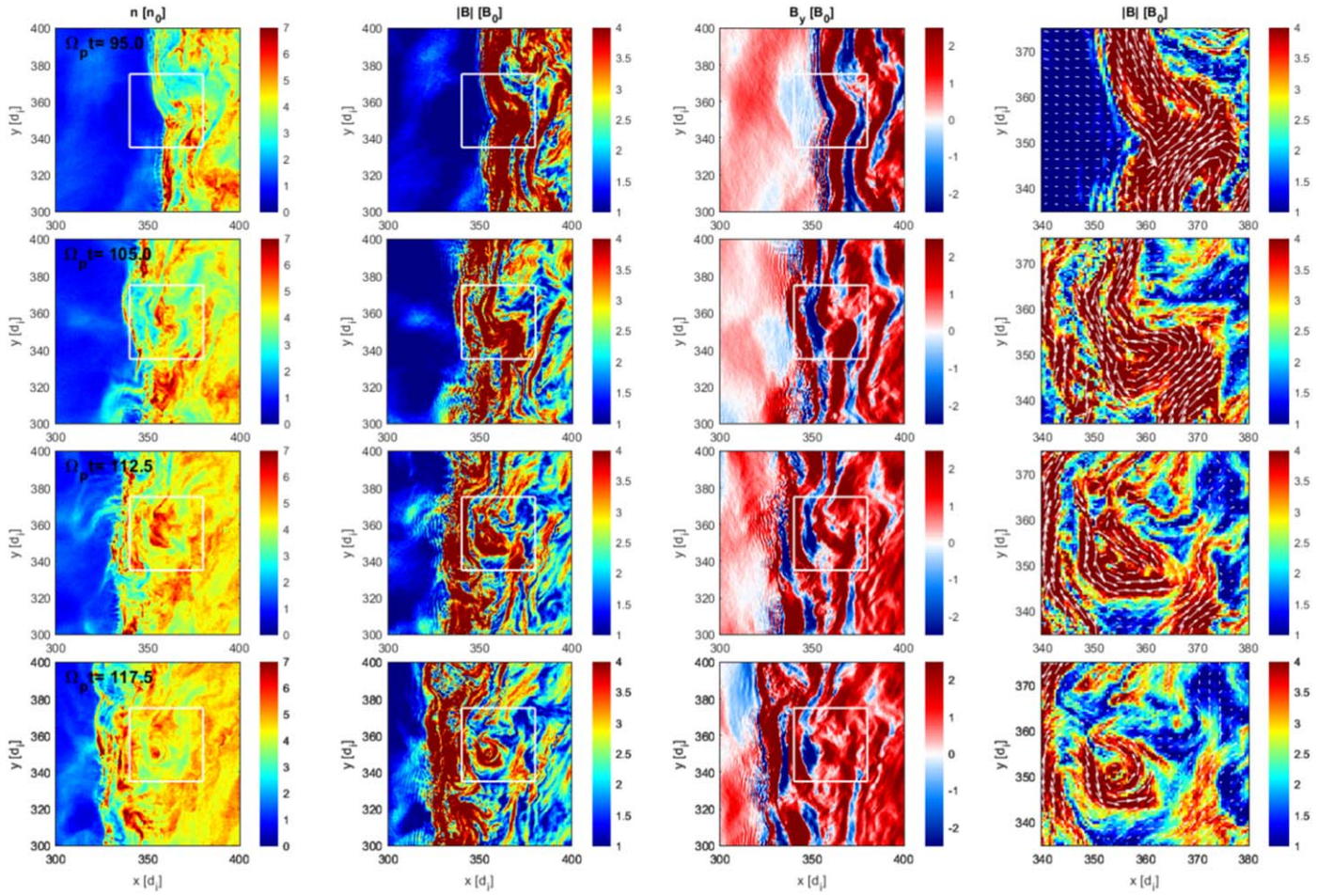

Figure 5. From left to right, isocolor snapshots of ion density, B-field magnitude, B_y magnitude colored according its positive (fading red) or negative (fading blue) direction, and B-field magnitude (isocolors and vectors) in the region delimited by the white square. The different times (rows) corresponds to $\Omega_p\, t = 95$, 105.0, 112.5, 117.5 and show the evolution of the shock region where the plasmoid ($\Omega_p\, t = 117.5$) is formed and which will evolve to that reported in Figure 3(a). The extended formation timeline is shown in Figures A1 and A2 in the Appendix.

On the other hand, the simulated plasmoid is formed at the immediate downstream region by the magnetic reconnection of two opposite B_y-oriented plasma layers that are piling up behind the shock due to the local reformation process characteristic of quasi-parallel shocks (Hao et al. 2016a, 2017). This mechanism gives rise to the formation of a B-field loop, which detaches the plasma inside it from the surroundings, allowing its transport with the downstream. This is the first time that this mechanism is suggested for the formation of paramagnetic embedded plasmoids characterized observationally by Karlsson et al. (2012, 2015). Shock reformation that can be due to upstream waves, shocklets, and SLAMS is then crucial because as these no linear magnetic structures pile up at the shock and become part of the downstream region where the B-field fluctuates rapidly, they change its orientation by up to 180° across small distances. Such large shear angles between the plasma layers provide the ideal conditions for the onset of magnetic reconnection, which eventually leads to the formation of plasmoids.

It is then clear how the different formation mechanisms of jets and paramagnetic embedded plasmoids also can explain some of the differences between their signatures: the magnetically confined nature of the plasmoid is responsible for its high density compared with the surroundings by isolating the plasma inside it inhibiting its diffusion as it is transported downstream. In contrast, the increment in density observed inside some jets is explained by the focusing effect at the ripple, which also increase the V_x component in the same region producing the bump in $P_{\mathrm{din},x}$. Also, due to its embedded nature the paramagnetic plasmoid does not present an increase in velocity and its life time is longer than that of the jet, so it would be more easily found away from the shock front compared to the jet.

These novel results have interesting implications in the context of recent works (Karlsson et al. 2015; Plaschke et al. 2018), which suggest that paramagnetic embedded plasmoids can be regarded as a subset of magnetosheath jets because both present a local increase in $P_{\mathrm{dyn},x}$ (see Figure 1). Although the two structures found in the simulation do share this characteristic, clearly it is not produced by the same mechanism.

Our work shows how numerical simulations can be used as a powerful tool to study different aspects of downstream structures. These results could be applied/contrasted to interpret the observational magnetosheath high-resolution data provided by different multi-spacecraft missions (e.g., Magnetospheric Multiscale (MMS), Cluster, and Time History of Events and Macroscale Interactions during Substorms (THEMIS)) and serve as motivation for future observational and theoretical studies. Future simulation work will include the analysis of VDFs, temperature anisotropy, and particle tracking inside and around simulation jets and

plasmoids as well as the study of these structures with fully 3D simulations.

We thank DGTIC-UNAM for the use of the supercomputer MIZTLI project LANCAD-UNAM-DGTIC-337. The authors acknowledge support from the Royal Society Newton International Exchange Scheme (Mexico) grant NI150051. L.P. thanks CONACYT grant 174700. X.B.C. thanks CONACyT grant 255203 and DGAPA project IN105218-3. D.B. thanks UK-STFC grant ST/P000622/1. D.T. thanks studentship by the Perren Fund of the University of London. P.K. thanks PAPIIT grant IA101118.

Appendix
Plasmoid Formation Mechanism: Additional Plots

Here we present more snapshots for the simulated output timesteps covering the formation of the studied plasmoid reported in Figure 3. The format of the figures is the same as the reported in Figure 5. Although here we only show the time interval $95 \leqslant \Omega_p\, t \leqslant 170$, the structure of the plasmoid, that is its internal magnetic rotation and increase in density, persist until $\Omega_p\, t \sim 200$ as well as its position at $x \sim 350\ d_i$.

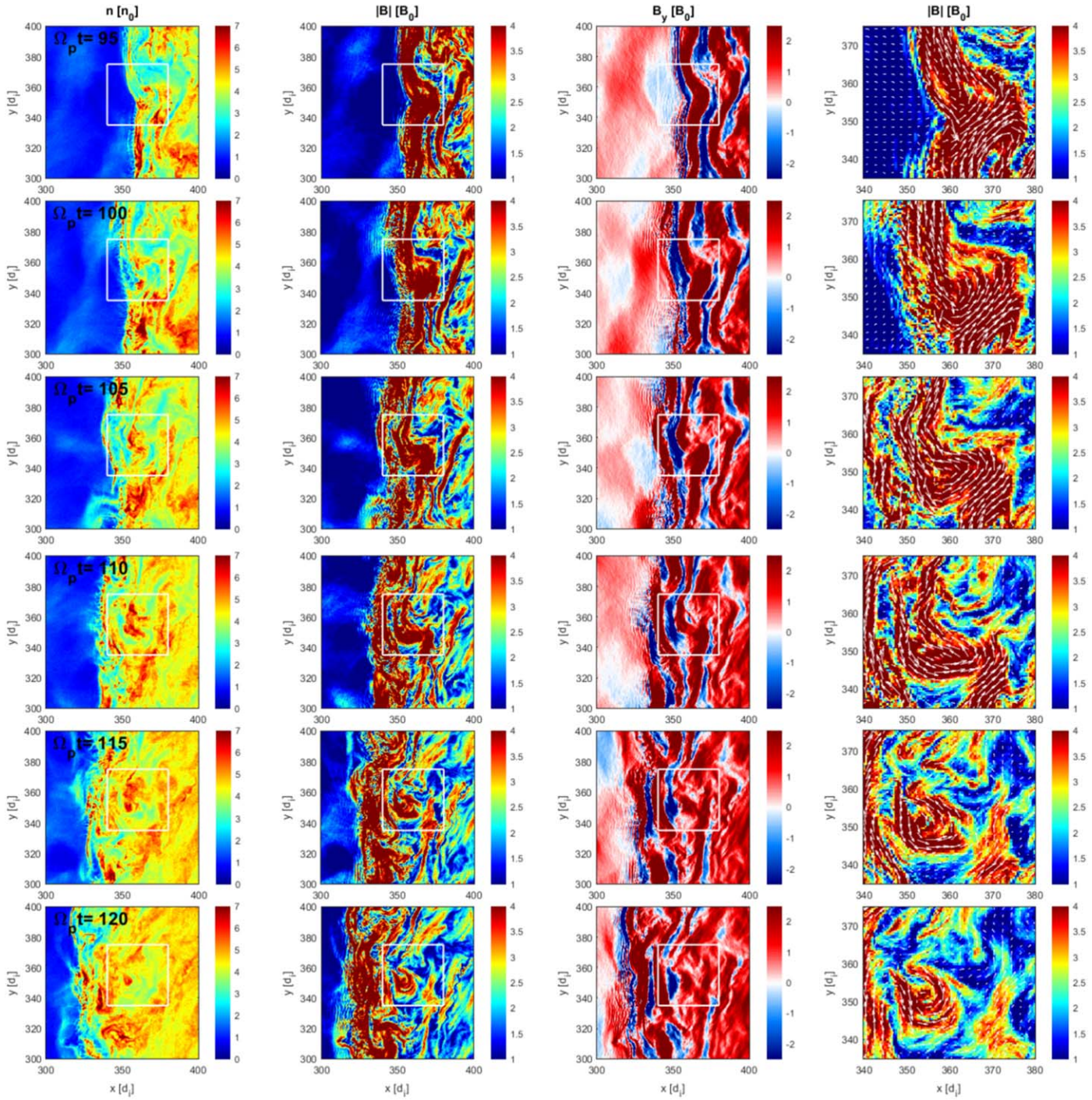

Figure A1. Isocolor snapshots corresponding (left to right) to ion density, B-field magnitude, B_y magnitude colored according its positive (fading red) or negative (fading blue) direction, and B-field magnitude (isocolors and vectors) in the region delimited by the white square. The timeline evolution (top to bottom) corresponds to $\Omega_p\, t = 95, 100, 105, 110, 115, 120$.

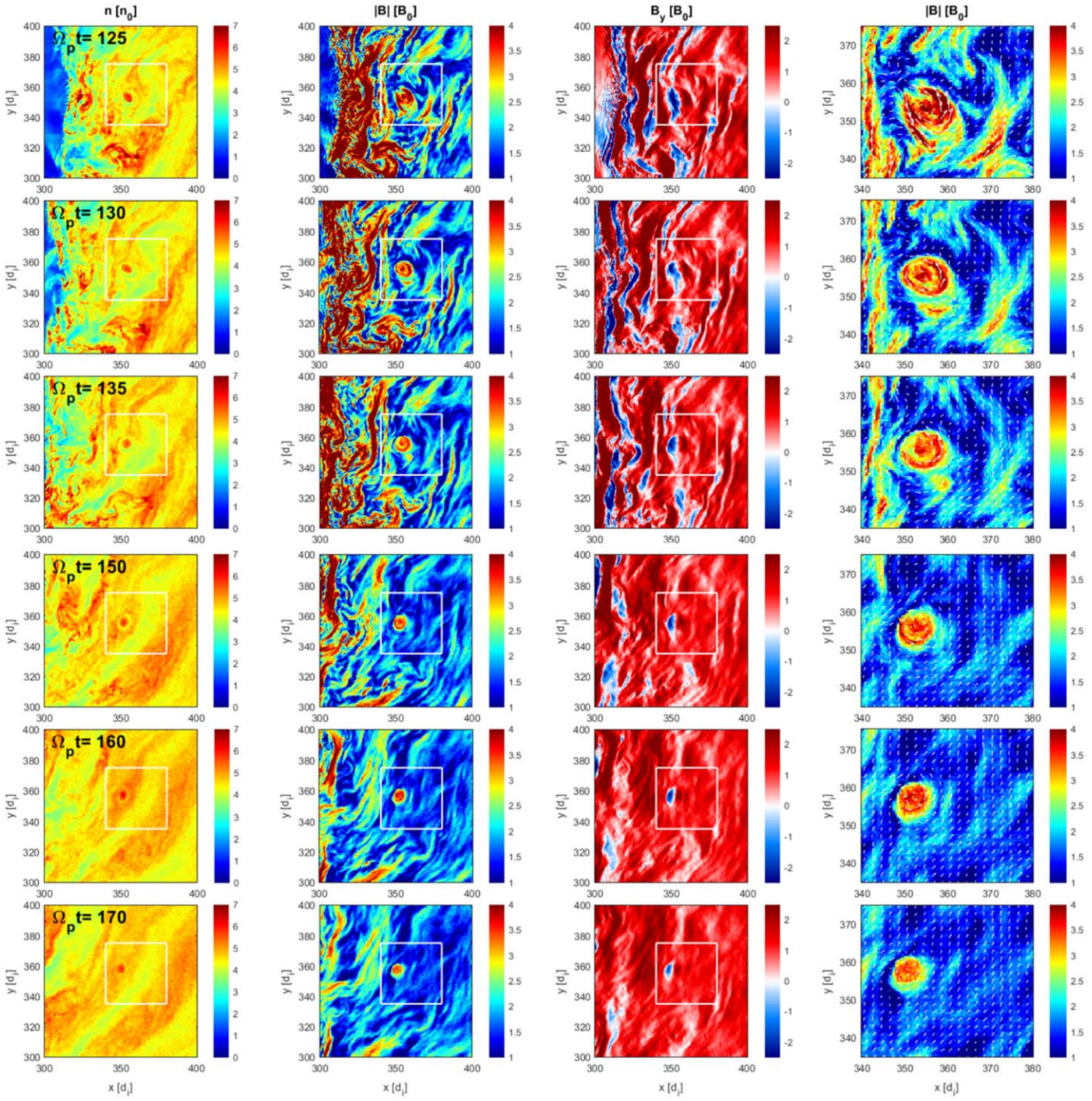

Figure A2. Same format as in Figure A1, now corresponding to $\Omega_p\ t = 125, 130, 135\ 150, 160, 170$.

ORCID iDs

Luis Preisser https://orcid.org/0000-0002-5636-2014
Xóchitl Blanco-Cano https://orcid.org/0000-0001-7171-0673
Primoz Kajdič https://orcid.org/0000-0002-0625-8892
David Burgess https://orcid.org/0000-0002-8175-9056
Domenico Trotta https://orcid.org/0000-0002-0608-8897

References

Amata, E., Savin, S. P., Ambrosino, D., et al. 2011, P&SS, 59, 482
Archer, M. O., & Horbury, T. S. 2013, AnGeo, 31, 319
Archer, M. O., Horbury, T. S., & Eastwood, J. P. 2012, JGR, 117, A05228
Blanco-Cano, X., Omidi, N., & Russell, C. T. 2009, JGRA, 114, A01216
Burgess, D. 1989, GeoRL, 16, 345
Burgess, D. 1995, AdSpR, 15, 159
Burgess, D. 1995, Collisionless Shocks (Cambridge: Cambridge University Press), 129
Burgess, D., & Scholer, M. 2015, Collisionless Shocks in Space Plasmas: Structure and Accelerated Particles, Cambridge Atmospheric and Space Science Series (Cambridge: Cambridge University Press)
Dubouloz, N., & Scholer, M. 1995, AdSpR, 15, 175
Eastwood, J. P., Balogh, A., Lucek, E. A., Mazelle, C., & Dandouras, I. 2005, JGRA, 110, A11219
Giacalone, J., Schwartz, S. J., & Burgess, D. 1993, GeoRL, 20, 149

Gingell, I., Schwartz, S. J., Burgess, D., et al. 2017, JGRA, 122, 11,003
Gunell, H., Stenberg Wieser, G., Mella, M., et al. 2014, AnGeo, 32, 991
Gutynska, O., Sibeck, D. G., & Omidi, N. 2015, JGRA, 120, 7687
Hao, Y., Gao, X., Lu, Q., et al. 2017, JGRA, 122, 6385
Hao, Y., Lembege, B., Lu, Q., & Guo, F. 2016a, JGRA, 121, 2080
Hao, Y., Lu, Q., Gao, X., & Wang, S. 2016b, ApJ, 823, 7
Hietala, H., Laitinen, T. V., Andréeová, K., et al. 2009, PhRvL, 103, 245001
Hietala, H., Partamies, N., Laitinen, T. V., et al. 2012, AnGeo, 30, 33
Hietala, H., & Plaschke, F. 2013, JGRA, 118, 7237
Hubert, D., & Harvey, C. C. 2000, GeoRL, 27, 3149
Karlsson, T., Brenning, N., Nilsson, H., et al. 2012, JGR, 117, A03227
Karlsson, T., Kullen, A., Liljeblad, E., et al. 2015, JGR, 120, 7390
Krauss-Varban, D., & Omidi, N. 1991, JGR, 96, 17715
Lucek, E. A., Constantinescu, D., Goldstein, M. L., et al. 2005, SSRv, 118, 95
Lucek, E. A., Horbury, T. S., Balogh, A., Dandouras, I., & Rème, H. 2004, JGRA, 109, A06207
Němeček, Z., Šafránková, J., Přech, L., et al. 1998, GeoRL, 25, 1273
Omidi, N., O'Farrell, A., & Krauss-Varban, D. 1994, AdSpR, 14, 45
Omidi, N., & Sibeck, D. G. 2007, JGRA, 112, A01203
Plaschke, F., Hietala, H., & Angelopoulos, V. 2013, AnGeo, 31, 1877
Plaschke, F., Hietala, H., Archer, M., et al. 2018, SSRv, 214, 81
Rakhmanova, L. S., Riazantseva, M. O., Zastenker, G. N., & Verigin, M. I. 2018, Ge&Ae, 58, 718
Savin, S., Amata, E., Budaev, V., et al. 2014, JETPL, 99, 16
Savin, S., Amata, E., Zelenyi, L., et al. 2012, AnGeo, 30, 1
Scholer, M., & Burgess, D. 1992, JGR, 97, 8319
Schwartz, S. J., & Burgess, D. 1991, GeoRL, 18, 373
Schwartz, S. J., Burgess, D., & Moses, J. J. 1996, AnGeo, 14, 1134
Schwartz, S. J., Burgess, D., Wilkinson, W. P., et al. 1992, JGR, 97, 4209
Shevyrev, N. N., & Zastenker, G. N. 2005, P&SS, 53, 95
Shevyrev, N. N., Zastenker, G. N., Nozdrachev, M. N., et al. 2003, AdSpR, 31, 1389
Su, Y., Lu, Q., Gao, X., Huang, C., & Wang, S. 2012, PhPl, 19, 092108
Tsubouchi, K., & Lembège, B. 2004, JGRA, 109, A02114
Tsurutani, B. T., & Stone, R. G. 1985, in Collisionless Shocks in the Heliosphere: Reviews of Current Research, Geophysical Monograph Ser, Vol. 35, ed. B. T. Tsurutani & R. G. Stone (Washington DC: AGU), 7
Yordanova, E., Vörös, Z., Varsani, A., et al. 2016, GeoRL, 43, 5969

Capítulo 4

Microestructura en la magnetofunda: Ondas modo mirror y jets durante campo magnético interplanetario sur.

4.1. Resumen del trabajo y metodología

En este trabajo se analizó un intervalo de $\sim$ 80 minutos observado por la misión Magnetospheric Multiscale Mission (MMS) (por sus siglas en inglés) en la región día de la magnetofunda terrestre de los cuales los primeros $\sim$ 46 minutos presentan un claro $B_z < 0$ en coordenadas GSE. Se estudiaron entonces tres estructuras identificadas como jets de acuerdo con el criterio basado en el incremento de la presión dinámica con respecto al plasma circundante (Plaschke et al., 2018). El análisis mostró que los tres jets poseen diferentes características por lo que se infiere que pueden tener diferente origen.

Dos de los jets (J1 y J2) presentan un claro incremento en la velocidad y un casi nulo aumento en la densidad. En contraste el tercer jet (J3) muestra un claro aumento en la densidad y un débil aumento en la velocidad. Además de esto, la duración de este último es aproximadamente siete veces más larga que la de J1 y J2. La firma magnética también es diferente: J3 coincide con una clara rotación (i.e. cambio de signo de negativo a positivo) en la componente B_z del campo magnético mientras que para J1 y J2 la magnitud de la

componente negativa B_z es la predominante. Las firmas de campo magnético y plasma para J3 se corresponden con una discontinuidad observada por otras naves localizadas en la región río arriba del choque de proa como fue demostrado en otro de los artículos (Trattner et al., 2020) que forma parte del mismo *GEM Special Issue* en el que se ha publicado nuestro trabajo. Las distribuciones iónicas dentro de los jets también resultaron tener diferentes características: J1 y J2 presentan un haz alineado secundario que no está presente en J3 cuyas distribuciones son más isotrópicas.

Con respecto a las diferencias en las fluctuaciones de campo magnético dentro y fuera de los jets, se logró determinar, a partir del análisis de Fourier, que la componente transversal, dentro de éstos, es la dominante, mientras que en las regiones inter-jet se localizaron al menos cinco zonas con ondas tipo mirror probando que los jets pueden coexistir con este tipo de ondas en la magnetofunda terrestre y debido a la naturaleza compresiva de estas últimas, ambas puedan interactuar con la magnetopausa.

4.2. Publicación en Journal of Geophysical Research (JGR) [Geospace Environment Modeling (GEM) Special Issue] (2020)

JGR Space Physics

RESEARCH ARTICLE
10.1029/2020JA027940

Special Section:
Results of the GEM Dayside Kinetics Southward IMF Challenge

Magnetosheath Microstructure: Mirror Mode Waves and Jets during Southward IP Magnetic Field

X. Blanco-Cano[1], L. Preisser[1], P. Kajdič[1], and D. Rojas-Castillo[1,2]

[1]Instituto de Geofísica, Universidad Nacional Autónoma de México, Mexico City, Mexico, [2]Space Research Institute, Austrian Academy of Sciences, Graz, Austria

Key Points:
- We study Earth's magnetosheath microstructure
- We show that structures identified as jets can be associated with different ion populations
- Magnetosheath jets and mirror mode can coexist deep in the magnetosheath

Correspondence to:
X. Blanco-Cano,
xbc@igeofisica.unam.mx

Citation:
Blanco-Cano, X., Preisser, L., Kajdič, P., & Rojas-Castillo, D. (2020). Magnetosheath microstructure: Mirror mode waves and jets during southward IP magnetic field. *Journal of Geophysical Research: Space Physics*, *125*, e2020JA027940. https://doi.org/10.1029/2020JA027940

Received 4 MAR 2020
Accepted 1 AUG 2020
Accepted article online 24 AUG 2020

Abstract In the Earth's magnetosheath plasma waves, nonlinear structures associated with characteristic ion populations can occur. Understanding the interaction of the solar wind with the magnetosphere requires a deeper knowledge of the underlying magnetosheath kinetic microstructure. We study a 45 min interval when the MMS spacecraft observed a southward magnetic field ($Bz < 0$ nT) in the dayside magnetosheath. Using magnetic field and plasma data, we analyze three transient dynamic pressure enhancements identified as magnetosheath jets. The characteristics of these jets are different, suggesting different origins. While two of them, called J1 and J2, exhibit large increment in velocity and almost no density increment, the third jet (J3) shows large density enhancements with almost no velocity increment. The duration of J3 is ~7 times longer than those of J1 and J2. J3 occurs at the region where the negative B_z becomes positive. Ion distributions inside the jets are different. J1 and J2 show a secondary field-aligned beam, which is not present in J3, suggesting that magnetic reconnection at the magnetopause is responsible for their formation. Distributions inside J3 are more isotropic. B field and plasma signatures inside J3 correspond to the crossing of a sector boundary, similar to the heliospheric plasma sheet, suggesting that J3 forms by the evolution and interaction of a solar wind structure with the bow shock and magnetosheath. Fluctuations inside J3 have larger transverse components, although they propagate at large angles to B. In contrast, waves in regions between the jets are compressive and are identified as mirror mode waves.

1. Introduction

The Earth's magnetosheath is the region downstream of the bow shock and contains solar wind (SW) plasma, which has been heated, decelerated, and compressed by the shock. It is permeated by a variety of ultralow frequency (ULF) waves ($f <$ proton gyrofrequency), nonlinear magnetic structures, and turbulence (Lucek et al., 2005). This means that this region is far from homogeneous, and its properties depend on the upstream conditions. It is this shocked SW, which eventually interacts with the magnetopause and can perturb and even enter into the magnetosphere. Therefore, understanding SW interaction with Earth's magnetic field requires a detailed knowledge of the magnetosheath plasma, including its kinetic microstructure.

The magnetosheath is magnetically connected to the bow shock, thereby the local shock properties have a large influence on the properties of the downstream plasma. Depending on the local angle θ_{Bn} between the local shock normal and the upstream magnetic field, the bow shock is classified as quasi-parallel ($Q_{\parallel}$) where $\theta_{Bn} < 45°$ and quasi-perpendicular ($Q_{\perp}$) where $\theta_{Bn} > 45°$ (Jones & Ellison, 1991). The existence of these two types of shocks results in different ways in which the plasma is processed by them. A characteristic B field/plasma extended transition develops at the $Q_{\parallel}$ shocks in contrast to a well-defined narrow transition for the shocks with the $Q_{\perp}$ geometry (Burgess & Scholer, 2015). The curved shape of planetary bow shocks (Schwartz, 1998) allows that their local shock normal direction and thus their geometry vary along the location on the shock surface.

Also, as a consequence of these geometric regimes at the $Q_{\parallel}$ bow shock, a portion of incident SW ions is reflected and escapes far upstream forming a region called the ion foreshock. The latter is filled by different backstreaming ion populations that can make the plasma unstable to a variety of wave modes (Eastwood et al., 2005; Hoppe et al., 1981). The most typical among them are the ULF waves with typical periods of 10–100 s that are carried earthward by the SW and steepen into shocklets and short-large amplitude magnetic structures (SLAMS, see Eastwood et al., 2005, and references therein). These can be transmitted

into the magnetosheath and probably account for the majority of the downstream fluctuations (Schwartz et al., 1996, and the references therein).

For the $Q_\perp$ bow shock region, the upstream side is much quieter (e.g., Omidi et al., 1994; Russell, 1985). This occurs because the ions and electrons that are reflected at such a shock cannot escape far upstream from it but are eventually transmitted downstream. There the initially reflected ions are preferentially heated in the direction perpendicular to the background magnetic field (Winske & Quest, 1988), so the corresponding downstream ion velocity distribution functions (VDFs) exhibit temperature anisotropies with $T_\perp/T_\parallel > 1$ (McKean et al., 1995; Sckopke et al., 1990). This anisotropy persists throughout the $Q_\perp$ magnetosheath, although it is larger near the shock as it has been observationally corroborated by, for example, Sckopke et al. (1990), and in recent hybrid simulations including He^{++} by Preisser et al. (2020). The anisotropy can lead to the growth of transverse ion cyclotron (IC) waves that propagate almost parallel to the background B field and the compressive, nonpropagating mirror mode waves (Gary, 1993). These two modes have been studied observationally by Anderson et al. (1991), Fuselier et al. (1991), and Anderson and Fuselier (1993), who showed that IC fluctuations arise preferentially in the low-β ($\beta \ll 1$) highly anisotropic plasmas, while mirror mode fluctuations are more likely to be observed in the higher-β ($\beta \geq 1$) plasmas even with smaller anisotropy. These results have been corroborated using linear-Vlasov theory under magnetosheath-like conditions including He^{++} particles (Gary et al., 1993). A typical observational signature of mirror mode structures is the anticorrelation between the magnetic field magnitude and density fluctuations (Enríquez-Rivera et al., 2013). Génot et al. (2009) determined the expression for mirror mode instability threshold to be $C_M = \beta_\perp(T_\perp/T_\parallel - 1) > 1$.

Another phenomenon studied in the magnetosheath is transient dynamic *pressure* (P_{dyn}) or ion flux enhancements called magnetosheath jets. Inside them the P_{dyn} may reach values above those in the upstream SW (Plaschke et al., 2018, and references therein). The P_{dyn} or ion flux enhancements can be due to enhancement of the dowstream SW speed, density, or a combination of both. Although there are several hypotheses on the origin of the magnetosheath jets, the most accepted ones are that the jets form at the shock due to its rippled surface (Hietala et al., 2009; Plaschke et al., 2013), due to the interaction of interplanetary magnetic field (IMF) discontinuities (Archer et al., 2012), hot flow anomalies (HFAs, Savin et al., 2012), or foreshock ULF waves (Omidi et al., 2016) with the bow shock, or that they may be SLAMS or SW plasmoids that have been transmitted into the magnetosheath (Karlsson et al., 2012, 2015, 2016).

Understanding jet properties and evolution is important because they can play a significant role in SW-magnetosphere-ionosphere interaction. Their increased momentum may cause deformations in the magnetosphere, which in turn can launch surface waves (Archer et al., 2012) or compressional waves (Plaschke et al., 2009). Ionospheric flow enhancements have been associated to jets (Hietala et al., 2012), and a recent study by Han et al. (2017) has suggested that a type of dayside auroras known as "throat" auroras may be caused by jet interaction with the magnetopause.

A number of past studies have determined some of the jets' properties, like their scale sizes being of the order of ~1 R_E (Archer et al., 2012; Plaschke et al., 2016), and their preferential occurrence downstream of the $Q_\parallel$ shock (Plaschke et al., 2016) and at low IMF cone angles (e.g., Vuorinen et al., 2019). However, we still know little about their microstructure, and how they interact with the surrounding plasma and different wave modes. In a recent study, Karlsson et al. (2018) showed that jets occurring at the transition region between the $Q_\parallel$ and $Q_\perp$ magnetosheath exhibit ion populations with VDFs similar to those observed in both $Q_\parallel$ and $Q_\perp$ magnetosheaths. These authors showed that jets can be associated with whistler, lower hybrid, and broadband electrostatic waves, as well as with compressive electromagnetic waves with periods of 10 s.

On the other hand, the SW is not a uniform flow of plasma and B field. Structures of different sizes, such as interplanetary coronal mass ejections (ICMEs) and magnetic clouds (MCs; Burlaga et al., 1981, 1982), small-scale flux ropes (Moldwin et al., 2000), small-scale flux rope-like structure (FRLS; Blanco-Cano et al., 2020), and smaller-scale rotational discontinuities may propagate in it. Extended periods of IMF with $B_z < 0$ may also occur; under such conditions, different phenomena such as magnetic reconnection can occur at the magnetopause (e.g., Cassak & Fuselier, 2016; Fuselier et al., 2019; Trattner et al., 2007, 2017), perturbing the geomagnetic field and magnetospheric currents due to the entry of SW particles.

The IMF orientation may be an important factor to consider during the magnetosheath jet interaction with the Earth's magnetic field. Magnetosheath jets have been shown to be often geoeffective

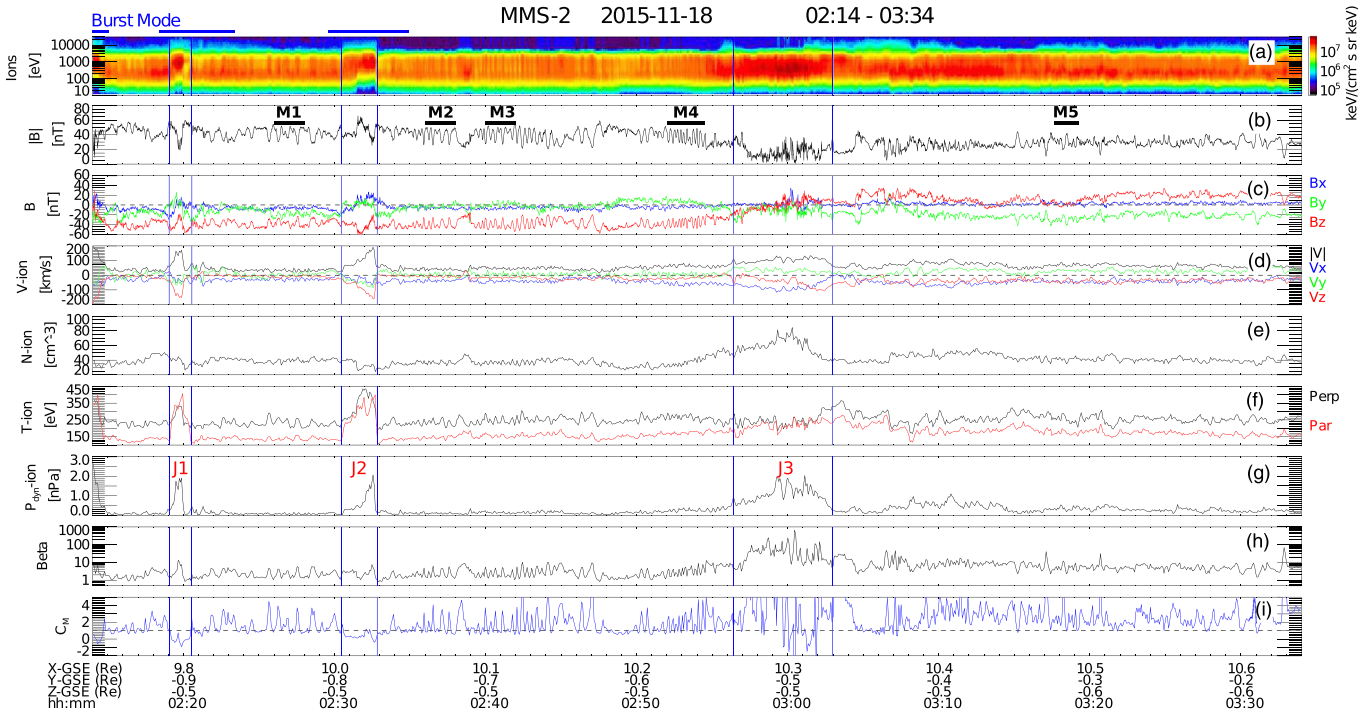

Figure 1. MMS-2 data on 18 November 2015 from 02:14 to 03:34 UT. Panels show ion energy spectra (a), magnetic field magnitude (b) and components (c), ion velocity magnitude and components (d), ion density (e), parallel and perpendicular ion temperature (f), dynamic pressure (g), plasma beta (h), and C_M the mirror mode instability threshold (i). The intervals during which the burst mode is available are marked by horizontal blue lines above the first panel. Mirror mode wave intervals are listed in Table 1 and are marked by horizontal black lines on panel (b). Jet intervals (J1, J2, and J3) are delimited by blue vertical lines.

(Plaschke et al., 2016), meaning that they impact the magnetosphere, they may cause magnetic reconnection at the magnetopause (Hietala et al., 2018), and may even penetrate across it (Dmitriev & Suvorova, 2012, 2015). It is thus important to study jets under different IMF orientations in order to understand better how they interact with our planet's environment.

In this work we investigate the microstructure of an extended period with southward B_z inside the magnetosheath region. The period under study was chosen by the GEM "Dayside Kinetic Processes in Global Solar Wind-Magnetosphere Interaction" focus group to examine different aspects of the SW interaction with Earth's magnetosphere under negative B_z. Our study focuses on mirror mode waves and magnetosheath jets. This paper is organized as follows: In section 2, the observations are described in a general way. In section 2.1, the wave analysis is presented. In section 2.2 the ion distributions on various locations are described. The discussion and conclusions are given in section 3.

2. Observations

We use data from the Magnetospheric Multiscale Mission (Burch et al., 2016) to study SW microstructure in the magnetosheath. Plasma data are from the Fast Plasma Instrument (Pollock et al., 2016) with a time resolution of 4.5 s and the magnetic field data with 16 samples per second from the Fluxgate Magnetometer (Russell et al., 2016).

On 18 November 2015 MMS crossed the magnetopause near the subsolar point at 02:11:30 UT (not shown) remaining in the dayside magnetosheath for several hours. An extended interval with southward B_z was observed during 02:14:00–02:59:46 UT. Figure 1 shows 80 min of plasma and magnetic field data during which MMS was located near the Sun-Earth line with its GSE coordinates varying from (9.74, −0.93, −0.46) to (10.67, −0.13, −0.58) in units of terrestrial radii (R_E). The panels in Figure 1 show, from top to bottom, omnidirectional ion energy spectra, magnetic field magnitude and components, velocity magnitude and components, ion density, ion temperature, ion dynamic pressure, plasma beta, and the mirror instability threshold ($C_M = \beta_\perp(T_\perp/T_{||} - 1)$; Génot et al., 2009; Hasegawa, 1969). The horizontal blue segments on top of the panels indicate periods during which the burst mode data are available. During the exhibited time

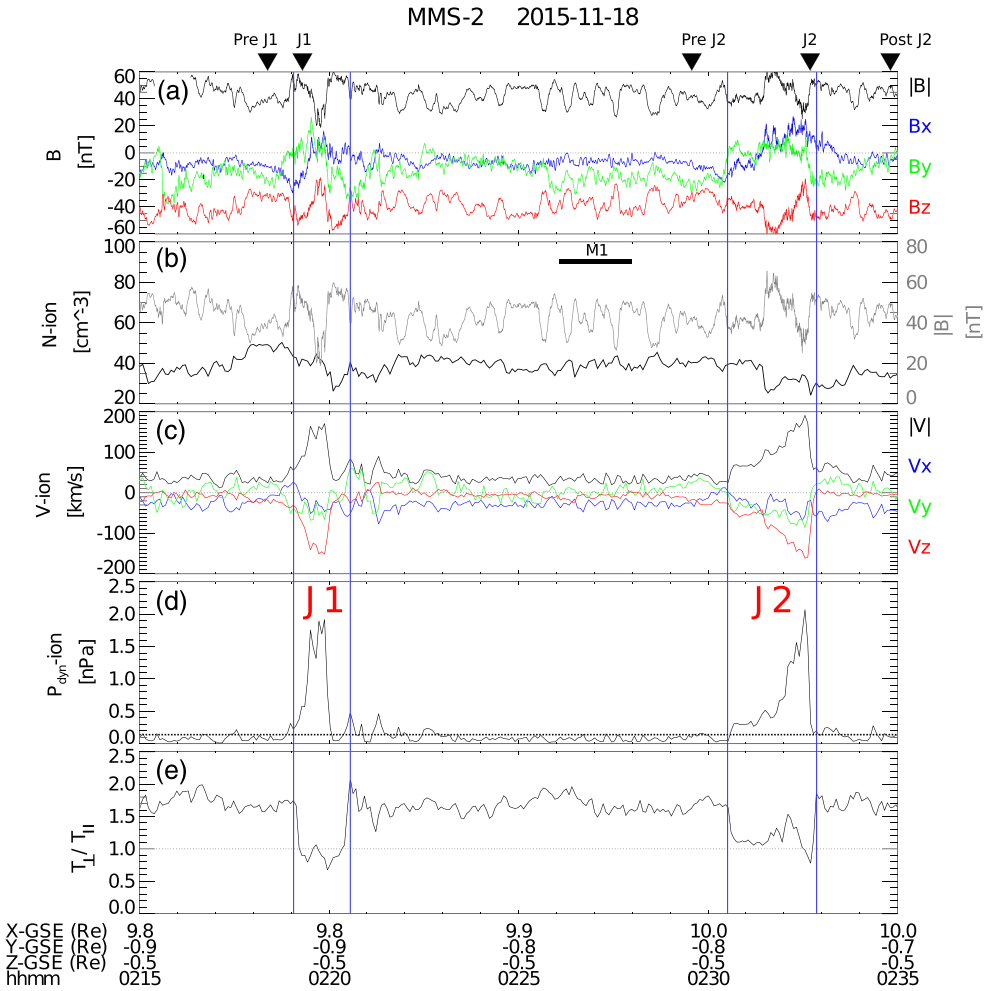

Figure 2. J1, J2, and their surroundings. Panels show magnetic field components and magnitude (a), ion density and magnetic field magnitude (b), velocity components and magnitude (c), dynamic pressure (d), and temperature anisotropy (e). The horizontal dotted line on panel (d) indicates the value of $2 < P_{dyn} >$. The times where the VDFs are calculated in Figures 5 and 6 are shown as triangle marks on the top. The time lapse of mirror mode waves—as listed in Table 1—is shown with a horizontal segment on panel (b). Blue lines mark sudden increments in temperature anisotropy around the maximum of P_{dyn}.

interval, the magnetosheath plasma is clearly not homogeneous showing interesting well-defined transients and waves.

In Figure 1 we identify three magnetosheath jets (marked as J1, J2, and J3) and various intervals with mirror mode waves (marked M1 to M5).

Several criteria have been used in the literature in order to identify magnetosheath jets (see Table 1 in Plaschke et al., 2018). Here we adopt the criteria of Archer and Horbury (2013), which states that the dynamic pressure inside the jets has to reach values of at least twice the background dynamic pressure. The horizontal dotted line in Figures 2 and 3 indicates the value of $2 < P_{dyn} >$. Due to the limited time interval that the MMS spacecraft spent on this occasion in the magnetosheath, we average the P_{dyn} *over* 2.5 min instead of the 20 min used by Archer and Horbury (2013).

The three jets propagate antisunward, with negative V_x. J1 and J2 have similar characteristics: large variations in V_z, a strong increment in V_{tot}, enhanced temperature, strong IMF rotation, and no increment in N. The increase in plasma velocity inside both jets is also seen in the ion spectrograms since the ion beams are shifted to higher energies.

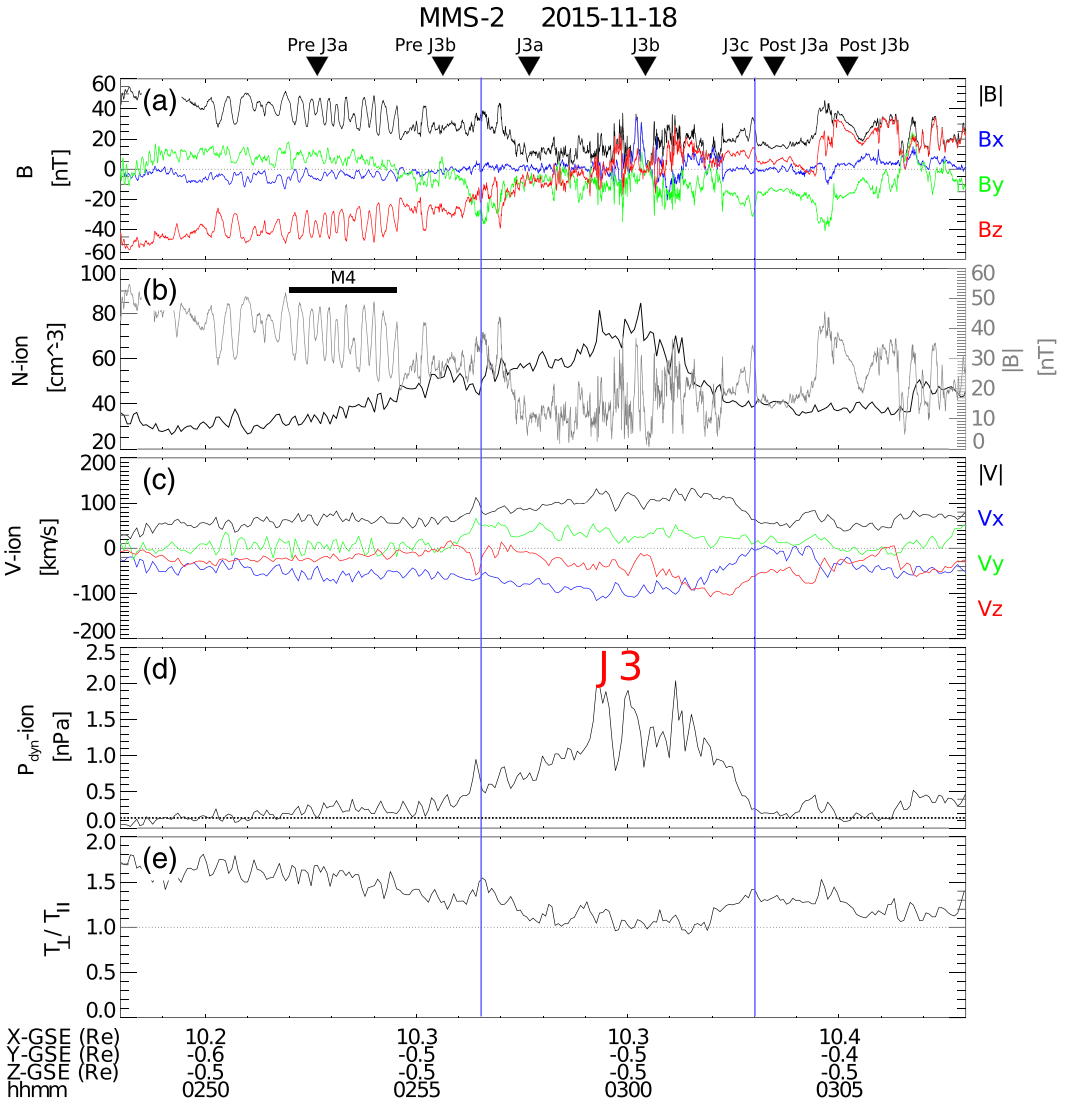

Figure 3. J3 and surrounding regions. The format of this figure as well as the *y* axis range of each panel is the same as in Figure 2.

We can see in Figure 1 that J3 occurs in the region where plasma and *B* field properties change. Before J3 the average *B* field magnitude is higher (~40 nT) and its orientation is mostly in the negative Z_{GSE} direction. After J3 the *B* field magnitude fluctuates around ~30 nT and it lies in the Y-Z_{GSE} plane. The plasma density changes from ~37 to ~40 cm^{-3} and the plasma speed from ~40 to ~65 km s^{-1}. The temperature anisotropy (Figures 2 and 3) shows background values (excluding J1 and J2 regions) of $T_{\perp}/T_{\parallel}\sim$ 1.7 until 02:51:11 UT. Inside J3 it diminishes and then it gradually rises to ~1.5. P_{dyn}, plasma β, and C_M parameter exhibit larger values after J3 than before.

The omnidirectional ion spectrogram in Figure 1 shows that from 02:33:30 to 02:57:00 UT the ion energies extended between 10 eV and ~6 keV. Afterward the maximum ion energies extend to higher values up to $\lesssim$20 keV. This is also observed at the rear part of the jet (~03:00:00 UT) and for ~8 min afterward. This broadening of the ion energy spectra has been associated to the spacecraft crossing from the $Q_{\perp}$ into the $Q_{\parallel}$ magnetosheath, that is, from the magnetosheath region that is magnetically connected to the $Q_{\perp}$ bow shock, into the region that is connected to the $Q_{\parallel}$ bow shock (Karlsson et al., 2018). As MMS was very near the subsolar magnetopause during the time of interest, we use the cone angle ($\theta_C = \arccos(|Bx|/|B|)$) as a proxy of the shock normal angle θ_{Bn} In most of the studied interval $\theta_C > 45°$ with only a short excursion to values <45° within J3. Thus, most of the time during the studied interval, MMS was in the $Q_{\perp}$ magnetosheath.

Note that in the case of J1 and J2 the broad spectra is associated *with* the increment in temperature, and not to the entrance into the $Q_{\parallel}$ magnetosheath. It is interesting to note that after J3 the energy spectra does not remain as broad as expected for the $Q_{\parallel}$ magnetosheath, and the temperature anisotropy values $T_{\perp}/T_{\parallel}$ are larger than 1, which is a characteristic of the $Q_{\perp}$ magnetosheath.

Inside J3 the temperature anisotropy values first decrease to $\gtrsim$1, indicating an almost isotropic ion distribution (see also Figure 3). This might be due to isotropisation of the plasma by the waves inside the jet. At the rear part of the jet the temperature anisotropy rises again with $T_{\perp} > T_{\parallel}$.

In contrast, inside J1 and J2 $T_{\perp}/T_{\parallel} \lesssim 1$. As we shall see later, this is not due to isotropic ion VDFs but occurs due to the fact that inside J1 and J2 two different ion populations coexist. The values of $T_{\perp}/T_{\parallel}$ in the plasma surrounding J1 and J2 are larger than 1, in agreement with the jets being immersed in a $Q_{\perp}$ magnetosheath.

As stated above, J1 and J2 are different from J3. Their duration in the data is 54 and 70 s, respectively. Through them the speed increases more than 100 km s^{-1}/s (see Figures 2 and 3), mostly due to enhanced V_z. In contrast, J3 lasts ~6 min and the velocity increment is ~50 km s^{-1}, with almost no change in the plasma flow direction. J1 and J2 show temperature enhancements within them, while the total temperature drops in J3 as can be observed in Figure 1f. These differences in jet characteristics suggest that J1 and J2 share a common origin, which seems to be different from the origin of J3.

It is important to mention that the B_z discontinuity detected by MMS was also observed upstream of the bow shock by Wind spacecraft as Kitamura et al. (2016) and Trattner et al. (2020) showed. As seen in Figure 2 of Kitamura et al. (2016), the change from negative B_z to positive values occurred through two discontinuities, and not in a smooth way as was observed by MMS in the magnetosheath. The transition from negative to positive B_z in the SW was accompanied by a small increment in the density that lasted around ~8 min. As we discuss below, it is highly probable (see Figure 3 in Trattner et al., 2020) that this small enhancement in plasma density is modified as the material crosses the shock and travels through the magnetosheath, leading to the large enhancement in density within J3 at the time of the smooth B_z rotation observed by MMS.

Figure 1 also shows the existence of anticorrelated plasma density and B field fluctuations, which we identify as mirror mode waves. The bottom panel shows that $C_M > 1$ throughout most of the analyzed interval, indicating that the plasma is mirror mode unstable (Enríquez-Rivera et al., 2013; Génot et al., 2009). Only inside J1 and J2, and in a portion of J3 C_M is less than 1, which indicates that plasma there is stable to the mirror mode instability. This is supported by the fact that the mirror mode waves are only observed in the interjet regions, but not inside the jets.

2.1. Mirror Mode Waves and Waves Inside Jets

Figures 2 and 3 show 20 min of data containing the jets. It is possible to see that the interjet regions are permeated by compressive waves, which show an anticorrelation between B and N. The shape of these waves is variable, with larger periods observed between J1 and J2, and shorter ones just before J3. The waves between J1 and J2 also show superposed higher frequency small amplitude fluctuations.

Figure 4 shows transverse and compressive power spectra of waves during six intervals. The top panels show B field spectra inside J1, J2, and J3. The bottom panels are for the interjet mirror mode intervals M1, M3, and M4. The compressive power is defined from the total power P_{tot}, which is the result of applying fast Fourier transform (FFT) to the total magnetic field $|B|$, while the transverse power is defined as $|P_x + P_y + P_z - P_{tot}|$, where P_x, P_y, and P_z are the powers of B_x, B_y, and B_z, respectively. It is possible to see that inside the jets the transverse component is the dominant one; however, the fluctuations also have a strong compressive component. In contrast, the waves in the interjet regions clearly contain more compressive power at low frequencies, $f < 10^{-1}$. For the waves observed during 02:26:00–02:28:00 (Figure 4d), there is also a peak in transverse power corresponding to very small amplitude waves that can be seen in Figure 2.

Mirror mode waves are easily identified in Figures 2b and 3b as they exhibit anticorrelated plasma density and B field fluctuations. Another strong indicator is the parameter C_M with values above 1. In order to strengthen our argument in favor of mirror mode waves, we perform minimum variance analysis (MVA; Sonnerup & Scheible, 1998) of various intervals and apply the criteria of Génot et al. (2001). According to these authors, mirror mode waves should satisfy $\lambda_{max} \gg \lambda_{int}$ and $\theta_{Boi} < 20°$, where λ_{max}, λ_{int}, and θ_{Boi} are the maximum and intermediate eigenvalues, and the angle between the ambient magnetic field and the maximum direction of fluctuation, respectively. Mirror mode waves are considered to be linearly polarized

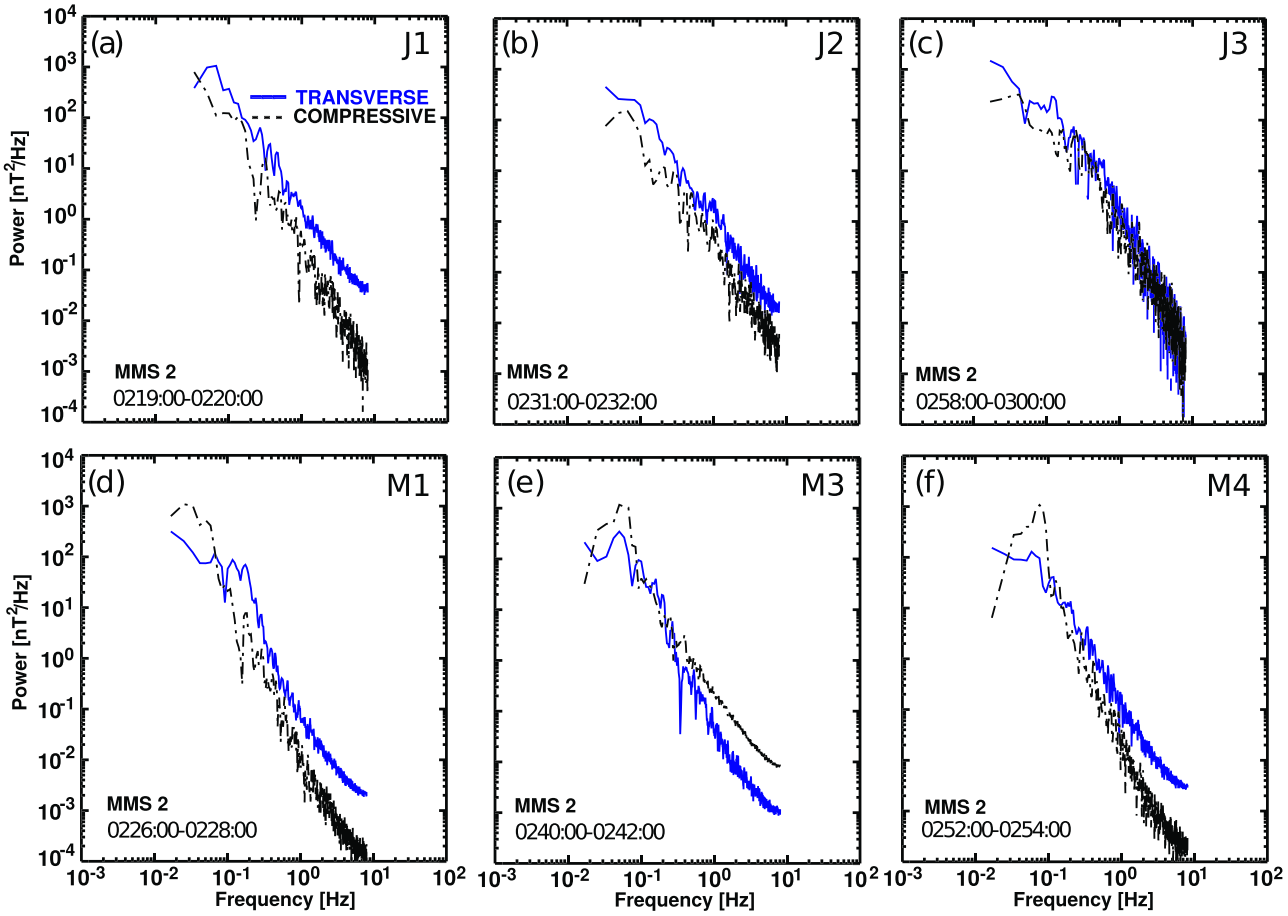

Figure 4. FFT spectra showing transverse (blue) and compressive (black dotted line) power of waves during six intervals. (a–c) Fluctuations inside J1, J2, and J3. (d–f) Intervals M1, M3, and M4 where mirror mode waves were identified.

when $\lambda_{int}/\lambda_{max} \leq 0.2$, and $\lambda_{min}/\lambda_{int} \geq 0.3$. If the last two criteria are not satisfied, mirror mode waves are considered to be elliptically polarized. Table 1 contains $\lambda_{int}/\lambda_{max}$, $\lambda_{min}/\lambda_{int}$, and θ_{Boi} for all of the analyzed intervals. We can see that all mirror mode waves here identified have elliptical polarization.

2.2. Ion Distributions

We use fast survey mode data from the Fast Plasma Instrument (FPI) to study the characteristics of ion distributions through the interval of study. Figure 5 shows distributions before, inside J1 and J2, and in the surrounding regions. The labels $V_{\perp 1}$, $V_{\perp 2}$, and $V_{\parallel}$ indicate directions perpendicular and parallel to the B field.

The VDFs in the interjet regions (02:18:24, 02:29:34, and 02:34:54) have a bi-Maxwellian shape with a $T_{\perp} > T_{\parallel}$, typical of the $Q_{\perp}$ magnetosheath. In contrast, the VDFs inside J1 and J2 show two populations, with the secondary (less dense) beam drifting along the B direction. As mentioned above, the temperature

Table 1
Mirror Mode Wave Intervals and Parameters

Label	Time interval	θ_{Boi}	$\lambda_{int}/\lambda_{max}$	$\lambda_{min}/\lambda_{int}$	Pol
M1	02:26:00–02:28:00	7	0.37	0.31	E
M2	02:36:00–02:38:00	6	0.23	0.30	E
M3	02:40:00–02:42:00	8	0.30	0.23	E
M4	02:52:00–02:54:30	7	0.19	0.21	E
M5	03:17:40–03:19:10	9	0.39	0.31	E

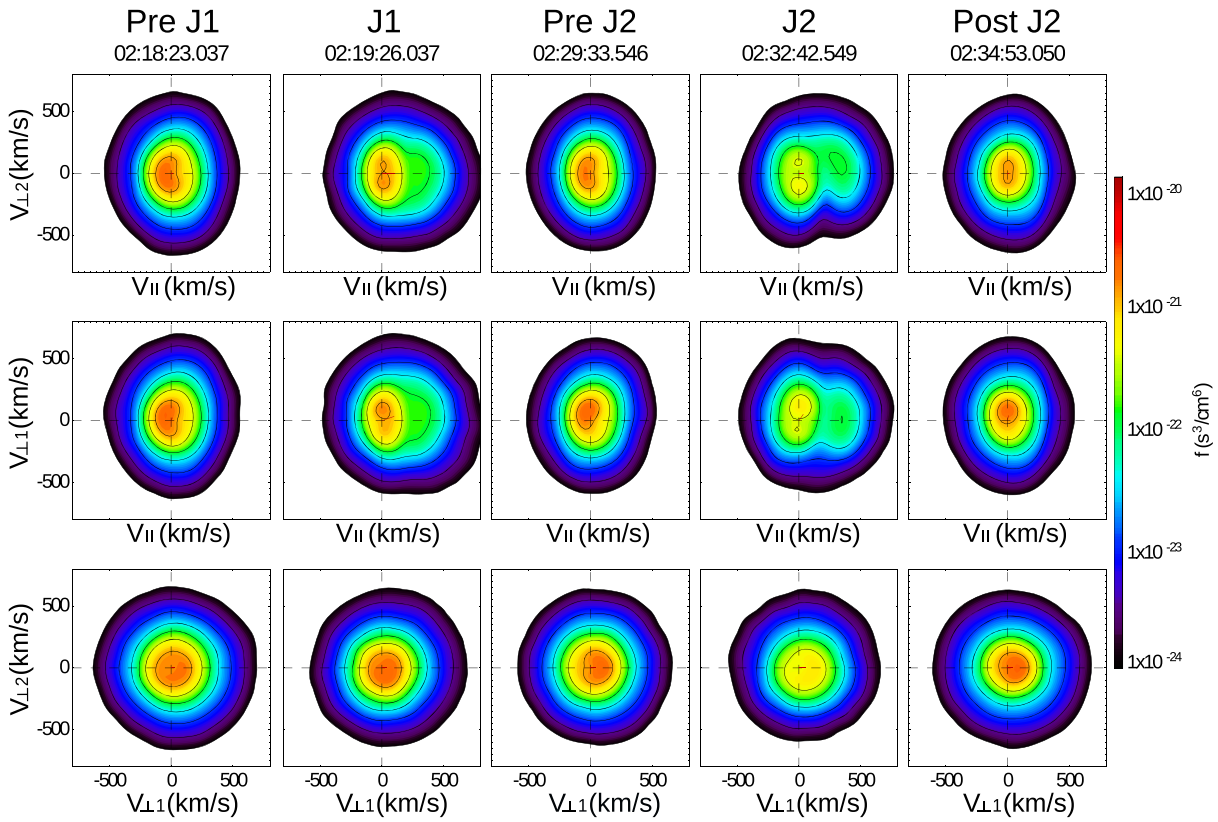

Figure 5. Ion distributions associated with J1, J2, and their surrounding regions. Distributions are given for three planes, where $V_{\perp 1}$, $V_{\perp 2}$, and $V_{\parallel}$ indicate directions perpendicular and parallel to the B field.

inside these jets increases. These plasma properties and distributions are very different from those reported by past authors (Archer & Horbury, 2013; Archer et al., 2012; Dmitriev & Suvorova, 2012; Karlsson et al., 2018; Plaschke et al., 2013; Shue et al., 2009) whose jets usually exhibit diminished temperature and $T_{\perp}/T_{\parallel}$ (although Karlsson et al., 2018, do report variations of the temperature anisotropy inside jets). The VDFs inside J1 and J2 are also different from those reported by Karlsson et al. (2018), which exhibit only one ion population.

Figure 6 shows distributions in a region before, inside, and after J3. The ion distribution at 02:52:39 UT is associated with mirror mode waves and exhibits $T_{\perp} > T_{\parallel}$. The ion distribution observed at 02:55:48 UT is not associated with mirror mode waves and is also less anisotropic. The latter can be clearly seen in Figure 3e, where the temperature anisotropy value changes from ∼1.6 at 02:52:39 UT to ∼1.4 at 02:55:49 UT. Two of the ion distributions inside the jet are isotropic (at 02:57:36 UT, 03:00:32 UT), while the VDF at the rear part of the jet at 03:02:42 UT shows anisotropic ion VDF. We can see in the Figure 3a that at the times of the first two VDFs inside J3 there are clear B field fluctuations, which are mostly transverse but also contain a strong compressive component and their frequencies range is between 0.05 and 0.10 Hz (see also Figure 4c). On the other hand at the rear part of J3 there are no such fluctuations. Finally, the VDF in the post-J3 region resembles those in the pre-J3 region.

3. Discussion and Conclusions

In this work we have shown that structures such as jets and mirror mode waves can coexist in the dayside magnetosheath. The jets were identified based on the dynamic pressure criteria of Archer and Horbury (2013). A particular characteristic of this interval is that B_z was negative and most of the sheath had a temperature anisotropy $T_{\perp}/T_{\parallel} > 1$ associated to the plasma downstream of the $Q_{\perp}$ shock. The microstructure of the studied region was complex; we investigated the properties of two jets due to velocity enhancements and one jet due to density increment.

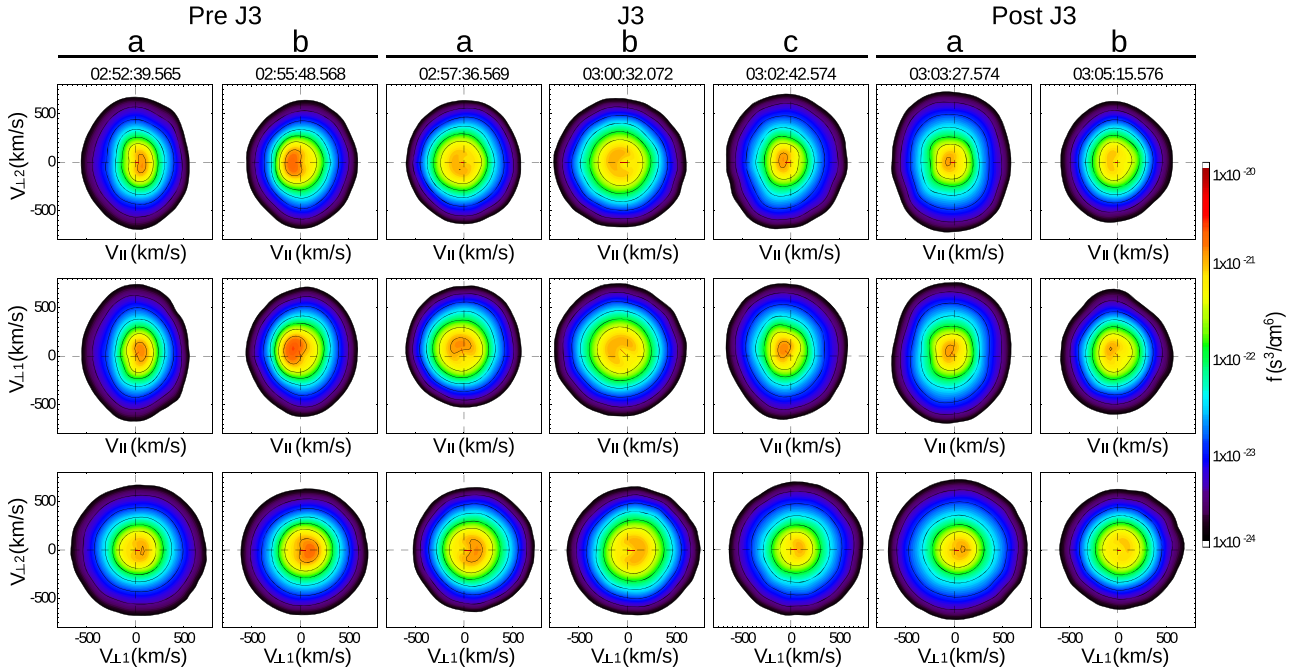

Figure 6. Ion distributions associated with J3 and their surrounding regions. In the same format as Figure 5.

We have shown that J1 and J2 have different characteristics in comparison with J3. In particular, the temperature increased inside J1 and J2, which is in contrast to other reported examples (Karlsson et al., 2018), where the decrement in temperature has been explained in terms of plasma that has been less processed than in their surroundings. J3 has a total temperature slightly above the background value.

Waves inside and outside of the jets were different; inside the jets waves are mainly transverse although they have a strong compressive component and propagate off angle. It is possible that inside J3 the waves arise from a combination of modes, as CB > 1, that is, above instability threshold. The waves inside J3 have frequencies $f \sim$ 0.05–0.10 Hz, which corresponds to periods 10–20 s in agreement with the results of Karlsson et al. (2018), who found waves inside jets with periods of 10 s. The interjet regions showed the existence of mirror mode waves, and no IC waves were identified. Because mirror mode waves are compressive structures, it is possible that their arrival to the magnetopause in combination with the jet arrival can have an impact on the magnetopause.

Our study reveals clear differences on VDF's in/out side jets. While in the interjet regions the VDFs are anisotropic with $T_\perp/T_\parallel > 1$, J1 and J2 show values close to 1 and even below 1. J3 shows more isotropic distributions, which could result from wave interaction. It remains as part of future work to study wave-particle interaction inside magnetosheath jets.

An interesting feature of J1 and J2 is that both exhibit a large, negative V_z (see Figure 2c). While in the past strong plasma flows at the magnetopause with large V_y and V_z components have been observed and explained in terms of magnetosheath jets being deflected at the distorted magnetopause by Shue et al. (2009), such deflections were also accompanied by strong variations of V_x, which remained the dominant velocity component. This is different than in the case of J1 and J2 where the dominant component is V_z, which means that these two jets traveled mainly in the southward direction.

One possibility for such a strong southward motion is that the two jets are a by-product of magnetic reconnection at the magnetopause, that is, formed by fast particle beams associated with reconnection. Kitamura et al. (2016) studied jets observed inside the magnetosphere for this same magnetopause crossing. These authors estimated that the distance from the separatrix to the center of the current sheet is about ~800 km. Thus, it is possible that MMS could go through the separatrix, where particles beams are expected to show higher parallel velocities as in the J1 and J2 cases. In a recent study, Trattner et al. (2020) identified J1 and J2 jets as signatures of the magnetopause boundary layer and mentioned that the southward accelerated ion

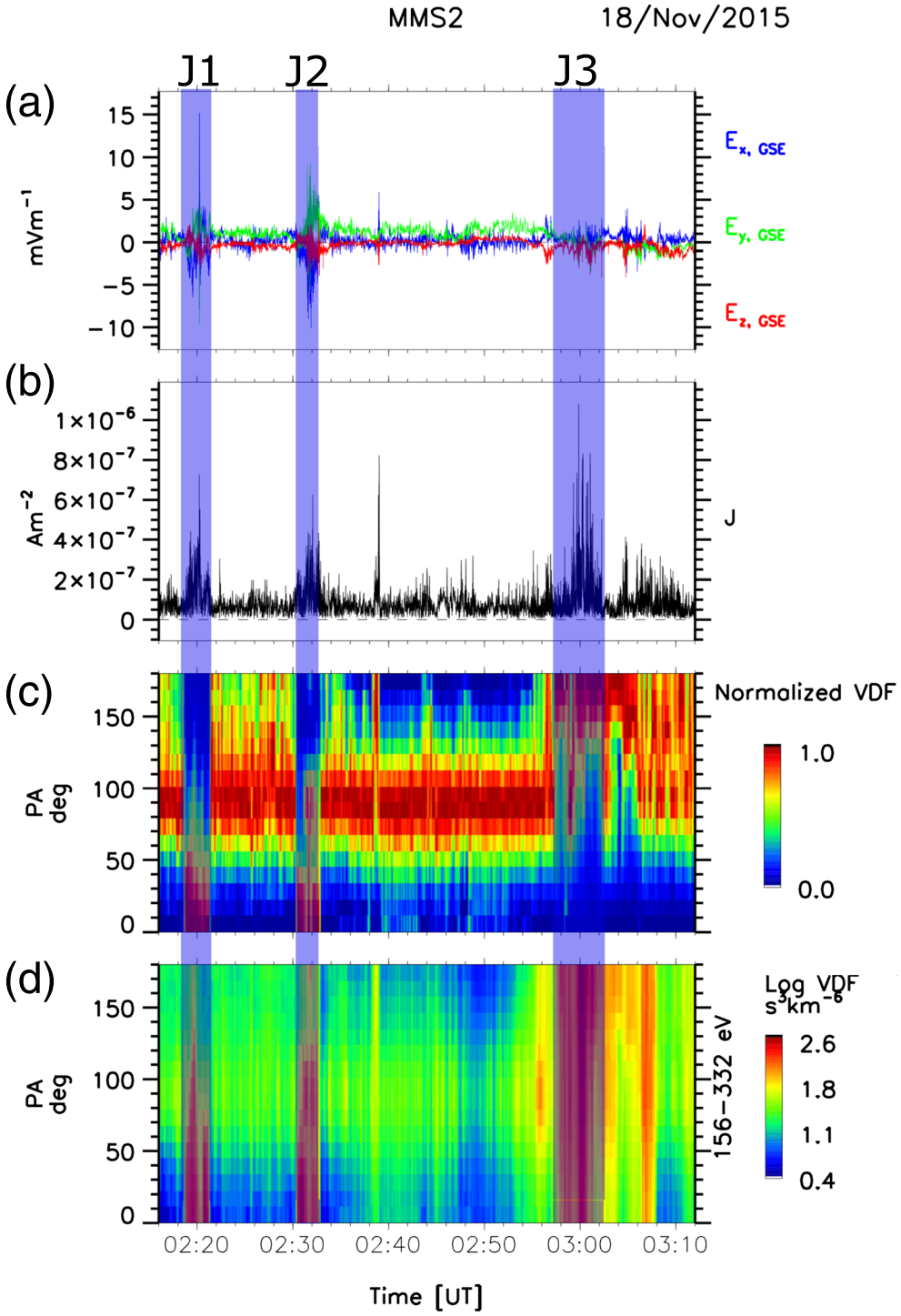

Figure 7. (a) Electric field components, (b) electric current calculated with the curlometer method (Robert et al., 1998), and (c and d) suprathermal electron pitch angle distributions, which are normalized on panel (c).

jets are evidence of an active X-line north of the MMS satellites. This would explain why we observe two ion populations: the more dense, unaccelerated population has its origin in the magnetosheath, while the accelerated, less dense population comes from the magnetosphere. Similar ion populations associated with magnetic reconnection at the magnetopause have been reported by, for example, Phan et al. (2013).

Lastly, we see that electron pitch angle distributions (PADs, Figures 7c and 7d) inside J1 and J2 are also very different from those in the ambient plasma. Figure 7c shows the distributions that are normalized to the largest value during each measurement. Compared with the rest of the magnetosheath, where electron PADs peak at pitch angles (PAs) ∼90°, inside J1 and J2 they are enhanced at all PAs and peak at PA $\lesssim$ 50°. Although these PADs extend up to 180°, they seem to have a secondary peak at PA ∼ 90°, which would indicate that two different electron populations coexist inside these two jets.

As mentioned above, the fast particles associated to J1 and J2 are observed away from their origin and the MMS spacecraft are located inside the magnetosheath before and after the jets. Hence, we do not observe all the reconnection jets signature, such as, for example, large IMF shear angles between the prejet and postjet regions and (anti)correlated B and V components (see, e.g., Gosling et al., 2005, for details on reconnection exhausts in the SW). Observational signatures in favor of the fast flows being associated to reconnection are the diminished B magnitude and increased temperature inside J1 and J2. The first is more clear in the case of J1, but it also occurs for J2 around the time of maximum P_{dyn} (see Figure 2). Different ion populations could be responsible for enhanced electric currents (see Figure 7b) and possibly also for strong electric field wave activity (Figure 7a) inside both jets. In all, J1 and J2 satisfy the definition of magnetosheath jets, with enhanced P_{dyn} above the stated threshold.

The J3 on the other hand shows a different set of features, such as relatively slow rotation of the B field (the shear angle between the pre-J3 and post-J3 IMF is ∼77°), more gradually varying B field magnitude, which is diminished inside the J3, enhanced ion density and β values (see Figures 1 and 3), and a single ion population (Figure 6). This together with its long duration (∼6 min) shows that magnetic reconnection could not have been a formation mechanism for J3. Rather, these signatures point to a crossing of a sector boundary (Ness & Wilcox, 1964; Wilcox & Ness, 1965), similar to the heliospheric plasma sheet (HPS; Burlaga et al., 1990; Winterhalter et al., 1994).

A crossing of HPS in the SW usually exhibits IMF inversions (e.g., Crooker et al., 2004), which means that the shear angle between pre-HPS and post-HPS are close to 180°. This is not the case for J3, but the same authors did show a few examples with smaller shear angles. It should be taken into account that J3 is observed deep inside the Earth's magnetosheath, so the observed HPS was processed by the Earth's bow shock and through the magnetosheath. Very similar signatures to those discussed here were reported by Wu et al. (2017) downstream of a fast, forward IP shock. These authors concluded that the HPS, which in the pristine SW already represents density enhancement, was further compressed by the IP shock so that an extremely strong density pulse with a peak value ∼94 cm^{-3} was formed. In our case the density peak is slightly smaller, reaching ∼85 cm^{-3}. We checked for possible HPS signatures at ACE and Wind. The two spacecraft observed the IMF rotation when B_z turned from negative to positive at ∼01:31 and ∼02:39 UT, respectively. Both spacecraft observed a much faster IMF rotation, of the order of ∼10 s, and no (ACE) or just a mild (Wind) density increase. However, at the time of observation ACE was located at (237, 32, 15) R_E and Wind at (215, −10, 6) R_E in GSE coordinates. Thus, they were not aligned with MMS and have probably missed the HPS or observed different parts of it.

Another characteristic feature of HPS crossing is that the PADs of suprathermal electrons (with energies of $\gtrsim$100 eV) abruptly change. Usually, PAs of these suprathermal strahl electrons change from 0° to 180° or vice versa (e.g., Crooker et al., 2004). Wu et al. (2017) report PA changes of ≥90°. Here we show PA distributions of electrons in energy range between 156 and 332 eV in Figures 7c and 7d. Figure 7c shows PA distributions, which are normalized to the largest value at each measurement. We can see that in the region between J2 and J3 the bulk of the electrons exhibit PA close to 90°, while inside J3 these are concentrated at PA $\lesssim$ 180°.

We should now put J1, J2, and J3 into a broader context. Many past works have studied jets by searching for signatures in a certain physical quantity, applying different identification criteria and proposing formation mechanisms (see Plaschke et al., 2018, for a review). However, we show here that different jets fulfilling the same identification criteria may have completely different origin. J1 and J2, for example, would have been detected by criteria involving the P_{dyn} (Amata et al., 2011; Archer & Horbury, 2013; Archer et al., 2012;

Hietala et al., 2012; Savin et al., 2008, 2014) or the ion flux (Němeček et al., 1998). However, the formation mechanisms proposed by some of the authors, such as formation at the rippled bow shock (Hietala et al., 2012), at IMF rotational discontinuities (Archer et al., 2012) or by transmission of SW plasmoids or foreshock SLAMS into the magnetosheath (Karlsson et al., 2012) do not apply to J1 and J2. On the other hand, J3 would have been picked up by all of the above criteria due to strong density enhancement and also by those used in Plaschke et al. (2013), Gunell et al. (2014), Karlsson et al. (2012, 2015, 2016), and Gutynska et al. (2015). As we mentioned earlier, J3 is associated to a field rotation so it is possible that it is related to the mechanism formation proposed by Archer et al. (2012).

In this work we have shown that a variety of plasma structures can be identified as jets using statistical identification criteria. However, the structures can be very different between them with extreme variations in their properties, which suggest different generation mechanisms. The case study approach used here is important to obtain detailed information of structures such as jets and mirror mode waves. In particular, the presented jet microstructure analysis proves the power of the VDFs and $T_{\perp}/T_{\parallel}$ as useful tools that should be adopted more often in addition to the preexisting toolkit with which jets have been studied and characterized. The changes on VDFs and temperature features could help to characterize jets formed by different mechanisms and/or determine their boundaries with a robust physical criterion. Future work is needed to provide more insight about the microphysics involved in the formation and evolution of magnetoheath jets and their impact on the SW magnetosphere interaction.

Data Availability Statement

Data access and some of the processing was done using SPEDAS V3.1, see Angelopoulos et al. (2019).

Acknowledgments
Authors acknowledge ClWeb (http://clweb.irap.omp.eu/) and MMS Science Data Center (https://lasp.colorado.edu/mms/sdc/public/) teams for easy access and visualization of the data. X. B. C. and P. K. acknowledge valuable discussions with members of the ISSI team 350 "Jets downstream of collisionless shocks" lead by F. Paschke and H. Hietala. P. K.'s work was supported by PAPIIT Grant IN105620. X. B. C.'s work was supported by UNAM DGAPA PAPIIT IN-105218-3 and Conacyt 255203 grants. L. P. thanks CONACYT becas nacionales 2015–2019 Grant 174700.

References

Amata, E., Savin, S. P., Ambrosino, D., Bogdanova, Y. V., Marcucci, M. F., Romanov, S., & Skalsky, A. (2011). High kinetic energy density jets in the Earth's magnetosheath: A case study. *Planetary and Space Science*, *59*, 482–494. https://doi.org/10.1016/j.pss.2010.07.021

Anderson, B. J., & Fuselier, S. A. (1993). Magnetic pulsations from 0.1 to 4.0 Hz and associated plasma properties in the Earth's subsolar magnetosheath and plasma depletion layer. *Journal of Geophysical Research*, *98*(A2), 1461–1480. https://doi.org/10.1029/92JA02197

Anderson, B. J., Fuselier, S. A., & Murr, D. (1991). Electromagnetic ion cyclotron waves observed in the plasma depletion layer. *Geophysical Journal Letters*, *18*(11), 1955–1958. https://doi.org/10.1029/91GL02238

Angelopoulos, V., Cruce, P., Drozdov, A., Grimes, E. W., Hatzigeorgiu, N., King, D. A., et al. (2019). The Space Physics Environment Data Analysis System (SPEDAS). *Space Science Reviews*, *215*(1), 9. https://doi.org/10.1007/s11214-018-0576-4

Archer, M. O., & Horbury, T. S. (2013). Magnetosheath dynamic pressure enhancements: Occurrence and typical properties. *Annales Geophysicae*, *31*(2), 319–331. https://doi.org/10.5194/angeo-31-319-2013

Archer, M. O., Horbury, T. S., & Eastwood, J. P. (2012). Magnetosheath pressure pulses: Generation downstream of the bow shock from solar wind discontinuities. *Journal of Geophysical Research*, *117*, A05228. https://doi.org/10.1029/2011JA017468

Blanco-Cano, X., Burgess, D., Sundberg, T., & Kajdi, P. (2020). Multispacecraft study of the interaction between an interplanetary shock and a solar wind flux rope. *Journal of Geophysical Research: Space Physics*, *124*, 9760–9773. https://doi.org/10.1029/2019JA026748

Burch, J. L., Moore, T. E., Torbert, R. B., & Giles, B. L. (2016). Magnetospheric multiscale overview and science objectives. *Space Science Reviews*, *199*(1-4), 5–21. https://doi.org/10.1007/s11214-015-0164-9

Burgess, D., & Scholer, M. (2015). Collisionless shocks in space plasmas.

Burlaga, L. F., Klein, L., Sheeley, J., Michels, D. J., Howard, R. A., Koomen, M. J., et al. (1982). A magnetic cloud and a coronal mass ejection. *Geophysical Journal Letters*, *9*(12), 1317–1320. https://doi.org/10.1029/GL009i012p01317

Burlaga, L. F., Mish, W. H., & Whang, Y. C. (1990). Coalescence of recurrent streams of different sizes and amplitudes. *Journal of Geophysical Research*, *95*, 4247–4255. https://doi.org/10.1029/JA095iA04p04247

Burlaga, L., Sittler, E., Mariani, F., & Schwenn, R. (1981). Magnetic loop behind an interplanetary shock: Voyager, Helios, and IMP 8 observations. *Journal of Geophysical Research*, *86*(A8), 6673–6684. https://doi.org/10.1029/JA086iA08p06673

Cassak, P. A., & Fuselier, S. A. (2016). Reconnection at Earth's Dayside Magnetopause. In W. Gonzalez & E. Parker (Eds.), *Magnetic reconnection: Concepts and applications, Astrophysics and Space Science Library* (Vol. 427, pp. 213). Cham, Switzerland: Springer International Publishing. https://doi.org/10.1007/978-3-319-26432-56

Crooker, N. U., Huang, C. L., Lamassa, S. M., Larson, D. E., Kahler, S. W., & Spence, H. E. (2004). Heliospheric plasma sheets. *Journal of Geophysical Research*, *109*, A03107. https://doi.org/10.1029/2003JA010170

Dmitriev, A. V., & Suvorova, A. V. (2012). Traveling magnetopause distortion related to a large-scale magnetosheath plasma jet: THEMIS and ground-based observations. *Journal of Geophysical Research*, *117*, A08217. https://doi.org/10.1029/2011JA016861

Dmitriev, A. V., & Suvorova, A. V. (2015). Large-scale jets in the magnetosheath and plasma penetration across the magnetopause: THEMIS observations. *Journal of Geophysical Research: Space Physics*, *120*, 4423–4437. https://doi.org/10.1002/2014JA020953

Eastwood, J. P., Balogh, A., Lucek, E. A., Mazelle, C., & Dandouras, I. (2005). Quasi-monochromatic ulf foreshock waves as observed by the four-spacecraft cluster mission: 1. Statistical properties. *Journal of Geophysical Research*, *110*, A11219. https://doi.org/10.1029/2004JA010617

Enríquez-Rivera, O., Blanco-Cano, X., Russell, C. T., Jian, L. K., Luhmann, J. G., Simunac, K. D. C., & Galvin, A. B. (2013). Mirror-mode storms inside stream interaction regions and in the ambient solar wind: A kinetic study. *Journal of Geophysical Research: Space Physics*, *118*, 17–28. https://doi.org/10.1029/2012JA018233

Fuselier, S. A., Klumpar, D. M., Shelley, E. G., Anderson, B. J., & Coates, A. J. (1991). He^{2+} and H^{+} dynamics in the subsolar magnetosheath and plasma depletion layer. *Journal of Geophysical Research*, *96*(A12), 21,095–21,104. https://doi.org/10.1029/91JA02145

Fuselier, S. A., Trattner, K. J., Petrinec, S. M., Pritchard, K. R., Burch, J. L., Cassak, P. A., et al. (2019). Stationarity of the reconnection X-Line at Earth's magnetopause for southward IMF. *Journal of Geophysical Research: Space Physics*, *124*, 8524–8534. https://doi.org/10.1029/2019JA027143

Gary, S. P. (1993). Theory of space plasma microinstabilities.

Gary, S. P., Fuselier, S. A., & Anderson, B. J. (1993). Ion anisotropy instabilities in the magnetosheath. *Journal of Geophysical Research*, *98*(A2), 1481–1488.

Génot, V., Budnik, E., Hellinger, P., Passot, T., Belmont, G., Trávníček, P. M., et al. (2009). Mirror structures above and below the linear instability threshold: Cluster observations, fluid model and hybrid simulations. *Annales Geophysicae*, *27*(2), 601–615. https://doi.org/10.5194/angeo-27-601-2009

Génot, V., Schwartz, S. J., Mazelle, C., Balikhin, M., Dunlop, M., & Bauer, T. M. (2001). Kinetic study of the mirror mode. *Journal of Geophysical Research*, *106*(A10), 21,611–21,622. https://doi.org/10.1029/2000JA000457

Gosling, J. T., Skoug, R. M., McComas, D. J., & Smith, C. W. (2005). Direct evidence for magnetic reconnection in the solar wind near 1 AU. *Journal of Geophysical Research*, *110*, A01107. https://doi.org/10.1029/2004JA010809

Gunell, H., Stenberg Wieser, G., Mella, M., Maggiolo, R., Nilsson, H., Darrouzet, F., et al. (2014). Waves in high-speed plasmoids in the magnetosheath and at the magnetopause. *Annales Geophysicae*, *32*(8), 991–1009. https://doi.org/10.5194/angeo-32-991-2014

Gutynska, O., Sibeck, D. G., & Omidi, N. (2015). Magnetosheath plasma structures and their relation to foreshock processes. *Journal of Geophysical Research: Space Physics*, *120*, 7687–7697. https://doi.org/10.1002/2014JA020880

Han, D. S., Hietala, H., Chen, X. C., Nishimura, Y., Lyons, L. R., Liu, J. J., et al. (2017). Observational properties of dayside throat aurora and implications on the possible generation mechanisms. *Journal of Geophysical Research: Space Physics*, *122*, 1853–1870. https://doi.org/10.1002/2016JA023394

Hasegawa, A. (1969). Drift mirror instability in the magnetosphere. *The Physics of Fluids*, *12*(12), 2642–2650. https://doi.org/10.1063/1.1692407

Hietala, H., Laitinen, T. V., Andréeová, K., Vainio, R., Vaivads, A., Palmroth, M., et al. (2009). Supermagnetosonic Jets behind a Collisionless Quasiparallel Shock. *Physical Review Letters*, *103*(24), 245001. https://doi.org/10.1103/PhysRevLett.103.245001

Hietala, H., Partamies, N., Laitinen, T. V., Clausen, L. B. N., Facskó, G., Vaivads, A., et al. (2012). Supermagnetosonic subsolar magnetosheath jets and their effects: From the solar wind to the ionospheric convection. *Annales Geophysicae*, *30*(1), 33–48. https://doi.org/10.5194/angeo-30-33-2012

Hietala, H., Phan, T. D., Angelopoulos, V., Oieroset, M., Archer, M. O., Karlsson, T., & Plaschke, F. (2018). In situ observations of a magnetosheath high-speed jet triggering magnetopause reconnection. *Geophysical Research Letters*, *45*, 1732–1740. https://doi.org/10.1002/2017GL076525

Hoppe, M. M., Russell, C. T., Frank, L. A., Eastman, T. E., & Greenstadt, E. W. (1981). Upstream hydromagnetic waves and their association with backstreaming ion populations: ISEE 1 and 2 observations. *Journal of Geophysical Research*, *86*(A6), 4471–4492. https://doi.org/10.1029/JA086iA06p04471

Jones, F. C., & Ellison, D. C. (1991). The plasma physics of shock acceleration. *Space Science Reviews*, *58*(1), 259–346. https://doi.org/10.1007/BF01206003

Karlsson, T., Brenning, N., Nilsson, H., Trotignon, J. G., Vallières, X., & Facsko, G. (2012). Localized density enhancements in the magnetosheath: Three-dimensional morphology and possible importance for impulsive penetration. *Journal of Geophysical Research*, *117*, A03227. https://doi.org/10.1029/2011JA017059

Karlsson, T., Kullen, A., Liljeblad, E., Brenning, N., Nilsson, H., Gunell, H., & Hamrin, M. (2015). On the origin of magnetosheath plasmoids and their relation to magnetosheath jets. *Journal of Geophysical Research: Space Physics*, *120*, 7390–7403. https://doi.org/10.1002/2015JA021487

Karlsson, T., Liljeblad, E., Kullen, A., Raines, J. M., Slavin, J. A., & Sundberg, T. (2016). Isolated magnetic field structures in Mercury's magnetosheath as possible analogues for terrestrial magnetosheath plasmoids and jets. *Planetary and Space Science*, *129*, 61–73. https://doi.org/10.1016/j.pss.2016.06.002

Karlsson, T., Plaschke, F., Hietala, H., Archer, M., Blanco-Cano, X., Kajdič, P., et al. (2018). Investigating the anatomy of magnetosheath jets—MMS observations. *Annales Geophysicae*, *36*(2), 655–677. https://doi.org/10.5194/angeo-36-655-2018

Kitamura, N., Hasegawa, H., Saito, Y., Shinohara, I., Yokota, S., Nagai, T., et al. (2016). Shift of the magnetopause reconnection line to the winter hemisphere under southward IMF conditions: Geotail and MMS observations. *Geophysical Research Letters*, *43*, 5581–5588. https://doi.org/10.1002/2016GL069095

Lucek, E. A., Constantinescu, D., Goldstein, M. L., Pickett, J., Pinçon, J. L., Sahraoui, F., et al. (2005). The magnetosheath. *Space Science Reviews*, *118*(1-4), 95–152. https://doi.org/10.1007/s11214-005-3825-2

McKean, M. E., Omidi, N., & Krauss-Varban, D. (1995). Wave and ion evolution downstream of quasi-perpendicular bow shocks. *Journal of Geophysical Research*, *100*(A3), 3427–3438. https://doi.org/10.1029/94JA02529

Moldwin, M. B., Ford, S., Lepping, R., Slavin, J., & Szabo, A. (2000). Small-scale magnetic flux ropes in the solar wind. *Geophysical Research Letters*, *27*(1), 57–60. https://doi.org/10.1029/1999GL010724

Němeček, Z., Šafránková, J., Přech, L., Sibeck, D. G., Kokubun, S., & Mukai, T. (1998). Transient flux enhancements in the magnetosheath. *Geophysical Research Letters*, *25*, 1273–1276. https://doi.org/10.1029/98GL50873

Ness, N. F., & Wilcox, J. M. (1964). Solar origin of the interplanetary magnetic field. *Physical Review Letters*, *13*, 461–464. https://doi.org/10.1103/PhysRevLett.13.461

Omidi, N., Berchem, J., Sibeck, D., & Zhang, H. (2016). Impacts of spontaneous hot flow anomalies on the magnetosheath and magnetopause. *Journal of Geophysical Research: Space Physics*, *121*, 3155–3169. https://doi.org/10.1002/2015JA022170

Omidi, N., O'Farrell, A., & Krauss-Varban, D. (1994). Sources of magnetosheath waves and turbulence. *Advances in Space Research*, *14*(7), 45–54. https://doi.org/10.1016/0273-1177(94)90047-7

Phan, T. D., Paschmann, G., Gosling, J. T., Oieroset, M., Fujimoto, M., Drake, J. F., & Angelopoulos, V. (2013). The dependence of magnetic reconnection on plasma β and magnetic shear: Evidence from magnetopause observations. *Geophysical Research Letters*, *40*, 11–16. https://doi.org/10.1029/2012GL054528

Plaschke, F., Glassmeier, K. H., Sibeck, D. G., Auster, H. U., Constantinescu, O. D., Angelopoulos, V., & Magnes, W. (2009). Magnetopause surface oscillation frequencies at different solar wind conditions. *Annales Geophysicae*, *27*(12), 4521–4532. https://doi.org/10.5194/angeo-27-4521-2009

Plaschke, F., Hietala, H., & Angelopoulos, V. (2013). Anti-sunward high-speed jets in the subsolar magnetosheath. *Annales Geophysicae*, *31*(10), 1877–1889. https://doi.org/10.5194/angeo-31-1877-2013

Plaschke, F., Hietala, H., Angelopoulos, V., & Nakamura, R. (2016). Geoeffective jets impacting the magnetopause are very common. *Journal of Geophysical Research: Space Physics*, *121*, 3240–3253. https://doi.org/10.1002/2016JA022534

Plaschke, F., Hietala, H., Archer, M., Blanco-Cano, X., Kajdič, P., Karlsson, T., et al. (2018). Jets downstream of collisionless shocks. *Space Science Reviews*, *214*(5), 81. https://doi.org/10.1007/s11214-018-0516-3

Pollock, C., Moore, T., Jacques, A., Burch, J., Gliese, U., Saito, Y., et al. (2016). Fast plasma investigation for magnetospheric multiscale. *Space Science Reviews*, *199*(1-4), 331–406. https://doi.org/10.1007/s11214-016-0245-4

Preisser, L., Blanco-Cano, X., Trotta, D., Burgess, D., & Kajdič, P. (2020). Influence of He^{++} and shock geometry on interplanetary shocks in the solar wind: 2D hybrid simulations. *Journal of Geophysical Research: Space Physics*, *125*, e27442. https://doi.org/10.1029/2019JA027442

Robert, P., Dunlop, M. W., Roux, A., & Chanteur, G. (1998). Accuracy of current density determination. *ISSI Scientific Reports Series*, *1*, 395–418.

Russell, C. T. (1985). Planetary bow shocks. *Washington DC American Geophysical Union Geophysical Monograph Series*, *35*, 109–130. https://doi.org/10.1029/GM035p0109

Russell, C. T., Anderson, B. J., Baumjohann, W., Bromund, K. R., Dearborn, D., Fischer, D., et al. (2016). The Magnetospheric Multiscale magnetometers. *Space Science Reviews*, *199*(1-4), 189–256. https://doi.org/10.1007/s11214-014-0057-3

Savin, S., Amata, E., Budaev, V., Zelenyi, L., Kronberg, E. A., Buechner, J., et al. (2014). On nonlinear cascades and resonances in the outer magnetosphere. *Journal of Experimental and Theoretical Physics Letters*, *99*, 16–21. https://doi.org/10.1134/S002136401401010X

Savin, S., Amata, E., Zelenyi, L., Budaev, V., Consolini, G., Treumann, R., et al. (2008). High energy jets in the Earth's magnetosheath: Implications for plasma dynamics and anomalous transport. *Journal of Experimental and Theoretical Physics Letter*, *87*, 593–599. https://doi.org/10.1134/S0021364008110015

Savin, S., Amata, E., Zelenyi, L., Lutsenko, V., Safrankova, J., Nemecek, Z., et al. (2012). Super fast plasma streams as drivers of transient and anomalous magnetospheric dynamics. *Annales Geophysicae*, *30*(1), 1–7. https://doi.org/10.5194/angeo-30-1-2012

Schwartz, S. J. (1998). Shock and discontinuity normals, Mach numbers, and related parameters. *ISSI Scientific Reports Series*, *1*, 249–270.

Schwartz, S. J., Burgess, D., & Moses, J. J. (1996). Low-frequency waves in the Earthś magnetosheath: Present status. *Annales Geophysicae*, *14*(11), 1134–1150. https://doi.org/10.1007/s00585-996-1134-z

Sckopke, N., Paschmann, G., Brinca, A. L., Carlson, C. W., & Luehr, H. (1990). Ion thermalization in quasi-perpendicular shocks involving reflected ions. *Journal of Geophysical Research*, *95*(A5), 6337–6352. https://doi.org/10.1029/JA095iA05p06337

Shue, J. H., Chao, J. K., Song, P., McFadden, J. P., Suvorova, A., Angelopoulos, V., et al. (2009). Anomalous magnetosheath flows and distorted subsolar magnetopause for radial interplanetary magnetic fields. *Geophysical Research Letters*, *36*, L18112. https://doi.org/10.1029/2009GL039842

Sonnerup, B. U. O., & Scheible, M. (1998). Minimum and maximum variance analysis. In G. Paschmann & P. Daly (Eds.), *Analysis methods for multi-spacecraft data* (pp. 185–220). Noordwijk: ESA.

Trattner, K. J., Burch, J. L., Ergun, R., Eriksson, S., Fuselier, S. A., Giles, B. L., et al. (2017). The MMS dayside magnetic reconnection locations during Phase 1 and their relation to the predictions of the maximum magnetic shear model. *Journal of Geophysical Research: Space Physics*, *122*, 11,991–12,005. https://doi.org/10.1002/2017JA024488

Trattner, K. J., Burch, J. L., Fuselier, S. A., Petrinec, S. M., & Vines, S. K. (2020). The November 18 2015 magnetopause crossing: The GEM dayside kinetic challenge event observed by MMS/HPCA. *Journal of Geophysical Research: Space Physics*, *125*, e2019JA027617. https://doi.org/10.1029/2019JA027617

Trattner, K. J., Mulcock, J. S., Petrinec, S. M., & Fuselier, S. A. (2007). Location of the reconnection line at the magnetopause during southward IMF conditions. *Geophysical Journal Letters*, *34*, L03108. https://doi.org/10.1029/2006GL028397

Vuorinen, L., Hietala, H., & Plaschke, F. (2019). Jets in the magnetosheath: IMF control of where they occur. *Annales Geophysicae*, *37*(4), 689–697. https://doi.org/10.5194/angeo-37-689-2019

Wilcox, J. M., & Ness, N. F. (1965). A Quasi-stationary corotating structure in the interplanetary medium. *Journal of Geophysical Research*, *70*(23), 5793–5805. https://doi.org/10.1029/JZ070i023p05793

Winske, D., & Quest, K. B. (1988). Magnetic field and density fluctuations at perpendicular supercritical collisionless shocks. *Journal of Geophysical Research*, *93*(A9), 9681–9693. https://doi.org/10.1029/JA093iA09p09681

Winterhalter, D., Smith, E. J., Burton, M. E., Murphy, N., & McComas, D. J. (1994). The heliospheric plasma sheet. *Journal of Geophysical Research: Space Physics*, *99*(A4), 6667–6680. https://doi.org/10.1029/93JA03481

Wu, C.-C., Liou, K., Lepping, R. P., Vourlidas, A., Plunkett, S., Socker, D., & Wu, S. T. (2017). Observation of an extremely large-density heliospheric plasma sheet compressed by an interplanetary shock at 1 AU. *Solar Physics*, *292*(8), 109. https://doi.org/10.1007/s11207-017-1114-3

Conclusiones

En los últimos años, el creciente interés en el estudio del medio interplanetario ha favorecido el envío de varias sondas a diferentes regiones de éste: La magnetosfera terrestre con las multisondas Cluster (2000), THEMIS (2007) y MMS (2015), el medio interplanetario a 1 AU con las sondas gemelas STEREO (2006) y los recientes lanzamientos de PSP (2018) y Solar Orbiter (2020), cuyo objetivo será acercarse como nunca antes al Sol. Aunado a esto, la mejora en la tecnología de los instrumentos de medición a bordo de estas misiones ha permitido que la resolución de los datos obtenidos sea cada vez mejor; la misión MMS (Burch et al., 2016), por ejemplo, es capaz de proveer datos de plasma con una resolución de hasta 30 ms para electrones y 150 ms para protones en el modo burst.

Al mismo tiempo y debido también al avance tecnológico, la potencia de los equipos de supercómputo y su capacidad de almacenamiento ha aumentado a la vez que los costos de sus componentes se ha reducido facilitando cada vez más el acceso a estos por parte de la comunidad científica. Esto ha propiciado que diferentes códigos híbridos como HYPSI (Burgess and Scholer, 2015; Gingell et al., 2017) y VLASIATOR (Palmroth et al., 2013) que han sido diseñados para correr en este tipo de arquitecturas sean cada vez más usados para simular choques sin colisiones de manera local y global, respectivamente, con características similares a los observados en el medio interplanetario (e.g. choques interplanetarios y choques de proa planetarios).

Por otro lado, aún cuando los datos proporcionados por las sondas poseen una resolución cada vez mejor, lo cual facilita el estudio de la microfísica de los choques sin colisiones, el hecho de que estos datos sean recolectados únicamente a lo largo de una trayectoria 1D, ha sido siempre una limitante a la hora de estudiar los procesos que tienen lugar a través de este tipo de interfaces, incluso en los casos donde un mismo choque es detectado por

varias naves. Y es que, desde el punto de vista de la microfísica, los choques distan mucho de comportarse como una interfaz bien definida y uniforme (Burgess and Scholer, 2015) por lo que el estudio observacional de los procesos que tienen lugar a lo largo de éstos, solo queda descrito de manera parcial con los datos que puede proporcionar una sola nave. Este incoveniente puede ser resuelto de varias maneras dependiendo de las escalas del problema a estudiar: Una posibilidad es buscar una alineación donde las naves se encuentren lo suficientemente cerca como para poder resolver, por ejemplo, la escala del arrugamiento a lo largo del choque cuando éste sea cruzado por una o más naves. También se puede buscar que las órbitas de las naves crucen regiones diferentes del mismo choque (aunque no necesariamente la interfaz de éste) para poder estudiar y relacionar, por ejemplo, como el choque de proa terrestre procesa el viento solar (río arriba de éste) al llegar a la región de la magnetofunda (río abajo de éste).

Sea cual sea la aproximación que se escoja para tratar de mitigar este tipo de problemas inherentes a las observaciones, siempre resultará difícil posicionar una constelación de naves "a modo" para estudiar una característica determinada de los choques espaciales. En cambio, lo que uno hace en la práctica es buscar, en las bases de datos de las diferentes misiones, choques con las características sugeridas por el problema a estudiar. Es aquí donde las simulaciones juegan un papel importante, ya que como se ha demostrado, permiten no solo contrastar los resultados obtenidos observacionalmente, sino que también basados en los resultados de las simulaciones se han propuesto nuevos problemas a investigar o incluso dichos resultados han sido parte de la justificación para el lanzamiento y/o diseño instrumental de nuevas misiones.

Es en este contexto en el que los tres primeros trabajos de esta tesis han sido elaborados. En Kajdič et al. (2019) nuestras simulaciones fueron usadas para validar y hacer más robustos los resultados obtenidos, a saber las primeras observaciones y caracterización de irregularidades a lo largo de varios choques interplanetarios realizadas con varias naves de la misión Cluster. En contraste en Preisser et al. (2020b) las observaciones fueron usadas como input para nuestras simulaciones en el sentido de que los parámetros de entrada de éstas, en particular el número de Mach Alfvénico y el porcentaje máximo de 5 % escogido para el contenido de He^{++}, fueron elegidos con base en trabajos observacionales de

choques y medio interplanetario. Los resultados obtenidos en este estudio (e.g. la correlación entre las fluctuaciones del campo magnético y el comportamiento de $T_\perp/T_\parallel$ y las VDF's para protones y He^{++}) pueden ser tomados como base o bien para validar futuros estudios observacionales. En Preisser et al. (2020a) fue el hallazgo de estructuras con una presión dinámica mayor que la de sus alrededores en la región río abajo de una de nuestras simulaciones lo que nos llevó a consultar algunos trabajos observacionales recientes que nos permitieron asociar dichas estructuras con aquellas previamente identificadas observacionalmente como jets y plasmoides. Más aún, gracias a que en una simulación se puede seguir temporalmente la evolución de dichas estructuras fuimos capaces de reproducir por primera vez, de manera clara, el mecanismo de formación propuesto por Hietala et al. (2009) para un jet, además de proponer también, por primera vez, un mecanismo para la formación de un plasmoide. Con este estudio se demostró que los diferentes mecanismos de formación de estas estructuras dan lugar a firmas diferentes, como ha sido reportado observacionalmente. Estos resultados pueden ser contrastados o servir como motivación para futuros trabajos observacionales relacionados con estas estructuras. Con este trabajo además se enriquece la reciente discusión sobre si ambas estructuras pueden ser consideradas o no como un solo fenómeno (ver Plaschke et al. (2018)).

A diferencia de los tres primeros trabajos antes mencionados, en el cuarto (Blanco-Cano et al., 2020) se realizó un estudio puramente observacional de tres jets observados en la magnetofunda terrestre. El análisis de estos muestra las diferencias internas que puede haber dentro y en los alrededores de dichas estructuras y la posible conexión entre el origen de alguno de éstos y las condiciones presentes en la región río arriba del choque de proa terrestre. Estos resultados plantean nuevas interrogantes que podrían ser resueltas con el estudio de una muestra más numerosa de eventos.

El trabajo a futuro relacionado con los artículos que conforman esta tesis incluye el estudio paramétrico del arrugamiento en choques con diferentes características a partir de las simulaciones y su contraste con observaciones como seguimiento a Kajdič et al. (2019). Para complementar el trabajo realizado en Preisser et al. (2020b) se analizarán las ondas y microinestabilidades río arriba y río abajo de choques con diferente geometría y contenido de He^{++} lo cual añadirá conocimiento a los estudios previos realizados en su

mayoría usando simulaciones 1D. Por último y siendo el tema que puede ser más fructífero debido a su actualidad, se complementarán los resultados obtenidos en Preisser et al. (2020a) sobre jets/plasmoides estudiando las funciones de distribución y el seguimiento de las partículas en y alrededor de estas estructuras así como en las regiones cercanas al choque cuando los jets/plasmoides se forman. Además de esto, un aspecto que ha sido poco estudiado y en el que podría ser interesante ahondar es el de una definición en términos físicos de las fronteras de los jets/plasmoides. Sería interesante investigar si a partir de las simulaciones podemos proponer nuevas formas de identificación más robustas que sin duda mejorarían los estudios observacionales futuros, en particular aquellos donde se hace estadística a partir de las observaciones de estas estructuras. Hay que mencionar que este último posible estudio ha sido motivado por el trabajo observacional de jets en la magnetofunda terrestre (Blanco-Cano et al., 2020) que acaba de ser aceptado para su publicación en la Journal of Geophysical Research: Space Physics.

Apéndice A

Técnicas de simulación numérica

El conocimiento que se tiene actualmente de la física de los choques en plasmas no colisionales ha sido enriquecido, en gran parte, gracias al uso de simulaciones númericas. En este apéndice se describen de manera breve los métodos numéricos usados en las simulaciónes realizadas con un código híbrido como HYPSI (Burgess and Scholer, 2015; Gingell et al., 2017) así como la forma en la que el choque es inicializado en el dominio computacional.

A.1. Ecuaciones básicas

Un plasma no colisional se puede describir usando la ecuación de Vlasov aplicada a la función de distribución $f_j(\mathbf{x}, \mathbf{v}, t)$ de cada una de las especies j

$$\frac{\partial f_j}{\partial t} + \mathbf{v} \cdot \frac{\partial f_j}{\partial \mathbf{x}} + \frac{q_j}{m_j}(\mathbf{E} + \mathbf{v} \times \mathbf{B}) \cdot \frac{\partial f_j}{\partial \mathbf{v}} = 0 \tag{A.1}$$

donde q_j y m_j son la carga y masa, respectivamente, de cada una de las especies j.

Los campos eléctrico $\mathbf{E}$ y magnético $\mathbf{B}$ están dados por las ecuaciones de Maxwell donde los términos fuente i.e. carga ρ y corriente eléctrica J se determinan a partir de los momentos de las funciones distribucion para el total de las especies j =1...M.

$$\frac{1}{c^2}\frac{\partial \mathbf{E}}{\partial t} = \nabla \times \mathbf{B} + \mu_0 J \tag{A.2}$$

$$\frac{\partial \mathbf{B}}{\partial t} = -\nabla \times \mathbf{E} \tag{A.3}$$

$$\nabla \cdot \mathbf{E} = \frac{1}{\epsilon_0}\rho \tag{A.4}$$

$$\nabla \cdot \mathbf{B} = 0 \tag{A.5}$$

con J y ρ dadas entonces por

$$J = \sum_{j=1}^{M} q_j \int d^3v \ \mathbf{v} f_j \tag{A.6}$$

y

$$\rho = \sum_{j=1}^{M} q_j \int d^3v \ f_j \tag{A.7}$$

A.2. Método de simulación numérica híbrida

Cuando en el problema a estudiar no es necesario resolver las escalas espaciales y temporales (e.g. inverso de la girofrecuencia, inverso de la frecuencia del plasma, longitud inercial, radio de giro) de los electrones, éstos no tienen que ser tratados cinéticamente por lo que un tratamiento de éstos, como un fluido, es suficiente. La ecuación de momento para este fluido de electrones puede ser escrita como

$$n_e \, m_e \frac{d\mathbf{V}_e}{dt} = -e \, n_e(\mathbf{E} + \mathbf{V}_e \times \mathbf{B}) - \nabla \cdot \mathbf{P}_e \tag{A.8}$$

donde $\mathbf{V}_e$ y $\mathbf{P}_e$ son la velocidad de fluido y el tensor de presión de los electrones, respectivamente. A fin de eliminar completamente los efectos cinéticos de los electrones, éstos son tratados como un fluido no inercial (m_e =0) por lo que la ecuación A.8 puede ser considerada como una ecuación para el campo eléctrico. Con una presión escalar P_e para los electrones uno obtiene

$$\mathbf{E} = -\mathbf{V}_e \times \mathbf{B} - \frac{\nabla P_e}{e \, n_e} + \eta \, e \, n_e(\mathbf{V}_i - \mathbf{V}_e) \tag{A.9}$$

donde un término resistivo, que describe el acoplamiento macroscópico entre los iones y electrones, ha sido adicionado. La conservación del momento requiere entonces adicionar

también un término de aceleración $-\eta\, J$ en la ecuación de movimiento. La ecuación de fluido para los electrones debe además ser completada por una ecuación de estado para éstos. La condición de cuasi neutralidad puede ser escrita como

$$e\, n_e = q_i\, n_i \tag{A.10}$$

La velocidad de flujo de los electrones puede ser expresada en términos de la velocidad de los iones $\mathbf{V}_i$. Usando la ley de Ampere despreciando la corriente de desplazamiento (aproximación de Darwin), tenemos

$$\nabla \times \mathbf{B} = \mu_0\, \mathbf{J} = \mu_0\, q_i\, n_i (\mathbf{V}_i - \mathbf{V}_e) \tag{A.11}$$

Usando la ecuación A.11 para eliminar $\mathbf{V}_e$ en la ecuación A.9 se obtiene directamente el campo eléctrico, por lo que no es necesario el avance temporal de $\mathbf{E}$. Por otra parte, el campo magnético es avanzado temporalmente usando la ecuación A.3.

Cuando se desean resolver en choques no colisionales a escalas menores de una longitud inercial iónica, los efectos inerciales de los electrones deben ser incluidos, por lo que ya no se puede asumir que m_e =0. El método más común para incluir este efecto es derivar y resolver un conjunto de ecuaciones donde a escalas de electrones, los iones se encuentren inmóviles y la variación en la densidad y velocidad de éstos sea pequeña. Esto se hace tomando el rotacional de la ecuación A.8. El término $\nabla \times \mathbf{E}$ es entonces substituido por $-\partial \mathbf{B}/\partial t$. Como resultado se obtiene una ecuación para la derivada parcial temporal de un campo magnético generalizado $\tilde{\mathbf{B}}$ que tiene la misma forma que la ley de Faraday:

$$\frac{\partial \tilde{\mathbf{B}}}{\partial t} = -\nabla \times \tilde{\mathbf{E}} \tag{A.12}$$

donde el campo magnético generalizado ésta definido por

$$\tilde{\mathbf{B}} = \mathbf{B} - \frac{c}{\omega_{pe}^2} \nabla^2 \mathbf{B} \tag{A.13}$$

y el campo eléctrico generalizado queda determinado por

$$\tilde{\mathbf{E}} = -\mathbf{V}_e \times \mathbf{B} - \frac{\nabla P_e}{e\, n_e} + \frac{m_e}{e}(\mathbf{V}_e \cdot \nabla)\mathbf{V}_e \tag{A.14}$$

Se obtiene, entonces, al igual que para el caso con m_e =0, una ecuación para la evolución temporal de un campo magnético generalizado y otra ecuación para un campo eléctrico generalizado que no tiene que ser avanzado temporalmente.

A.3. Método de inyección

Aunque varios métodos han sido usados para generar choques no colisionales en un sistema numérico (Lembège, 2003), uno de los más usados en simulaciones en una y dos dimensiones es el de inyección. En éste la caja de la simulación se llena con un flujo de plasma super Alfvénico que es continuamente inyectado en dirección de la pared derecha tal como se muestra en la Figura A.1. El flujo es reflejado por la pared derecha interaccionando con el flujo entrante, lo que genera un choque que se desplazará hacia la izquierda conforme el tiempo de la simulación transcurre. La principal ventaja de este método es la facilidad con la que se pueden implementar numéricamente la paredes del dominio computacional (izquierda: inflow, derecha: reflected, superior e inferior: periodic). Uno de los inconvenientes, por otro lado, es que el choque, al moverse hacia la izquierda de la caja de la simulación, acota su tiempo de vida a la vez que la región río arriba se va reduciendo.

Por último, hay que mencionar que parte del trabajo realizado durante el doctorado fue la instalación, puesta en marcha y prueba del código HYPSI en la supercomputadora MIZTLI de la DGTIC-UNAM. Las simulaciones realizadas formaron parte de dos proyectos (LANCAD-UNAM-DGTIC-337) que se sometieron a dicha dependencia y resultaron aprobados.

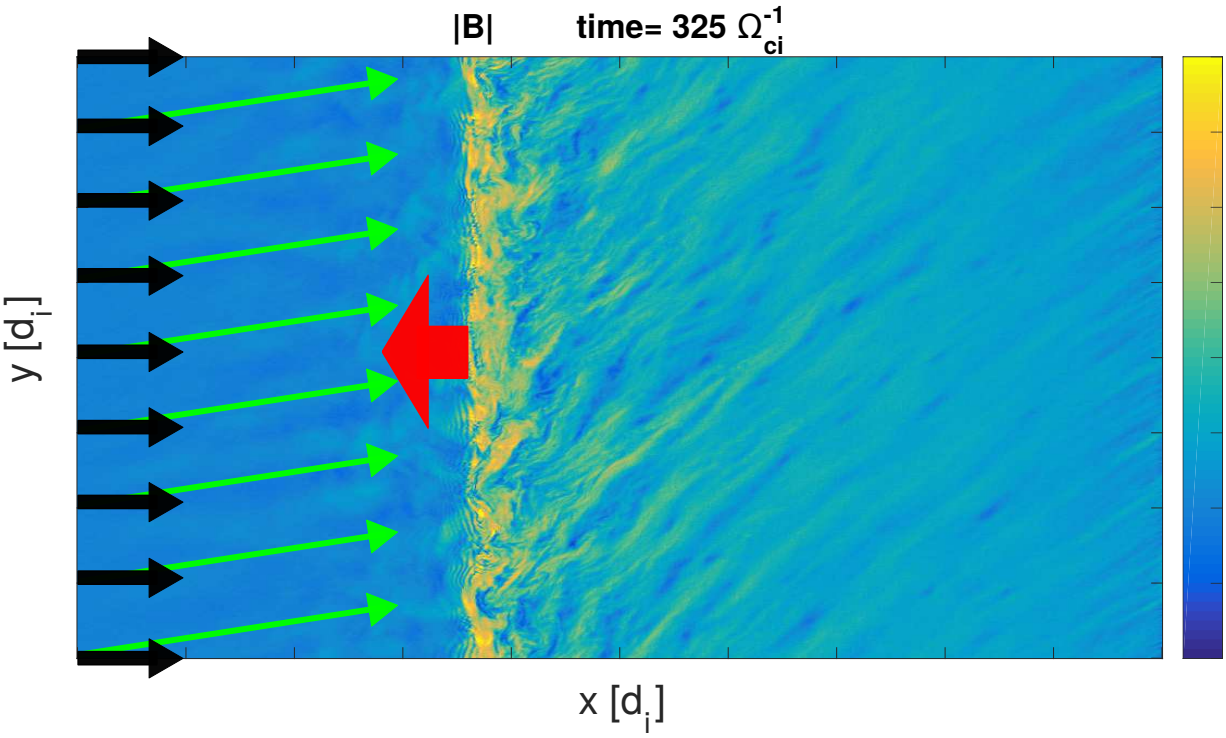

Figura A.1: Esquema del dominio computacional: Las flechas negras representan la dirección del flujo de plasma inyectado continuamente desde la pared izquierda, la flecha roja representa la velocidad del choque, las flechas verdes representan la dirección del campo magnético inicial río arriba.

Bibliografía

B. J. Anderson, R. E. Denton, G. Ho, D. C. Hamilton, S. A. Fuselier, and R. J. Strangeway. Observational test of local proton cyclotron instability in the Earth's magnetosphere. , 101(A10):21527–21544, Oct. 1996. doi: 10.1029/96JA01251.

D. Biskamp and H. Welter. Structure of the earth's bow shock. *Journal of Geophysical Research*, 77(31):6052–6059, 1972. ISSN 2156-2202. doi: 10.1029/JA077i031p06052. URL `http://dx.doi.org/10.1029/JA077i031p06052`.

X. Blanco-Cano, P. Kajdič, E. Aguilar-Rodríguez, C. T. Russell, L. K. Jian, and J. G. Luhmann. Interplanetary shocks and foreshocks observed by stereo during 2007–2010. *Journal of Geophysical Research: Space Physics*, 121(2):992–1008, 2016. ISSN 2169-9402. doi: 10.1002/2015JA021645. URL `http://dx.doi.org/10.1002/2015JA021645`. 2015JA021645.

X. Blanco-Cano, L. Preisser, P. Kajdič, and D. Rojas-Castillo. Magnetosheath microstructure: Mirror mode waves and jets during southward IP magnetic field. *Journal of Geophysical Research (Space Physics)*, 125(9), Sept. 2020. doi: 10.1029/2020JA027940.

J. L. Burch, T. E. Moore, R. B. Torbert, and B. L. Giles. Magnetospheric Multiscale Overview and Science Objectives. , 199(1-4):5–21, Mar. 2016. doi: 10.1007/s11214-015-0164-9.

D. Burgess. Cyclic behavior at quasi-parallel collisionless shocks. , 16(5):345–348, May 1989. doi: 10.1029/GL016i005p00345.

D. Burgess and M. Scholer. *Collisionless Shocks in Space Plasmas: Structure and Accelera-*

ted Particles. Cambridge Atmospheric and Space Science Series. Cambridge University Press, 2015. doi: 10.1017/CBO9781139044097.

C. Escoubet, R. Schmidt, and M. Goldstein. Cluster – science and mission overview. *Space Science Reviews*, 79(1):11–32, Jan 1997. ISSN 1572-9672. doi: 10.1023/A:1004923124586. URL `https://doi.org/10.1023/A:1004923124586`.

S. P. Gary. *Theory of Space Plasma Microinstabilities*. Cambridge Atmospheric and Space Science Series. Cambridge University Press, 1993. doi: 10.1017/CBO9780511551512.

M. Gedalin. Effect of alpha particles on the shock structure. *Journal of Geophysical Research (Space Physics)*, 122(1):71–76, Jan. 2017. doi: 10.1002/2016JA023460.

I. Gingell, S. J. Schwartz, D. Burgess, A. Johlander, C. T. Russell, J. L. Burch, R. E. Ergun, S. Fuselier, D. J. Gershman, B. L. Giles, K. A. Goodrich, Y. V. Khotyaintsev, B. Lavraud, P.-A. Lindqvist, R. J. Strangeway, K. Trattner, R. B. Torbert, H. Wei, and F. Wilder. MMS Observations and Hybrid Simulations of Surface Ripples at a Marginally Quasi-Parallel Shock. *Journal of Geophysical Research (Space Physics)*, 122 (11):11,003–11,017, Nov 2017. doi: 10.1002/2017JA024538.

H. Hietala, T. V. Laitinen, K. Andréeová, R. Vainio, A. Vaivads, M. Palmroth, T. I. Pulkkinen, H. E. J. Koskinen, E. A. Lucek, and H. Rème. Supermagnetosonic Jets behind a Collisionless Quasiparallel Shock. *Phys. Rev. Lett.*, 103(24):245001, Dec. 2009. doi: 10.1103/PhysRevLett.103.245001.

F. M. Ipavich, J. T. Gosling, and M. Scholer. Correlation Between the He/H ratios in upstream particle events and in the solar wind. , 89(A3):1501–1507, Mar. 1984. doi: 10.1029/JA089iA03p01501.

L. Jian, C. T. Russell, J. G. Luhmann, and R. M. Skoug. Properties of Stream Interactions at One AU During 1995 2004. , 2006a.

L. Jian, C. T. Russell, J. G. Luhmann, and R. M. Skoug. Properties of Interplanetary Coronal Mass Ejections at One AU During 1995 2004. , 2006b.

P. Kajdič, L. Preisser, X. Blanco-Cano, D. Burgess, and D. Trotta. First Observations of Irregular Surface of Interplanetary Shocks at Ion Scales by Cluster. *The Astrophysical Journal Letters*, 874(2):L13, Apr 2019. doi: 10.3847/2041-8213/ab0e84.

T. Karlsson, N. Brenning, H. Nilsson, J.-G. Trotignon, X. Vallières, and G. Facsko. Localized density enhancements in the magnetosheath: Three-dimensional morphology and possible importance for impulsive penetration. *J. Geophys. Res.*, 117:A03227, Mar. 2012. doi: 10.1029/2011JA017059.

T. Karlsson, A. Kullen, E. Liljeblad, N. Brenning, H. Nilsson, H. Gunell, and M. Hamrin. On the origin of magnetosheath plasmoids and their relation to magnetosheath jets. *J. Geophys. Res.*, 120:7390–7403, Sept. 2015. doi: 10.1002/2015JA021487.

D. Krauss-Varban and N. Omidi. Structure of medium mach number quasi-parallel shocks: Upstream and downstream waves. *Journal of Geophysical Research: Space Physics*, 96(A10):17715–17731, 1991. ISSN 2156-2202. doi: 10.1029/91JA01545. URL `http://dx.doi.org/10.1029/91JA01545`.

D. Krauss-Varban, Y. Li, and J. G. Luhmann. Ion acceleration at the earth's bow shock and at interplanetary hocks: A comparison. In G. Li, Q. Hu, O. Verkhoglyadova, G. P. Zank, R. P. Lin, and J. G. Luhmann, editors, *Particle Acceleration and Transport in the Heliosphere and Beyond, 7^{th} Annual Astrophysics Conference*, pages 307–313. AIP, 2008. doi: 10.1063/1.2982463. URL `https://doi.org/10.1063/1.2982463`.

Lembège. *Full Particle Electromagnetic Simulation of Collisionless Shocks*, volume 615, pages 54–78. 2003.

M. M. Leroy, D. Winske, C. C. Goodrich, C. S. Wu, and K. Papadopoulos. The structure of perpendicular bow shocks. *Journal of Geophysical Research: Space Physics*, 87(A7):5081–5094, 1982. ISSN 2156-2202. doi: 10.1029/JA087iA07p05081. URL `http://dx.doi.org/10.1029/JA087iA07p05081`.

R. E. Lowe and D. Burgess. The properties and causes of rippling in quasi-perpendicular

collisionless shock fronts. *Annales Geophysicae*, 21(3):671–679, 2003. doi: 10.5194/angeo-21-671-2003. URL `https://www.ann-geophys.net/21/671/2003/`.

Z. Němeček, J. Šafránková, L. Přech, D. G. Sibeck, S. Kokubun, and T. Mukai. Transient flux enhancements in the magnetosheath. *Geophys. Res. Lett.*, 25:1273–1276, 1998. doi: 10.1029/98GL50873.

L. Ofman and M. Gedalin. Rippled quasi-perpendicular collisionless shocks: Local and global normals. *Journal of Geophysical Research: Space Physics*, 118 (10):5999–6006, 2013. ISSN 2169-9402. doi: 10.1002/2013JA018780. URL `http://dx.doi.org/10.1002/2013JA018780`.

M. Palmroth, I. Honkonen, A. Sandroos, Y. Kempf, S. von Alfthan, and D. Pokhotelov. Preliminary testing of global hybrid-Vlasov simulation: Magnetosheath and cusps under northward interplanetary magnetic field. *Journal of Atmospheric and Solar-Terrestrial Physics*, 99:41–46, July 2013. doi: 10.1016/j.jastp.2012.09.013.

F. Plaschke, H. Hietala, and V. Angelopoulos. Anti-sunward high-speed jets in the subsolar magnetosheath. *Ann. Geophys.*, 31:1877–1889, Oct. 2013. doi: 10.5194/angeo-31-1877-2013.

F. Plaschke, H. Hietala, M. Archer, X. Blanco-Cano, P. Kajdič, T. Karlsson, S. H. Lee, N. Omidi, M. Palmroth, V. Roytershteyn, D. Schmid, V. Sergeev, and D. Sibeck. Jets Downstream of Collisionless Shocks. *Space Science Reviews*, 214(5):81, Aug 2018. doi: 10.1007/s11214-018-0516-3.

L. Preisser, X. Blanco-Cano, P. Kajdič, D. Burgess, and D. Trotta. Magnetosheath Jets and Plasmoids: Characteristics and Formation Mechanisms from Hybrid Simulations. , 900(1):L6, Sept. 2020a. doi: 10.3847/2041-8213/abad2b.

L. Preisser, X. Blanco-Cano, D. Trotta, D. Burgess, and P. Kajdič. Influence of He^{++} and Shock Geometry on Interplanetary Shocks in the Solar Wind: 2D Hybrid Simulations. *Journal of Geophysical Research (Space Physics)*, 125(4):e27442, Apr. 2020b. doi: 10.1029/2019JA027442.

M. Scholer and D. Burgess. The role of upstream waves in supercritical quasi-parallel shock re-formation. , 97(A6):8319–8326, June 1992. doi: 10.1029/92JA00312.

S. J. Schwartz and D. Burgess. Quasi-parallel shocks - A patchwork of three-dimensional structures. *Geophys. Res. Lett.*, 18:373–376, Mar. 1991. doi: 10.1029/91GL00138. URL `https://doi.org/10.1029/91GL00138`.

D. J. Southwood and M. G. Kivelson. Mirror instability. I - Physical mechanism of linear instability. , 98(A6):9181–9187, June 1993. doi: 10.1029/92JA02837.

K. J. Trattner, J. L. Burch, S. A. Fuselier, S. M. Petrinec, and S. K. Vines. The 18 november 2015 magnetopause crossing: The gem dayside kinetic challenge event observed by mms/hpca. *Journal of Geophysical Research: Space Physics*, 125(7):e2019JA027617, 2020. doi: 10.1029/2019JA027617. URL `https://agupubs.onlinelibrary.wiley.com/doi/abs/10.1029/2019JA027617`. e2019JA027617 2019JA027617.

D. Winske and K. B. Quest. Magnetic field and density fluctuations at perpendicular supercritical collisionless shocks. *Journal of Geophysical Research: Space Physics*, 93(A9):9681–9693, 1988. ISSN 2156-2202. doi: 10.1029/JA093iA09p09681. URL `http://dx.doi.org/10.1029/JA093iA09p09681`.

T. H. Zurbuchen and I. G. Richardson. In-Situ Solar Wind and Magnetic Field Signatures of Interplanetary Coronal Mass Ejections. , 123(1-3):31–43, Mar. 2006. doi: 10.1007/s11214-006-9010-4.